Thesis for the Degree of Doctor of Philosophy

Disruption mitigation in tokamaks with massive material injection

Oskar Vallhagen

Department of Physics
Chalmers University of Technology
Göteborg, Sweden 2025

Disruption mitigation in tokamaks with massive material injection

OSKAR VALLHAGEN

ISBN 978-91-8103-321-2

Doktorsavhandlingar vid Chalmers tekniska högskola
Ny serie nr 5778
ISSN 0346-718X

Division of Subatomic, High Energy and Plasma Physics
Department of Physics
Chalmers University of Technology
SE-412 96 Göteborg
Sweden
Telephone: +46 (0)31-772 1000

Cover:
Illustration of the deuterium density increase during a shattered pellet injection in a tokamak plasma, using data from figure 2d) in paper **H**. The pellet shards are marked by cyan-filled black circles (enlarged for visibility), and the cyan streaks (vertical width not to scale) and dots illustrate the drift and deposition of the ablated pellet material, with an opacity indicating the ablation rate.

Typeset in LaTeX
Printed in Sweden by
Chalmers digitaltryck
Göteborg, Sweden 2025

Disruption mitigation in tokamaks with massive material injection

OSKAR VALLHAGEN

Department of Physics
Chalmers University of Technology

Abstract

The sudden loss of confinement of the energy content of fusion plasmas in off-normal events, called disruptions, is among the most severe threats to the future of fusion energy based on the tokamak design. An efficient disruption mitigation system will therefore be of utmost importance for future large, high-current devices such as ITER. The potentially greatest threat to be mitigated is posed by currents carried by highly energetic electrons, called runaway electrons, which may cause severe damage upon wall impact. The disruption mitigation system must also ensure a sufficiently homogeneous deposition of the thermal energy on the plasma-facing components, and avoid excessive forces on the machine due to currents flowing in the surrounding structures. The currently envisaged mitigation method is to initiate a massive material injection, primarily in the form of a shattered cryogenic pellet, when an emerging disruption is detected, and so attempt to better control the plasma cooling.

In this thesis, we develop modeling tools for the various physical phenomena present during a tokamak disruption mitigated by a massive material injection. This includes extending existing numerical tools with the capability to handle effects of partial ionization in the cooling plasma on the generation of runaway electrons, and the material assimilation in the plasma following a shattered pellet injection. It also includes the implementation of a method for estimating the losses of runaway electrons due to the vertical motion of the plasma, and the resulting scrape-off against the wall. These tools are then used to simulate a wide range of disruption mitigation scenarios in reactor-scale tokamak devices. Finally, we also develop an analytical model for the radial transport of the relatively cold and dense material recently ablated from a shattered pellet upon exposure to the hot plasma, and the acceleration of the pellet shards due to asymmetries in the ablation.

We find that the severity of a disruption in a reactor-scale device can be significantly reduced by a carefully chosen injection scheme. In particular, a two-stage injection might efficiently reduce the localised heat loads and the runaway generation due to the hot-tail mechanism, by allowing for an intermediate equilibration of the superthermal electron population between the injections. However, the strong runaway avalanche associated with a high plasma current was found to be able to amplify even a very small runaway seed, such as those produced by tritium decay and Compton scattering during nuclear operation, to several mega-amperes. With scrape-off losses included, plausible scenarios with a successful runaway mitigation exist, but the results are sensitive to the details of the evolution of the current density profile. This mitigation scheme might also be further complicated by a relatively large shard deceleration and outward drift of the recently ablated pellet material.

Keywords: fusion plasma, disruption mitigation, shattered pellet injection, runaway electron

List of publications

A Vallhagen, O., Embreus, O., Pusztai, I., Hesslow, L. & Fülöp, T. 2020 "Runaway dynamics in the DT phase of ITER operations in the presence of massive material injection". *Journal of Plasma Physics* **86**, 475860401, doi: 10.1017/S0022377820000859

B Vallhagen, O., Pusztai, I., Hoppe, M., Newton, S. L. & Fülöp, T. 2022 "Effect of two-stage shattered pellet injection on tokamak disruptions". *Nuclear Fusion* **62**, 112004, doi: 10.1088/1741-4326/ac667e

C Vallhagen, O., Pusztai, I., Helander, P., Newton, S. L. & Fülöp, T. 2023 "Drift of ablated material after pellet injection in a tokamak". *Journal of Plasma Physics* **89**, 905890306. doi: 10.1017/S0022377823000466

D Vallhagen, O., Hanebring, L., Artola, F. J., Lehnen, M., Nardon, E., Fülöp, T., Hoppe, M., Newton, S. L. & Pusztai, I. 2024 "Runaway electron dynamics in ITER disruptions with shattered pellet injections". *Nuclear Fusion* **64**, 086003. doi: 10.1088/1741-4326/ad54d7

E Guth, N. J., Vallhagen, O., Helander, P., Pusztai, I., Newton, S. L. & T Fülöp. 2025 "Pellet rocket effect in magnetic confinement fusion plasmas". *Physical Review Letters* **134**, 035101. doi: 10.1103/PhysRevLett.134.035101

F Guth, N. J., Vallhagen, O., Helander, P., Fülöp, T., Tresnjic, A., Newton, S. L. & Pusztai, I. 2025 "The effect of plasmoid drifts on the pellet rocket effect in magnetic confinement fusion plasmas". Accepted: *Journal of Plasma Physics.* doi: 10.48550/arXiv.2412.15824

G Vallhagen, O., Hanebring, L., Fülöp, T., Hoppe, M., & Pusztai, I. 2025 "Reduced modeling of scrape-off losses of runaway electrons during tokamak disruptions". *Journal of Plasma Physics* **91**, E78. doi: 10.1017/S0022377825000327

H Vallhagen, O., Antonsson, L., Halldestam, P., Papp, G., Heinrich, P., Patel, A., Hoppe, M., Votta, L., the ASDEX Upgrade Team & the EUROfusion Tokamak Exploitation Team. 2025 "Simulation of shattered pellet injections with plasmoid drifts in ASDEX Upgrade and ITER". Accepted: *Plasma Physics and Controlled Fusion.* doi: 10.1088/1361-6587/ae140f

Related publications, not included in the thesis

I Hesslow, L., Embreus, O., Vallhagen, O. & Fülöp, T. 2019 "Influence of massive material injection on avalanche runaway generation during tokamak disruptions". *Nuclear Fusion* **59**, 084004,
doi: 10.1088/1741-4326/ab26c2

J Hesslow, L., Unnerfelt, L., Vallhagen, O., Embreus, O., Hoppe, M., Papp, G., & Fülöp, T. 2019 "Evaluation of the Dreicer runaway growth rate in the presence of high-Z impurities using a neural network". *Journal of Plasma Physics* **85**, 475850601,
doi: 10.1017/S0022377819000874

K Fülöp, T., Helander, P., Vallhagen, O., Embreus, O., Hesslow, L., Svensson, P., Creely, A. J., Howard, N. T. & Rodriguez-Fernandez, P. 2020 "Effect of plasma elongation on current dynamics during tokamak disruptions". *Journal of Plasma Physics* **86**, 474860101,
doi: 10.1017/S002237782000001X

L Insulander Björk, K., Papp, G., Embreus, O., Hesslow, L., Fülöp, T., Vallhagen, O., Lier, A., Pautasso, G., Bock, A., the ASDEX Upgrade team & the EUROfusion MST1 team 2020 "Kinetic modelling of runaway electron generation in argon-induced disruptions in ASDEX Upgrade". *Journal of Plasma Physics* **86**, 855860401,
doi: 10.1017/S0022377820000793

M Creely, A. J., Greenwald, M. J., Ballinger, S. B., Brunner, D., Canik, J., Doody, J., Fülöp, T., Garnier, D. T., Granetz, R., Gray, T. K., Holland, C., Howard, N. T., Hughes, J. W., Irby, J. H., Izzo, V. A., Kramer, G. J., Kuang, A. Q., LaBombard, B., Lin, Y., Lipschultz, B., Logan, N. C., Lore, J. D., Marmar, E. S., Montes, K., Mumgaard, R. T., Paz-Soldan, C., Rea, C., Reinke, M. L., Rodriguez-Fernandez, P., Särkimäki, K., Sciortino, F., Scott, S. D., Snicker, A., Snyder, P. B., Sorbom, B. N., Sweeney, R., Tinguely, R. A., Tolman, E. A., Umansky, M., Vallhagen, O., Varje, J., Whyte, D. G., Wright, J. C., Wukitch, S. J., Zhu, J. & the SPARC Team 2020 "Overview of the SPARC tokamak". *Journal of Plasma Physics* **86**, 865860502,
doi: 10.1017/S0022377820001257

N Sweeney, R., Creely, A. J., Doody, J., Fülöp, T., Garnier, D. T., Granetz, R., Greenwald, M., Hesslow, L., Irby, J., Izzo, V. A., La Haye, R. J., Logan, N. C., Montes, K., Paz-Soldan, C., Rea, C., Tinguely, R. A., Vallhagen, O. & Zhu, J. 2020 "MHD stability and disruptions in the SPARC tokamak". *Journal of Plasma Physics* **86**, 865860507,
doi: 10.1017/S0022377820001129

O Svensson, P., Embreus, O., Newton, S. L., Särkimäki, K., Vallhagen, O. & Fülöp, T. 2021 "Effects of magnetic perturbations and radiation on the runaway avalanche". *Journal of Plasma Physics* **87**, 905870207, doi: 10.1017/S0022377820001592

P Insulander Björk, K., Vallhagen, O., Papp, G., Reux, C., Embreus, O., Rachlew, E., Fülöp, T., the ASDEX Upgrade team, JET contributors & the EUROfusion MST1 team 2021 "Modelling of runaway electron dynamics during argon-induced disruptions in ASDEX Upgrade and JET". *Plasma Physics and Controlled Fusion* **63**, 085021, doi: 10.1088/1361-6587/ac07b5

Q Pusztai, I., Hoppe, M. & Vallhagen, O. 2022 "Runaway dynamics in tokamak disruptions with current relaxation". *Journal of Plasma Physics* **88**, 905880409, doi: 10.1017/S0022377822000733

R Berger, E., Pusztai, I., Newton, S. L., Hoppe, M., Vallhagen, O., Fil, A. & Fülöp, T. 2022 "Runaway dynamics in reactor-scale spherical tokamak disruptions". *Journal of Plasma Physics* **88**, 905880611, doi: 10.1017/S0022377822001209

S Pusztai, I., Ekmark, I., Bergström, H., Halldestam, P., Jansson, P., Hoppe, M., Vallhagen, O. & Fülöp, T. 2023 "Bayesian optimization of massive material injection for disruption mitigation in tokamaks". *Journal of Plasma Physics* **89**, 905890204, doi: 10.1017/S0022377823000193

T Ekmark, I., Hoppe, M., Fülöp, T., Jansson, P., Antonsson, L., Vallhagen, O. & Pusztai, I. 2024 "Fluid and kinetic studies of tokamak disruptions using Bayesian optimization". *Journal of Plasma Physics* **90**, 905900306, doi: 10.1017/S0022377824000606

U Bandaru, V., Hoelzl, M., Artola, F. J., Vallhagen, O., Lehnen, M. & the JOREK Team 2024 "Runaway electron fluid model extension in JOREK and ITER relevant benchmarks". *Physics of Plasmas* **31**, 082503, doi: 10.1063/5.0213962

V Fil, A., Henden, L., Newton, S., Hoppe, M. & Vallhagen, O. 2024 "Disruption runaway electron generation and mitigation in the Spherical Tokamak for Energy Production (STEP)". *Nuclear Fusion* **64**, 106049, doi: 10.1088/1741-4326/ad73e9

W Halldestam, P., Heinrich, P., Papp, G., Hoppe, M., Hoelzl, M., Pusztai, I., Vallhagen, O., Fischer, R., Jenko, F., the ASDEX Upgrade Team, the EUROfusion Tokamak Exploitation Team 2025 "Reduced kinetic modelling of shattered pellet injection in ASDEX Upgrade". *Journal of Plasma Physics* **91**, E104,
doi: 10.1017/S0022377825100470

Conference contributions

X Pusztai, I., Hoppe, M., Vallhagen, O. & Fülöp, T. 2023 "Runaway dynamics in disruptions with current relaxation events". *Proceedings of the 48th EPS Conference on Plasma Physics, Online, 27th June - 1st July 2022* IAEA-CN-316-1770.
https://conferences.iaea.org/event/316/papers/28547/files/10745-AFIL%20-%20IAEA%20FEC%202023%20Paper%20-%20Final.pdf

Y Fil, A., Henden, L., Newton, S., Hoppe, M. & Vallhagen, O. 2023 "Disruption runaway electron generation and mitigation in the spherical tokamak for energy production". *Proceedings of the 29th IAEA Fusion Energy Conference, London, 16th - 21th October 2023* IAEA-CN-316-1770.
https://conferences.iaea.org/event/316/papers/28547/files/10745-AFIL%20-%20IAEA%20FEC%202023%20Paper%20-%20Final.pdf

Z Nardon, E., Peysson, Y., Reux, C., Saura, R., Wang, C., Artola, F. J., Lehnen, M., Bandaru, V., Bergström, H., Halldestam, P., Hoelzl, M., Papp, G., Särkimäki, K., Decker, J., Sommariva, C., Ekmark, I., Fülöp, T., Pusztai, I., Vallhagen, O., Hoppe, M., Järvinen, A., Olasz, S., Poko, G., JET Contributors & the JOREK team 2023 "Modelling of runaway electron dynamics in tokamak disruptions". *Proceedings of the 29th IAEA Fusion Energy Conference, London, 16th - 21th October 2023* IAEA-CN-316-2174.
https://conferences.iaea.org/event/316/papers/27851/files/10722-Nardon_IAEA_FEC_2023_Paper.pdf

a Vallhagen, O., Hanebring, L., Artola, F. J., Lehnen, M., Nardon, E., Fülöp, T. & Pusztai, I. 2023 "Runaway electron dynamics in ITER disruptions with shattered pellet injection". *Proceedings of the 29th IAEA Fusion Energy Conference, London, 16th - 21th October 2023* IAEA-CN-316-2158.
https://conferences.iaea.org/event/316/papers/28126/files/10770-IAEA_FEC2023_Vallhagen_TH.pdf

b Ekmark, I., Hoppe, M., Fülöp, T., Tinguely, R. A., Sweeney, R., Jansson, P., Antonsson, L., Vallhagen, O. & Pusztai, I. 2024 "Fluid and kinetic modeling of runaway electron generation from tritium beta decay and Compton scattering". *Proceedings of the 50th EPS Conference on Plasma Physics, Salamanca, 8th - 12th July 2024* P4.109.
https://lac913.epfl.ch/epsppd3/2024/html/PDF/P4-109.pdf

c Halldestam, P., Heinrich, P., Papp, G., Hoppe, M., Hölzl, M., Pusztai, I., Vallhagen, O., Fischer, R., Jenko, F., the ASDEX Upgrade Teama & the EUROfusion Tokamak Exploitation Team 2024 "Reduced fluid modelling of shattered pellet injection in ASDEX Upgrade". *Proceedings of the 50th EPS Conference on Plasma Physics, Salamanca, 8th - 12th July 2024* P5.085.
https://lac913.epfl.ch/epsppd3/2024/html/PDF/P5-085.pdf

d Vallhagen, O., Antonsson, L., Halldestam, P., Pusztai, I., Helander, P., Newton, S., Papp, G., Heinrich, P., Patel, A., Hoppe, M., Fülöp, T., the ASDEX Upgrade Teama & the EUROfusion Tokamak Exploitation Team 2024 "From injection to deposition - capturing the drift of ablated pellet material in a tokamak". *Proceedings of the 50th EPS Conference on Plasma Physics, Salamanca, 8th - 12th July 2024* O2.305.
https://lac913.epfl.ch/epsppd3/2024/html/PDF/O2-305.pdf

Statement of contribution

A I established the scenarios to be studied in collaboration with the co-authors, ran all simulations and extracted the presented data. The figures and manuscript were produced jointly by me and the co-authors.

B I implemented the shattered pellet injection model in the DREAM code, ran all of the simulations and created all figures. I also performed the derivations and calculations in appendix B. The manuscript was written jointly by me and the co-authors.

C I was the main person responsible for conceptualising the idea and deriving the plasmoid drift model, and I created all figures. The manuscript was written jointly by me and the co-authors.

D I implemented the required new functionality in the DREAM code, including the ion advection and diffusion terms and support for the shattered pellet injection model in an arbitrary flux surface geometry. I established the scenarios to be studied in collaboration with the co-authors, and ran the simulations and created all the figures in close collaboration with L. Hanebring and I. Pusztai. The manuscript was written jointly by me and the co-authors.

E I conceptualised the idea behind the rocket effect model, and derived the equation system to be solved (equation (3)-(7)) in close collaboration with P. Helander and N. Guth. I outlined the semi-analytical solution, and supervised N. Guth who implemented the numerical part of the solution. I contributed to the editing during the writing of the manusscript.

F I conceptualised the idea behind the rocket effect model first presented in paper **E**, which is elaborated on in this paper. I derived the model for the plasmoid shielding asymmetry and its contribution to the rocket force in close collaboration with N. Guth. I supervised N. Guth and A. Tresnjic who performed the numerical calculations and simulations, and contributed to the writing of the manuscript.

G I conceptualised the idea behind the scrape-off runaway electron loss term in collaboration with the co-authors and acknowledged external colleagues. I supervised L. Hanebring who implemented the loss term in the DREAM code, and ran all simulations except those in appendix A in close collaboration with her. I created all figures except figure 4 and wrote the manuscript.

H I supervised L. Antonsson who implemented the plasmoid drift model in the DREAM code, and ran the ITER simulations in close collaboration with him. I ran all of the ASDEX Upgrade simulations, created all figures and wrote the manuscript.

Acknowledgments

I would like to express my sincerest gratitude towards the people who have supported me in all aspects of my life during my work leading up to the finishing of this thesis. First of all, I want to thank my main supervisor and mentor Tünde Fülöp, who has believed in me ever since I was a second-year Bachelor student. Her tremendous effort to support her students, and her mantra that poor confidence is forbidden, has enabled me to repeatedly step out of my comfort zone and manage things I didn't think I ever could. I have also received invaluable support from my co-supervisors István Pusztai and Sarah Newton, who always take their time to provide their great experience and expertise in all parts of academic life. This includes the huge effort of following the details of my work even when I ended up working with pellet theory outside the group's main area of expertise. I also want to thank Christian Forssén for taking the role as my examiner although my research is not related to his field.

This thesis would not have been possible without the collaboration with several other colleagues. I especially want to thank Mathias Hoppe for sharing his baffling computational science expertise, Gergely Papp for his lightning-quick extensive email replies and for taking so good care of me during my visits to Garching, and Per Helander for spending his valuable time sharing his wide theoretical expertise, giving me appreciated breaks from the computer and boosting my faith in pure human abilities. I also want to thank all the undergraduate students I have had the privilege to supervise, with special thanks to Lise Hanebring, Liam Antonsson and Nico Guth who have all greatly contributed to the research in this thesis. Conversely, I want to thank Ola Embreus and Linnea Hesslow for their valuable supervision when I was an undergraduate student myself. The list could be extended to all past and present members of the group, nobody named, nobody forgotten.

Besides the academic community, I could not have finished this thesis without the support and presence from my great family and friends. A special thanks goes to Julia Järlebark and Erik Svensson, for a decade ranging between silly laughs, unforgettable trips and support in figuring out the course of our lives, and to Carin Lundqvist and Ebba Grönfors, for simply being incredibly kind, regardless of my ability to be an enjoyable company. I also want to thank all past and present members of F-spexet, for the companionship and warm environment that really makes you feel like a weird second family. Finally, I want to thank my real family, for always offering their help with whatever they can, for always being caring and supportive and for keeping up the good puns and teasing in a true Göteborg spirit.

Oskar Vallhagen, Göteborg, 2025-10-23

Contents

Chapter 1

Introduction

The steadily increasing energy consumption around the world will make future generations' demand for reliable and clean energy sources larger than ever before. If successful, fusion energy has the potential to play a key role in a future carbon-free energy system. Even if commercial fusion does not become available soon enough to tackle the most urgent climate changes, it may still be of importance to meet the increasing energy demand during the later half of this century (Cabal *et al.*, 2017).

In many ways, fusion can be regarded as an ideal energy source (Chen, 2011): The fusion reactions do not produce any other waste products than helium, making fusion sustainable from a climate perspective. The hydrogen isotopes used as fuel can be extracted from ordinary sea water or can be produced at the power plant through lithium breeding by neutron irradiation, making the fuel reserves practically unlimited. The energy production is not weather-dependent, and the fusion energy output can therefore be adapted to a varying demand to a greater extent than intermittent renewable energy sources. The half-life of the radioactive materials produced by neutron bombardment of the reactor wall is of the order of hundreds of years. This is about a thousand times shorter than the hundreds of thousands of years for some of the high level radioactive waste produced by a fission reactor. Finally, fusion produces no by-products that may be used for nuclear weapons.

There are, however, many difficulties involved in realizing a fusion power plant (Chen, 1974). In order to fuse two nuclei, the distance between them must be similar to their de Broglie wavelength. At this point, the probability to overcome the remaining Coulomb potential barrier by tunneling becomes significant. For this to happen, the nuclei have to overcome the Coulomb repulsion at larger distances, and therefore they have to collide at a very high energy. In order to achieve such energetic collisions, the fuel must be heated to a temperature of the order of 10^8 K. Confining such a hot fuel and maintaining the conditions necessary for a substantial fusion reaction rate is a challenging task. The most developed method to overcome these challenges, aiming to use fusion as an energy source, is so-called magnetically confined fusion, which is introduced in section 1.1.

Although magnetically confined fusion devices allow for a stable confinement of the fusion fuel during normal operation, they must also be able to handle off-normal events, where the confinement is suddenly lost, called disruptions (Hollmann *et al.*, 2015). These events result in a rapid release of the stored thermal and magnetic

energy, which can be very dangerous for the machine integrity. The basic features of disruptions, their consequences, and suggested methods to mitigate their impact on the machine are introduced in section 1.2. However, disruption mitigation in future large reactor-scale fusion devices is still an unresolved issue. This is the topic to which this thesis aims to contribute, by providing specific guidelines to mitigate the effects of such events.

1.1 Magnetic plasma confinement and the tokamak design

At the high temperatures necessary for fusion energy generation, the electrons in the fuel are separated from the atomic nuclei. When this happens, the fuel becomes a plasma, which may be regarded as a gas consisting of unbound charged particles. Since the particles are charged, they may be controlled by a magnetic field, which is the fundamental physical basis of magnetic confinement fusion.

When a charged particle is subject to a magnetic field, it undergoes a gyro-motion around the magnetic field lines, while traveling along the field lines (Freidberg, 2008). Naively, one could therefore confine the plasma by bending the magnetic field into a torus. This is indeed the basic principle behind magnetically confined fusion. However, the construction of such a magnetic field inevitably introduces a gradient of the field strength along the major radius of the torus. This magnetic field gradient makes a plasma in a purely toroidal magnetic field intrinsically unstable, as explained below.

A gradient in the magnetic field makes the radius of the gyro-motion longer in the part of the gyration where the magnetic field is weaker, compared to the part where it is stronger. This results in a drift of the center of gyration, called the *guiding center*, perpendicular to both the magnetic field and its gradient, as illustrated in figure 1.1a). This drift is referred to as the ∇B*-drift*. As the ∇B-drift is oppositely directed for electrons and ions, it will induce a charge separation in the plasma, generating a vertical electric field.

This electric field also affects the gyroradius during the particle motion. For a positively (negatively) charged particle, when the particle moves parallel (antiparallel) to the electric field, its speed, and therefore its gyroradius, increases, and when it moves antiparallel (parallel) to the electric field it decreases. This causes the gyroradius to vary along the direction of the electric field, in opposing ways for electrons and ions, leading to a guiding center drift perpendicular to both the magnetic and electric field, as illustrated in figure 1.1b). This drift is referred to as the $E \times B$ *drift*. As evident from figure 1.1b), this drift has the same direction for both electrons and ions, leading to the whole plasma drifting out of confinement.

This issue can be resolved by introducing a poloidal twist to the magnetic field, i.e. a magnetic field component circulating the short way around the torus, as illustrated in figure 1.2a) (Freidberg, 2008). This twist is quantified by the *safety factor*, denoted q, defined as the ratio of the number of times a field line revolves in the toroidal direction for every revolution in the poloidal direction. It typically lies in the range of $1 - 2$ in most of the plasma, but may increase rapidly at the plasma

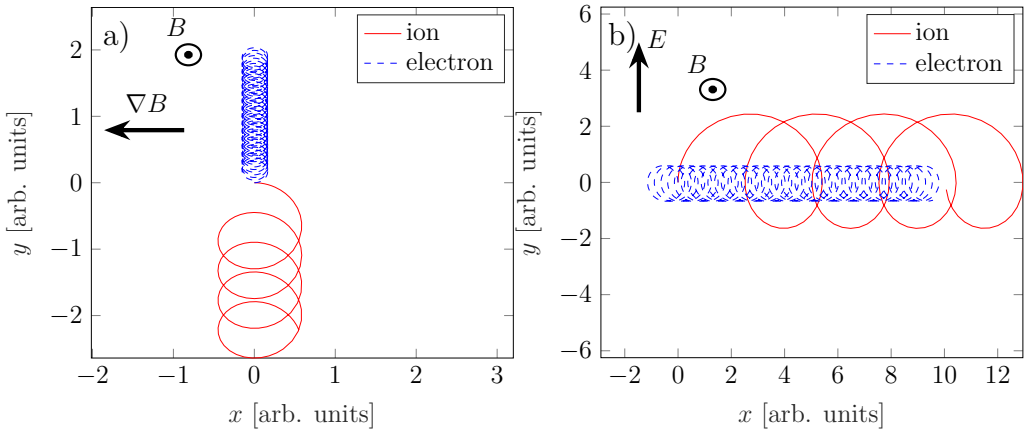

Figure 1.1: Particle trajectories for an ion and electron, starting from the origin, with different prescribed electric and magnetic field settings. a) A magnetic field pointing in the positive z-direction (out from the paper) with a uniform gradient in the negative x-direction, giving rise to a ∇B-drift. The resulting charge separation gives rise to an electric field in the positive y-direction. b) A constant uniform magnetic field pointing in the positive z-direction and a constant uniform electric field pointing in the positive y-direction, giving rise to an $E \times B$-drift. The ratio of the gyroradii of the electron and the ion is enlarged for visibility.

edge. Such a twist makes the particles circulate around the plasma in the poloidal direction in a way that averages out the effect of the vertical ∇B-drift; in the upper part of the poloidal motion, the ∇B-drift drives the particles away from the plasma center, while in the lower part the ∇B-drift drives the particles back towards the center. In that way, the charge separation, and hence the $E \times B$-drift that would break the confinement, is avoided, as illustrated in figure 1.2.

In the most studied design for such a configuration, the so-called *tokamak*, this twist of the field lines is achieved by driving a large toroidal current through the plasma, of the order of mega-amperes (MAs). In such a configuration, the magnetic field lines can be shown to circulate in the plasma following nested toroidal surfaces called *flux surfaces* (surfaces of constant poloidal magnetic flux), sketched in figure 1.2a) (Freidberg, 2008). The particles in the plasma then stay essentially confined to one of those flux surfaces*.

There are two types of confined trajectories which the particles may follow, depending on the ratio $v_\perp/v_{||}$ of the speed perpendicular and parallel to the field lines. The separation is related to the fact that the magnetic moment $\mu = \gamma m v_\perp^2/(2B)$ associated with the gyro-motion can be shown to be an adiabatic invariant (Chen, 1974), where γ is the Lorentz factor and m is the particle mass. Thus, as the particle approaches the inner part of the torus, where B increases, $v_\perp$ must also increase, forcing $v_{||}$ to decrease due to energy conservation. For sufficiently large minimum values of $v_\perp$ along the trajectory, there will be a point where $v_{||}$ vanishes completely, forcing the particle to turn around. These particles follow *trapped orbits*, as illustrated in figure 1.2c). If the minimum value of $v_\perp$ is sufficiently small, the particle is however able to complete a full poloidal transit, following a *passing orbit*,

*In the absence of fluctuations and collisions, which are important on a longer time scale.

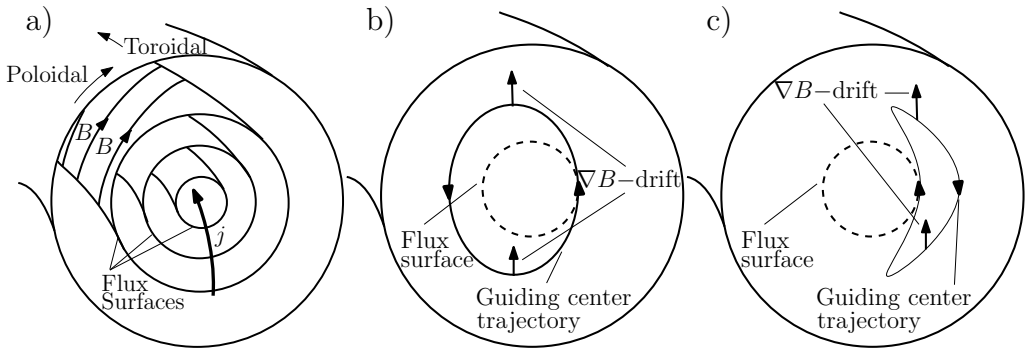

Figure 1.2: a) Illustration of the magnetic field configuration in a tokamak; the magnetic field is the sum of a toroidal component generated by external coils (not shown in the figure) and a poloidal component generated by the plasma current. The resulting magnetic field lines follow helical paths around the plasma, ordered in a set of nested flux surfaces. b) Projection of the guiding center trajectory of an ion in a tokamak on the poloidal plane, illustrating how the ∇B-drift is averaged out by the motion along the poloidal component of the magnetic field for a passing orbit. A flux surface with circular cross section, tangential to the ion guiding center trajectory, is included as reference. c) The same as b) but for a trapped orbit. The drift away from the flux surfaces is exaggerated for visibility.

as illustrated in figure 1.2b).

The tokamak design is utilised by the JET (Joint European Torus) device, currently holding the record for the ratio of the generated fusion power to the supplied heating power - the so-called Q-factor - at 0.67. It is also used for future devices aiming at producing a net gain of fusion energy. These devices include SPARC, under development by Commonwealth Fusion Systems (Paper **M**), STEP (Spherical Tokamak for Energy Production) under development by the UK Atomic Energy Authority, and ITER, which is currently under construction in France by the ITER organization. ITER will be the largest among the next generation of fusion devices, and is the main concern of this thesis. The ITER project is an international collaboration between the European Union, United States, China, Russia, South Korea, India and Japan, aiming for a Q-factor of 10. In order to increase the Q-factor, next-generation devices will store significantly larger thermal and magnetic energies than current experiments. This increases the severity of the threat posed by disruptions, to which we now turn our attention.

1.2 Tokamak disruptions

Disruptions are a form of operational failure, where the plasma confinement is suddenly lost, and the energy contained in the plasma is dissipated to the surrounding structures (Hender *et al.*, 2007). A disruption typically includes four phases, as introduced below and described in more detail in sections 3.1-3.2.

During the first phase of a disruption, called the thermal quench, the vast majority of the thermal energy may be released over a time scale as short as 0.1–1 ms, and the temperature typically drops by several orders of magnitude. This phase

is usually triggered by a perturbation to the magnetic field that becomes unstable, leading to the development of a so-called magnetohydrodynamic (MHD) instability. Such an instability introduces a stochastic component to the magnetic field which, to some extent, temporarily breaks the flux surface geometry and therefore strongly enhances the radial transport of particles and heat.

The drop in temperature also comes with a drop in conductivity, leading to dissipation of the magnetic energy associated with the plasma current. This drop in conductivity is related to the fact that, in a plasma, the collisional interaction between the particles is dominated by their Coulomb interaction (Chen, 1974). This leads to the somewhat counter-intuitive phenomenon that the drag force felt by a particle moving through the plasma decreases with its momentum, as particles with a higher relative momentum spend less time in the vicinity of one another, giving the Coulomb force less time to cause a momentum change. The phase of the disruption thus initiated is called the current quench.

However, the decay of the plasma current leads to the induction of a high electric field. As the drag force decreases at high momenta, the force exerted by the electric field will overcome the drag force for all particles with a momentum higher than a critical value. This enables these particles, called runaway electrons, to be accelerated to extremely high energies. As long as there is any mechanism present which can feed the region of momentum space above the critical momentum, as described in section 2.2.2, a part of the plasma current will be replaced by a runaway current which, due to the low collisionality at high momenta, can remain in the plasma much longer than the resistive time scale. This phase of the disruption is called the runaway plateau phase. It typically lasts until the vertical control of the plasma is lost, initiating the scrape-off phase, where the runaway current is terminated by being scraped off against the wall.

The rapid release of the thermal and magnetic energy might cause severe damage to the device (Hollmann *et al.* (2015), Paper **N**). The rapid release of the thermal energy can cause a substantial sputtering, or even melting, of the wall material. A rapid current drop can induce large eddy currents in the structures surrounding the plasma, which in the presence of the strong magnetic fields used to control the plasma may result in large forces being exerted on the machine. Conversely, if the current decay is slow, the plasma control might be lost while there is a substantial current remaining in the plasma. The currents in the outer layers of the plasma may then begin to flow through the surrounding structures, forming a so-called halo-current. Such a current may also lead to large forces being exerted on the machine. Finally, the potentially most severe threat to a reactor-scale tokamak is the generation of runaway electrons, which may cause a significant melting of plasma-facing components upon impact.

The potential damage resulting from a disruption as described above poses strict requirements for disruption mitigation (Hollmann *et al.*, 2015). Three main tasks must be accomplished by a tokamak disruption mitigation system. The first is to minimize the localized heat loads on the plasma facing components, by spreading the heat loads over as large an area as possible. Secondly, the disruption mitigation system must control the time scale for the current decay so that it is long enough to avoid excessive eddy currents, but short enough to avoid excessive halo currents.

Finally, the current carried by runaway electrons impacting the wall should be minimized.

The currently envisaged disruption mitigation method is to inject a comparatively massive amount of material into the plasma as soon as the emerging disruption is detected. The injection primarily consists of hydrogen isotopes and/or noble gases, such as neon or argon. As this material enters the plasma in the form of neutral atoms, and typically is not fully ionized throughout a substantial part of the disruption, it may emit line radiation when excited by exposure to the plasma. This radiation can release the thermal energy isotropically, reducing the maximum localised heat loads. The amount and composition of the injected material can also be tuned to gain some control over the temperature after the initial drop, which in turn determines the current decay rate. Moreover, as the injected material ionizes, the electron density increases. This leads to an increase in the drag force felt by the electrons in the plasma, which to some extent can be used to reduce the runaway generation.

Conventionally, the injected material is delivered as a gas puff from a pressurized vault (Hollmann *et al.*, 2015). While this technique is comparatively simple, it comes with a number of disadvantages. The injected gas ionizes rapidly when exposed to the still hot plasma. When ionized, the injected material becomes tied to the magnetic field, which substantially slows down the transport towards the plasma core. Moreover, the gas injection introduces a perturbation to the magnetic field, which accelerates the growth of the plasma instabilities. As a result, the disruption might fully begin before the injected material has reached the plasma center.

Another approach, that can provide better core penetration, is to inject material in the form of a solid, cryogenic pellet. The exposure to the plasma causes the pellet to ablate and deposit its content along its trajectory. The ablation can be made more efficient by shattering the pellet into smaller shards before it enters the plasma, forming a so-called Shattered Pellet Injection (SPI). This technique has been chosen as the baseline for the disruption mitigation system at ITER (Lehnen *et al.*, 2020).

There are however potential drawbacks of this technique as well. One important example stems from the fact that in the very dense plasma cloud surrounding the ablating pellet, the poloidal component of the magnetic field cannot average out the local ∇B-drift, so that a local charge separation occurs. The corresponding $E \times B$-drift will transport the ablated material along the major radius direction until it has homogenized with the rest of the plasma, as detailed in section 4.3.1. In addition, uneven ablation may give rise to a rocket-like propulsion of the pellet shards, as described in section 4.4, which may significantly limit their penetration depth. Both these mechanisms lower the core penetration and might even expel the ablated material from the plasma.

In conclusion, the design of a disruption mitigation system for a reactor-scale tokamak remains an open question, to which the work in this thesis aims to contribute. The pellet injection theory developed in this thesis may also be relevant for other types of material injection.

1.3 Thesis outline

The rest of this thesis is structured as follows. In chapter 2 the theory governing the momentum space dynamics in a plasma is introduced, with a focus on the formation of runaway electrons. Chapter 3 gives an overview of tokamak disruptions, mitigation requirements and mitigation strategies. A detailed background of the physics of pellet injection in a tokamak, which is the injection technique most thoroughly studied in this work, is given in chapter 4. The components necessary for a full disruption mitigation model are then summarized in chapter 5, and the numerical tools GO and DREAM, which are used extensively in this work, are introduced. Finally, the appended papers are summarized in chapter 6, where we also discuss the implications of this work and suggestions for future studies.

Chapter 2

Momentum space dynamics of plasmas

Many of the phenomena at play during a tokamak disruption, as introduced in the previous chapter, are related to the way the electron phase space distribution function evolves in a plasma and how it couples to the electromagnetic fields present. More precisely, the collisional properties of a plasma play a particularly important role. In this chapter we start by giving a qualitative illustration of the collisional dynamics of a plasma in section 2.1, where we also derive scaling laws providing an intuitive understanding of the electrical conductivity and the runaway phenomenon in a plasma. We then give an overview of the so-called kinetic equation, which governs the electron phase space distribution function in a plasma, in section 2.2, before taking a more detailed look at the runaway phenomenon and how runaway electrons are generated in a tokamak disruption in section 2.2.2.

2.1 Coulomb collisions

Collisions in a plasma differ quite significantly from collisions in a gas. Instead of the binary close collisions which dominate in a gas, the collisional dynamics in a plasma is dominated by long-range interactions through the Coulomb force. An important consequence of this is that, as we will see shortly, fast particles are *less* collisional than slow particles, as opposed to the case in a gas.

A qualitative comparison of the difference between Coulomb collisions and close collisions prevailing in a gas is illustrated in figure 2.1a). This illustration is made using a simple simulation of a particle traveling through a fixed ion background (corresponding to background particles with a much larger mass than the test particle, which would be the case if the moving particle was an electron). If the particle is neutral, so that the interaction with the background takes place through close collisions, the resulting trajectory will be made up of straight line segments with sharp deflections where a collision takes place. If the particle is an electron, on the other hand, the long-range Coulomb interaction with the background ions causes the electron to follow a smoothly curved path. Notably, while the path of the neutral particle is determined by a set of consecutive large angle collisions, the path of the electron is determined by the contribution from many small angle collisions with

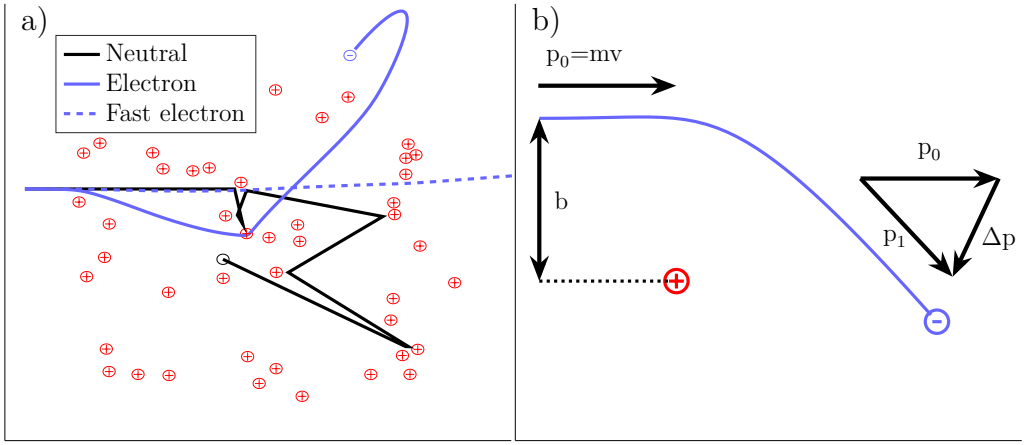

Figure 2.1: a) Illustration of a neutral atom (black), and two electrons (blue) with different speeds moving through a background of fixed ions, comparing electron-ion Coulomb collisions with close collisions with neutrals, and illustrating the velocity dependence of Coulomb collisions. b) Illustration of a single Coulomb collision between an incident electron and a fixed ion. Note that for the vast majority of collisions $\Delta p \ll p_0$, although Δp is exaggerated here for visibility.

many ions at the same time (Helander & Sigmar, 2005). Moreover, for the neutral particle, the deflection angle is independent of the particle speed, but for the electron interacting through the Coulomb force, we see that a fast electron is significantly less affected by the background ions than a slower one. This happens because the time spent in the vicinity of the ions decreases with an increasing electron speed, without affecting the interaction force.

The setup for a single Coulomb collision of an electron with mass m, traveling with a velocity v and colliding with a fixed ion, is shown in figure 2.1b). The ion is assumed here to have an equal but opposite charge compared to the electron. In the absence of the Coulomb force, the electron would have a distance of closest approach equal to b as defined in the figure, which is referred to as the *impact parameter*. After the collision, the electron has acquired a change in momentum of magnitude Δp.

Before turning to a rigorous kinetic description of Coulomb collisions, one may gain an increased intuitive understanding based on scaling laws derived from the simple case depicted above. The velocity scaling of the cross section and collision frequency of electron-ion Coulomb collisions, defined as the rate at which the electron momentum undergoes an order unity relative change, can be determined as follows. As mentioned above, for Coulomb collisions, the momentum change is dominated by the accumulated effect of many small-angle interactions, but as we are primarily interested in the speed scaling here, we may simplify the picture by considering events where the order unity momentum change occurs due to a single Coulomb interaction. During the main part of this interaction, the Coulomb force is roughly given by

$$F_\mathrm{c} \sim \frac{e^2}{4\pi\epsilon_0 b^2}, \tag{2.1}$$

where e is the elementary charge and ϵ_0 is the vacuum permittivity, and is felt during a collision duration time roughly given by $t_\mathrm{c} \sim b/v$. From these considerations, we

may relate the impact parameter necessary for a significant deflection of the electron to the electron velocity according to

$$\Delta p \sim mv \sim F_{\mathrm{c}} t_{\mathrm{c}} \sim \frac{e^2}{4\pi\epsilon_0 b v} \Rightarrow b \sim \frac{e^2}{4\pi\epsilon_0 m v^2}. \tag{2.2}$$

The cross section can then be estimated according to

$$\sigma_{\mathrm{c}} \sim \pi b^2 \sim \frac{e^4}{16\pi\epsilon_0^2 m^2 v^4}. \tag{2.3}$$

The collision frequency can now be estimated by the number of electrons passing through a cross section of area σ_{c} per unit time, according to

$$\nu \sim nv\sigma_{\mathrm{c}} \sim \frac{ne^4}{16\pi\epsilon_0^2 m^2 v^3}. \tag{2.4}$$

Here, n is the density of electrons or ions, assumed to be equal here for simplicity. The important take-away here is the $1/v^3$-scaling, which quantifies the previous observation that fast particles are less collisional in a plasma. In practice, however, the particles in a plasma do not all have the same velocity, but usually a thermal, Maxwellian, distribution of velocities. To estimate the collision frequency for a thermal plasma, we may therefore replace the velocity v by the thermal speed $v_{\mathrm{th}} = \sqrt{k_{\mathrm{B}} T/m}$ and obtain the thermal collision frequency as

$$\nu_{\mathrm{th}} = \frac{ne^4}{16\pi\epsilon_0^2 m^2 v_{\mathrm{th}}^3} = \frac{ne^4}{16\pi\epsilon_0^2 m^{1/2} T^{3/2}}, \tag{2.5}$$

where the main takeaway is that the thermal collision frequency scales as $T^{-3/2*}$.

These scalings play an important role during a tokamak disruption. The electrical conductivity σ scales as $1/\nu_{\mathrm{th}}$, which gives a temperature scaling according to $\sigma \sim T^{3/2}$, so that a drop in temperature is accompanied by a drop in the conductivity. The conductivity after the temperature drop has a major impact on the dissipation rate of the current, and thus on the electromagnetic forces exerted on the machine. In addition, as the current in an inductive system can not change instantly, a fast drop in the conductivity has to be compensated by a large induced electric field[†].

Consider now a superthermal electron (with $v \gg v_{\mathrm{th}}$) moving through the plasma in the presence of such an induced electric field. The relative velocity compared to particles in the thermal bulk is then dominated by the velocity v, and the drag force therefore scales as $F_{\mathrm{drag}} \sim mv\nu \propto 1/v^2$. Thus, for electrons with a velocity higher than a critical speed at which the acceleration force due to the electric field exceeds the drag force, the electric field can quickly accelerate the light electrons in the plasma to extremely high energies, forming a beam of runaway electrons, as will be discussed in more detail later in section 2.2.2. Before turning to the details of the runaway electron phenomenon, we give an overview of the kinetic equation, and in particular the so-called Coulomb collision operator, needed to rigorously model Coulomb collisions in a kinetic framework.

*We adopt the convention in plasma physics to absorb the Boltzmann factor k_{B} in the temperature, so that T has the dimension of energy.

†This is quite similar to the high voltages that may occur when one disconnects the power supply from an ordinary coil, as the reader might be familiar with from circuit theory.

2.2 The kinetic equation

In a kinetic model, a particle species in a plasma is described by the distribution of this species in position and velocity space, $f(\mathbf{r}, \mathbf{v}, t)$ (Chen, 1974). As $\mathbf{r}$ and $\mathbf{v}$ both represent three variables each, the distribution function is a function of seven variables. It is customary to normalize the distribution function so that its integral over the velocity space gives the particle density,

$$n(\mathbf{r}, t) = \int f(\mathbf{r}, \mathbf{v}, t) d\mathbf{v}. \tag{2.6}$$

The evolution of the distribution function is governed by the equation referred to as the *Boltzmann equation* or *kinetic equation*, which has the form (Chen, 1974)

$$\frac{\partial f}{\partial t} + \mathbf{v} \cdot \nabla f + \frac{\mathbf{F}}{m} \cdot \frac{\partial f}{\partial \mathbf{v}} = \left(\frac{\partial f}{\partial t} \right)_{\mathrm{c}} + S. \tag{2.7}$$

Here, ∇ is the gradient in position space, $\partial/\partial\mathbf{v}$ is the gradient in velocity space, and $\mathbf{F}$ is the force acting on the particles, usually the electromagnetic force $\mathbf{F} = Ze(\mathbf{E} + \mathbf{v} \times \mathbf{B})$, where Z is the charge number of the particle species. The right hand side contains the effect on the distribution function caused by collisions via the so-called *collision operator* $\left(\frac{\partial f}{\partial t}\right)_{\mathrm{c}}$. The source term S represents changes in the total number of particles, for example caused by ionization or recombination (where a free electron is caught by an ion). The left hand side may be recognized as the total time derivative df/dt of the distribution function, i.e. the time derivative in a frame of reference following the particles in the six-dimensional phase space, by invoking the chain rule, and recognizing that $d\mathbf{v}/dt = \mathbf{F}/m$ from Newton's second law. The kinetic equation can therefore be regarded as a mathematical formulation of the following rather intuitive statement: the distribution function in the frame advected along collisionless particle trajectories in phase space can only change due to collisions and sources.

2.2.1 The Fokker-Planck Coulomb collision operator

When deriving an expression for the collision operator for Coulomb collisions, the fact that the dynamics is dominated by small angle collisions makes it possible to describe the dynamics using a *Fokker-Planck collision operator*, which has the form (Rosenbluth, MacDonald & Judd, 1957; Helander & Sigmar, 2005)

$$\left(\frac{\partial f}{\partial t} \right)_{\mathrm{c}} = C(f) = \sum_k \sum_l \frac{\partial}{\partial v_k} \left[-\frac{\langle \Delta v_k \rangle}{\Delta t} f + \frac{\partial}{\partial v_l} \left(\frac{\langle \Delta v_k \Delta v_l \rangle}{2\Delta t} f \right) \right]. \tag{2.8}$$

The first term can be interpreted as a friction force, a form of advection in velocity space, and the second term describes a diffusion process in velocity space. The expression $\langle \Delta v_k \rangle$ should be understood as the expectation value of the velocity change along direction $k \in (x, y, z)$ during a short time Δt along a particle trajectory, due to the collisional contribution from all other particles. These expectation values can be evaluated based on a calculation of the velocity change in the single particle

collision depicted in figure 2.1b), assuming small deflection angles. Next, the number of collisions with a given velocity and impact parameter of the incident particles is calculated, in terms of the distribution function of the incident species. Once these quantities are known, the expectation value for the total velocity change can be obtained by integrating their product over velocity space and impact parameters.

If there are multiple species $b_1, b_2, ..., b_n$ colliding with species a, the total collision operator for species a is given by the sum

$$C_a(f_a) = \sum_{k=1}^{n} C_{ab_k}(f_a, f_{b_k}). \tag{2.9}$$

The notation C_{ab_k} should be interpreted as the collision operator for collisions of species a against species b_k, and f_a, f_{b_k} are the distribution functions for species a and b_k, respectively.

In many cases, deriving the terms on the right-hand side of equation (2.8) can be simplified by certain assumptions for the distribution function of the background species. One such case is collisions between particles of disparate speeds, e.g. collisions between electrons (denoted e) and ions (denoted i) with similar temperatures. The large mass ratio implies the ions move much slower, and the distribution function f_i can therefore be approximated by a delta function around $v' = 0$. The resulting collision operator for electron-ion collisions takes the form (Helander & Sigmar, 2005)

$$C_{ei} = \nu_{ei}(v)\mathcal{L}(f_e), \tag{2.10}$$

where the electron-ion collision frequency is $\nu_{ei}(v) = n_i Z_{\text{eff}} e^4/(4\pi m_e^2 \epsilon_0^2 v^3)$, $\mathcal{L}(f_e)$ is the Lorentz operator, and the *effective ion charge* Z_{eff} (given in terms of the elementary charge) is defined as (Helander & Sigmar, 2005)

$$Z_{\text{eff}} \equiv \frac{\sum_k \sum_l n_{b_k l} Z_{b_k l}^2}{\sum_k \sum_l n_{b_k l} Z_{b_k l}}, \tag{2.11}$$

where $n_{b_k l}$ and $Z_{b_k l}$ are the density and charge number respectively of charge state l of ion species b_k.

The Lorentz scattering operator is equal to the angular part of the Laplacian operator in velocity space, meaning that C_{ei} describes a diffusion process on a sphere in velocity space at constant speed. As a result, only the direction of the electrons are changed by collisions with the massive ions. In spherical coordinates, with θ and ϕ denoting the polar and azimuthal angle, respectively, the Lorentz scattering operator can be expressed as

$$\mathcal{L}(f_e) = \frac{1}{2}\left[\frac{1}{\sin\theta}\frac{\partial}{\partial\theta}\left(\sin\theta\frac{\partial f_e}{\partial\theta}\right) + \frac{1}{\sin^2\theta}\frac{\partial^2 f_e}{\partial\phi^2}\right]. \tag{2.12}$$

The above approximation based on the disparate speeds of the colliding particles is not valid for electron-electron collisions. However, in many cases, such as the ones considered in this thesis, the electron distribution is dominated by a bulk population in thermal equilibrium, which can be used to simplify the collision operator. In a collisionally dominated, relativistic plasma, the equilibrium state is the Maxwell-Jüttner distribution (referred to as a Maxwellian for short). Thus, we divide the

electron distribution function into a Maxwellian part, f_{e0}, and a non-Maxwellian part, $f_{e1} = f_e - f_{e0}$, containing far fewer particles than f_{e0}.

The collision operator can be shown to be bilinear (Helander & Sigmar, 2005), so that the collision operator can be expanded as

$$C_{ee}(f_{e0} + f_{e1}, f_{e0} + f_{e1}) = C_{ee}(f_{e0}, f_{e0}) + C_{ee}(f_{e0}, f_{e1}) + C_{ee}(f_{e1}, f_{e0}) + C_{ee}(f_{e1}, f_{e1}). \tag{2.13}$$

The first term vanishes, as the collision operator for collisions between two Maxwellians with the same temperature and average velocity is zero (Helander & Sigmar, 2005). If f_{e1} is small compared to f_{e0}, the last, nonlinear, term can also be neglected. The two remaining terms now comprise a *linearised electron-electron collision operator*. The first of these, called the *field particle term*, describes the effect on the Maxwellian bulk from collisions with the small non-Maxwellian population. The second, called the *test particle term*, describes the effect on the non-Maxwellian population from collisions with the Maxwellian.

If one is primarily interested in the evolution of the small non-Maxwellian part, it is usually sufficient to only keep the test particle term $C_{ee}(f_{e1}, f_{e0})$. Combined with the impact from electron-ion collisions, the collision operator describing the dynamics of the non-Maxwellian population then takes the form (Helander & Sigmar, 2005)

$$\begin{aligned} C_{e1}(f_{e1}) &= C_{ei}(f_{e1}) + C_{ee}(f_{e1}, f_{e0}) \\ &= \nu_{ei}\mathcal{L}(f_{e1}) + \nu_{\mathrm{D}}^{ee}\mathcal{L}(f_{e1}) + \frac{1}{v^2}\frac{\partial}{\partial v}\left[v^3\left(\frac{1}{2}\nu_{\mathrm{s}}^{ee}f_{e1} + \frac{1}{2}\nu_{||}^{ee}v\frac{\partial f_{e1}}{\partial v}\right)\right]. \end{aligned} \tag{2.14}$$

Here, the terms describe angular scattering, frictional drag, and a parallel velocity space diffusion, respectively. The collision frequencies ν_{ei}, ν_{D}^{ee}, ν_{s}^{ee} and $\nu_{||}^{ee}$ relevant in a tokamak disruption in general contain contributions from both free and bound electrons, as the temperature becomes low enough that the plasma partially recombines, and the frequencies are thus complicated by the quantum mechanical properties of the partially ionized ions and atoms (Hesslow *et al.*, 2018*a*). Full expressions for the collision frequencies in the presence of partially ionized species are given in section 5.4.1. However, for a non-relativistic, fully ionized plasma, they reduce to the relatively simple expressions

$$\nu_D^{ee} = \hat{\nu}_{ee}\frac{\mathrm{erf}(x) - G(x)}{x^3}, \tag{2.15}$$

$$\nu_S^{ee} = 4\hat{\nu}_{ee}\frac{G(x)}{x}, \tag{2.16}$$

$$\nu_{||}^{ee} = 2\hat{\nu}_{ee}\frac{G(x)}{x^3}, \tag{2.17}$$

$$\hat{\nu}_{ee} = \frac{n_e e^4 \ln\Lambda}{4\pi\epsilon_0^2 m_e^2 v_{\mathrm{th}}^3}. \tag{2.18}$$

The dimensionless factor $\ln\Lambda$ is the so-called *Coulomb logarithm*, typically of order 10^1, and provides a measure of the impact of small angle collisions compared to large angle collisions (Chen, 1974).

We may note here that the average friction force on a particle, $-m_e v \nu_S^{ee}$, is proportional to the so-called Chandrasekhar function,

$$G(x) = \frac{\mathrm{erf}(x) - x\mathrm{erf}'(x)}{2x^2}, \tag{2.19}$$

where erf is the error function and $x = v/v_{\mathrm{th}}$ is the normalized speed (Helander & Sigmar, 2005). This function decreases as $1/x^2$ for large x, in line with what we found for F_{drag} in the qualitative analysis of section 2.1. This fact gives rise to the runaway phenomenon, to which we now turn our attention.

2.2.2 The runaway phenomenon

The runaway phenomenon can be understood by studying the velocity dependence of the drag force felt by an electron moving through the plasma, the form of which is illustrated in figure 2.2. This non-monotonic velocity dependence means that, in the presence of an accelerating electric field E, once a particle has gained a speed higher than a critical speed, marked as v_{c} in figure 2.2, the drag force will never balance the accelerating force. The particle can then continue accelerating to extremely high energies. This phenomenon is called the *runaway phenomenon*, and electrons with a speed larger than v_{c} are called *runaway electrons* (Helander & Sigmar, 2005). For such electrons, the energy gain is only limited by the energy losses due to synchrotron radiation and bremsstrahlung, which become significant at very high energies (Hirvijoki *et al.*, 2015; Decker *et al.*, 2016; Embréus, Stahl & Fülöp, 2016).

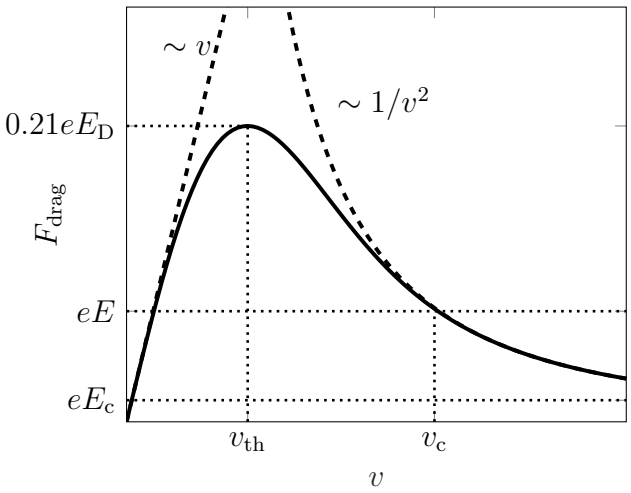

Figure 2.2: Illustration of the drag force felt by an electron moving through a plasma as a function of velocity. The presence of an accelerating electric field E creates a runaway region at velocities larger than v_{c}, where the drag force becomes weaker than the accelerating electric force. The Dreicer field E_{D} and the critical electric field E_{c} are also marked.

If the electric field becomes large enough, the accelerating force will be stronger than the maximum friction force. When this happens, all electrons become runaways. An estimate of the electric field required for this to happen can be obtained

by inserting $v = v_{\mathrm{th}}$ in the asymptotic expression for the drag force at high velocities. The electric field E_{D} corresponding to this force is called the *Dreicer electric field* and is given by (Dreicer, 1959; Connor & Hastie, 1975)

$$E_{\mathrm{D}} = \frac{e^3 n \ln \Lambda}{4\pi\epsilon_0^2 T}. \tag{2.20}$$

When considering the full expression for the drag force, it can be shown that the electric field at which all electrons become runaways is approximately equal to $0.21E_{\mathrm{D}}$ (Helander & Sigmar, 2005).

As the electron speed is limited by the speed of light, one may anticipate from the classical treatment that the drag force does not go all the way down to zero at high velocities. This sets a lower limit on the electric field necessary for the existence of runaway electrons. A relativistic treatment in the high energy limit shows that, in a fully ionized plasma, neglecting energy losses from synchrotron radiation and bremsstrahlung as well as the energy dependence of the Coulomb logarithm[‡], the drag force approaches the force corresponding to the Connor-Hastie critical electric field (Connor & Hastie, 1975; Helander & Sigmar, 2005),

$$E_{\mathrm{c}} = \frac{e^3 n \ln \Lambda}{4\pi\epsilon_0^2 m c^2}. \tag{2.21}$$

During normal tokamak operation, due to the very high conductivity, an electric field of the order of 1 mV/m is sufficient to drive the plasma current, which is usually not high enough to enable runaway generation. The situation might however be different in the case of a disruption, where the plasma suddenly cools (Hender *et al.*, 2007). Typically, the temperature drops in the thermal quench by about three orders of magnitude, resulting in a decrease in the conductivity by a factor of the order of $10^{-4} - 10^{-5}$ (recall the $\sigma \sim T^{-3/2}$ scaling from section 2.1). On the short time scale of the temperature drop, the current density is essentially constant, so that $E \sim 1/\sigma$. The electric field thus increases by a factor of $10^4 - 10^5$, and can become much larger than E_{c}, so that runaways can be generated. However, in order for a runaway current to actually form, there must be some mechanism feeding electrons to the velocity space region above the critical velocity for runaway acceleration. Depending on the circumstances, a number of such mechanisms may be present in tokamak disruptions, as described below. Quantitative models for these mechanisms are given in chapter 5.4.

The runaway generation mechanisms can be divided into two different types: *primary generation* or *seed generation*, that is independent of the number of runaway electrons present, and *secondary generation* or *avalanche generation*, which amplifies an existing runaway seed. An example of the former is the *Dreicer mechanism* (Dreicer, 1959). This mechanism relies upon the fact that the velocity distribution tends to equilibrate collisionally towards a Maxwellian, with a high energy tail above

[‡]It should however be mentioned that the energy losses from synchrotron radiation and bremsstrahlung result in an increase in the effective friction force at momenta $p \gg m_e c$, increasing its minimum value to some extent (Aleynikov & Breizman, 2015). The effective critical electric field is also affected by the presence of bound electrons, as well as the energy dependence of the Coulomb logarithm, as derived by Hesslow *et al.* (2018*b*).

the critical velocity. When this part of the distribution can run away, as particles accelerate to higher energies, the electron bulk will re-equilibrate and "fill out" the depleted tail, resulting in a continuous runaway generation.

The *hot-tail* mechanism of runaway generation occurs because it takes a finite time for the tail of the initially hot Maxwellian velocity distribution to equilibrate with the much lower temperature rapidly obtained by the bulk electrons during the thermal quench (Helander *et al.*, 2004; Smith *et al.*, 2005; Smith & Verwichte, 2008). The equilibration of the tail of the distribution is slower than that of the bulk due to the velocity dependence of the collision frequency derived in section 2.1. The tail of the distribution might therefore temporarily form a non-Maxwellian electron population at superthermal energies. When the electric field increases at the start of the current quench, a part of this superthermal population may remain at velocities larger than the critical velocity, and in that way become runaways before they have time to thermalise. This mechanism is illustrated in figure 2.3, showing the evolution of the angle-integrated distribution function during a disruption, as simulated by the numerical tool DREAM described in chapter 5. As opposed to other mechanisms, the hot-tail generation is only present during the initial part of the disruption.

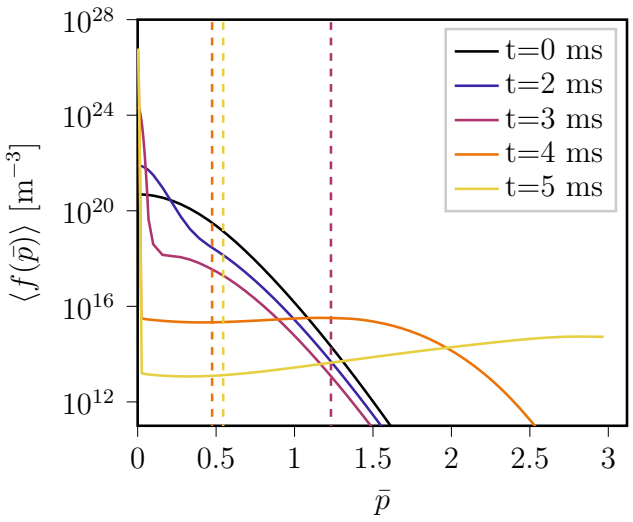

Figure 2.3: Illustration of the hot-tail mechanism, showing a representative evolution of the angle averaged electron momentum distribution $\langle f(\bar{p})\rangle$ as a function of the normalized momentum $\bar{p} = p/(m_e c)$. The vertical dashed lines indicate the runaway threshold momentum (initially outside the scale). The tail of the initially hot Maxwellian distribution (black line) takes a finite time to equilibrate to the dropping temperature of the bulk electrons. As the electric field increases, part of the distribution is therefore "caught" above the runaway threshold momentum, and is accelerated to higher momenta. The data is extracted from the disruption simulation studied in figure 5.6 a) in Vallhagen (2021).

In non-nuclear experiments, e.g. using pure protium plasmas, the Dreicer and hot-tail mechanisms are the only primary runaway generation mechanisms. During nuclear operation, however, the power will be generated by fusing deuterium and tritium, with the latter being β^--radioactive. Part of the energy spectrum of the electron released during the β^--decay may fall within the runaway region, providing another source of runaway generation (Martín-Solís, Loarte & Lehnen (2017), Paper

K). Another runaway generation mechanism present during nuclear operation comes from the activation of the wall due to the bombardment by neutrons released in the fusion reactions. This bombardment makes the wall radioactive, causing it to emit γ-photons. These γ-photons can be Compton scattered against electrons in the plasma, transferring enough energy to an electron to accelerate it over the runaway threshold (Martín-Solís, Loarte & Lehnen, 2017). This mechanism also applies mostly to plasmas consisting of a mixture of deuterium and tritium. It may however sometimes also play a role in pure deuterium plasmas, despite the much smaller reaction cross section of deuterium-deuterium fusion reactions and lower energy of the released neutrons (Ekmark *et al.*, 2025).

Finally, the runaway generation by the above mechanisms may be amplified by the *avalanche mechanism*. This mechanism generates runaways through collisions of existing runaways with slower electrons in such a way that both electrons have final velocities larger than the critical one after the collision (Sokolov, 1979; Rosenbluth & Putvinski, 1997; Embréus, Stahl & Fülöp, 2018). As the energies of the runaway electrons are much higher than the ionization energy of the ions in the plasma, bound electrons may also contribute to the avalanche process. In fact, it has recently been shown that an increase in the fraction of bound electrons might substantially enhance the avalanche. The reason for this is that the bound electrons contribute to the number of target electrons to practically the same extent as the free electrons, while their contribution to the drag force is smaller than that from free electrons at high electric fields (Paper **I**).

Chapter 3

Overview of tokamak disruption

With the theoretical background from the previous chapter covered, we are now ready to move on to a more detailed description of the main topic of this work, namely disruptions. These events are a type of operational failure in a tokamak, where the plasma suddenly cools. While disruptions present a range of concerns already in present-day tokamaks, the larger amount of energy (in the GJ range) released in a reactor scale tokamak disruption make these events the potentially most severe threat to the future of fusion energy based on the tokamak design (Schuller, 1995; Hender *et al.*, 2007). A particular concern is the runaway electron generation, especially due to the runaway avalanche mechanism. This process is exponentially sensitive to the initial current, making it a serious threat to future devices, which are expected to operate at higher current than present day devices.

This chapter focuses on the qualitative features of disruptions and various potential mitigation strategies, while quantitative theoretical models for the various phenomena at play are given in chapters 4 and 5. The chapter starts with a description of the typical triggering and onset mechanisms in section 3.1, followed by a description of the phases of a disruption in section 3.2. It then continues by detailing related potential damage to the device in section 3.3, with an emphasis on the requirements for disruption mitigation in ITER. Next, we discuss disruption mitigation by massive material injection in section 3.4, focusing on shattered pellet injection, which is the currently favoured approach and so studied in this thesis. Finally, we briefly cover a couple of alternative disruption mitigation strategies in section 3.5.

3.1 Triggering mechanisms and onset

Disruptions are caused by the plasma confinement being subject to an unstable perturbation. These events are closely related to the onset of *magnetohydrodynamic (MHD) instabilities* (Wesson, 2011; Schuller, 1995), as described below.

On flux surfaces where the safety factor q is irrational, the field line never connects to itself, and then a single field line traces out the whole flux surface. This can be used to illustrate the magnetic field geometry with Poincaré-plots, some examples of which are shown in figure 3.1. These plots are obtained by following a magnetic field line and adding a point to the plot every time the field line crosses a given

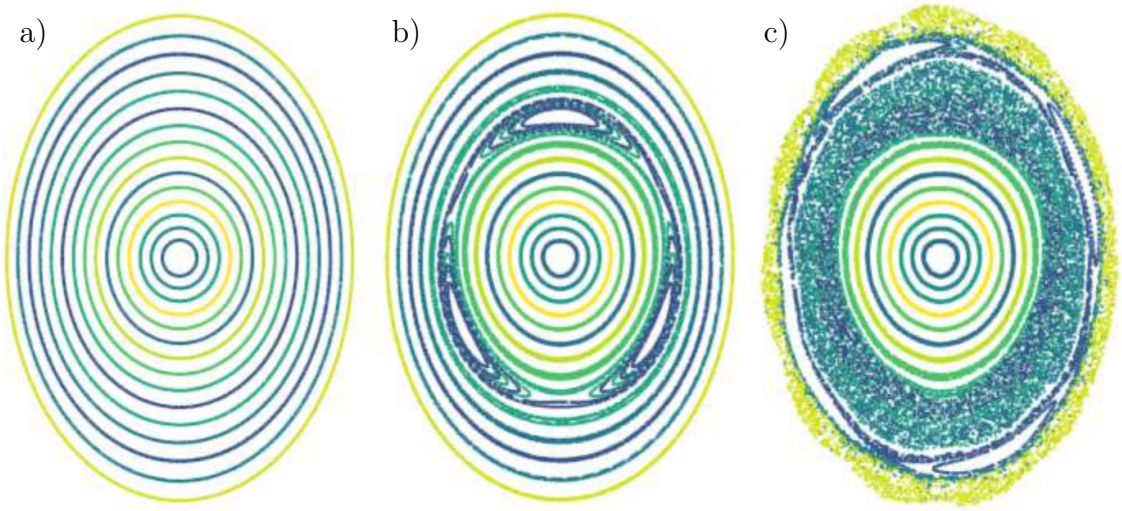

Figure 3.1: Poincaré-plots illustrating the stochastisation of a magnetic field in connection to a disruption, a) unperturbed magnetic field, b) creation of magnetic islands at the flux surface where $q = 3/2$, and c) stochastisation of the magnetic field due to overlapping of islands centered at different rational flux surfaces. Figure adapted from Svensson (2020).

poloidal plane. The resulting illustration of an unperturbed plasma equilibrium is shown in figure 3.1a).

The instabilities are related to perturbations of the plasma on flux surfaces where q is a low-order rational number, referred to as *rational flux surfaces* (Wesson, 2011). On these flux surfaces, the field lines connect with themselves after a few toroidal revolutions, making these surfaces more susceptible to perturbations. The instabilities are often induced by reaching a critical magnitude of a pressure gradient or current density, leading to a growing perturbation of the magnetic field. This can be caused by e.g. an influx of impurities into the plasma, which may (locally) cool the plasma to the $\sim 10 - 100\,\mathrm{eV}$ range typically sufficient to trigger a disruption (Schuller, 1995). The impurities might originate from an unintended influx of particles from the wall, or from a deliberate injection of impurities attempting to control the energy loss in order to minimize the damage to the device (Ward & Wesson, 1992; Hollmann *et al.*, 2015).

Perturbations to the magnetic field tend to create island-like magnetic field structures in the vicinity of the rational flux surfaces, centered around the points originally passed by the perturbed field lines. Such structures are illustrated in figure 3.1b) for the case with $q = 3/2$. As such islands are formed and grow on different rational flux surfaces, they might become large enough to overlap with each other. At this point, the magnetic field lines reconnect with each other in a rather chaotic way, causing a stochastisation of the magnetic field (Wesson, 2011). When this happens, the field lines are no longer limited to single flux surfaces, but instead ergodically fill volumes, as illustrated in figure 3.1c). Magnetic reconnection events may also be caused by other types of overlapping MHD mode structures than the ones illustrated here (Schuller, 1995), but the main principles are similar. This ergodicity of the field lines strongly reduces the plasma confinement, potentially initiating a disruption, as described in the next subsection.

3.2 Typical phases

As the particles follow the ergodic magnetic field lines across the equilibrium flux surfaces, the particle transport and thermal conductivity across the plasma is greatly increased (Schuller, 1995; Hender *et al.*, 2007). If the instability was triggered by an influx of impurities, the impurities also contribute directly to the thermal energy loss by emitting radiation. A major part of the impurity radiation is emitted in the form of line radiation as partially ionized species fall back to lower energy levels after collisional excitation by the surrounding electrons. Another contribution comes from the radiative release of the potential energy change when a free electron recombines with an ion. Moreover, the introduction of material with atomic charge $Z \gtrsim 10$ (hereafter referred to as *high-Z impurities*) increases the bremsstrahlung corresponding to the momentum exchange during collisions between charged particles, which might contribute significantly to the thermal energy losses at the high initial temperatures. These mechanisms may cause a rapid cooling of the plasma from several keV down to ~ 10 eV over a millisecond time scale. This phase of the disruption is called the *thermal quench*.

An illustration of a typical disruption evolution is shown in figure 3.2, where the panels show the qualitative evolution of the temperature and electric field (a), and current (b). The thermal quench is marked here by a red shaded area.

During the thermal quench phase, the magnetic reconnection event breaking up the flux surfaces also causes a rapid transport of poloidal magnetic flux, leading to a flattening of the current density profile (Schuller, 1995; Boozer, 2018). The corresponding drop in the internal inductance of the plasma is usually compensated for by a temporal spike in the plasma current, as shown in figure 3.2b). The spike occurs as the magnetic helicity must be conserved on the short time scale of the magnetic reconnection (Boozer, 2018). Helicity is here defined as the integral of the poloidal magnetic flux ψ_p with respect to the toroidal magnetic flux ψ_t, $-2\int \psi_\mathrm{p} d\psi_\mathrm{t} d\theta d\phi/(2\pi)^2$, where θ and ϕ are the poloidal and toroidal angles.

As the speed at which particles follow the perturbed field lines is, on average, of the order of the thermal speed, the cross-field transport due to magnetic perturbations decreases with decreasing temperature. In addition, the flux surfaces start to re-heal towards the end of the thermal quench, and the transported losses are therefore greatly reduced after the thermal quench (Ward & Wesson, 1992). At this point, the energy balance, and hence the temperature, is essentially determined by impurity radiation and the Ohmic heating by the plasma current.

The cooling leads to a rapid drop in the plasma conductivity, due to the conductivity scaling as $T^{3/2}$, as shown in section 2.1. The thermal quench is usually very fast compared to the current diffusion time scale, which is set by the plasma conductivity and the scale and mechanical structure of the device. The current can therefore not change significantly during the thermal quench, so a large electric field must be induced in order to maintain the current. After this, the electric field starts to decay by diffusing out of the plasma, leading to a drop in the plasma current, a phase called the *current quench* (Hender *et al.*, 2007), marked by a green shaded area in figure 3.2.

The electric field induced during a disruption is usually well above the critical

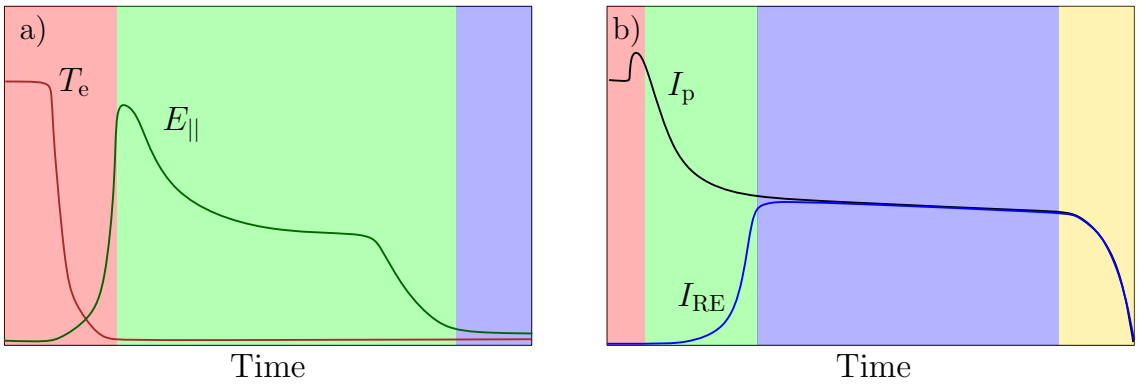

Figure 3.2: Illustration of the general features of a disruption. The panels show a) the drop of the electron temperature (T_e) and resulting increase and decay of the field line parallel electric field ($E_{||}$), and b) the decay of the plasma current (I_p) and growth and loss of the runaway current I_{RE}. The shaded areas indicate the time spans of the thermal quench (red), current quench (green), runaway plateau (blue), and runaway loss (yellow) respectively.

electric field for runaway electron generation, leading to the conversion of part of the original plasma current into a current carried by runaway electrons (Hender *et al.*, 2007). Eventually, the Ohmic current will decay and the runaway current becomes the only current remaining in the plasma. Due to the low collisionality of runaway electrons, this current decays much more slowly than the Ohmic current, such that a sufficiently large runaway current may form a *runaway plateau*. This is shown in the blue shaded area of figure 3.2b). The slow dissipation of the runaway current usually continues until the position control of the plasma is lost and the plasma impacts the wall (unless it is terminated by an artificially induced major MHD instability, see section 3.5).

The final termination of the runaway plateau is typically caused by the fact that the decay of the plasma current makes the plasma vertically unstable (Gruber *et al.*, 1993; Taylor *et al.*, 1999; Lehnen *et al.*, 2013). This vertical instability can be explained by the inductive coupling between the plasma and the surrounding conducting structures (Kiramov & Breizman, 2017). The decay of the plasma current induces currents in the surrounding structures. If the current induced in the upper and lower conducting structures are somewhat asymmetrical (e.g. due to slight up-down asymmetries in the plasma configuration), the forces due to these currents may vertically shift the position where the net force on the plasma cancels. This shift in the equilibrium position reinforces the asymmetry in the currents induced by the decay of the plasma current, leading to a vertical instability.

In a device with a highly conducting wall (such as ITER), the plasma position is strongly correlated with the plasma current (Kiramov & Breizman, 2017), so that the plasma edge is expected to always touch the wall at a similar current for a given initial configuration ($\sim 10\,\mathrm{MA}$ for a 15 MA ITER plasma) (Martín-Solís *et al.*, 2022). However, some displacement also takes place at constant plasma current, such as during a runaway plateau, on a time scale similar to the resistive time scale of the tokamak wall in a realistic setting (Bandaru *et al.*, 2025). Once the flux surfaces carrying the runaway electrons reach the wall, the runaway electrons are

led to intersect the wall by the field lines, depositing their energy upon impact, a process referred to as *scrape-off*. This is typically the main mechanism behind the *runaway loss* phase (yellow shaded area in figure 3.2), which continues until the magnetic axis reaches the wall and the last runaway electrons are lost.

It should be mentioned that the evolution described above is representative only for cases with a sufficiently fast runaway generation, such that a large runaway beam is formed before the innermost flux surfaces are scraped off, slowing down the vertical motion and enabling the formation of a runaway plateau. However, in cases with a slower runaway generation, the scrape-off process and runaway generation may overlap, potentially scraping off all the flux surfaces before a runaway plateau is formed. The prospect of achieving such a scenario in ITER is discussed in paper **G**.

3.3 Vessel loads and mitigation requirements

The various phases of a disruption all pose their own threats to the device, imposing different requirements on a successful mitigation system. We here give a brief overview of the potentially harmful mechanisms at play, and the corresponding requirements for successful disruption mitigation in an ITER-sized tokamak, as summarized by Hollmann *et al.* (2015), with some updates presented by Lehnen & the ITER DMS task force (2021).

The sudden deposition of the released thermal energy content during the thermal quench might cause melting of the plasma facing components if the heat loads are localised. It is therefore necessary for the disruption mitigation system to ensure that a major part of the thermal energy is radiated homogeneously. In ITER, the homogeneously radiated fraction should be larger than 90% of the initial thermal energy content. The time frame between the detection of an emerging disruption and the onset of a naturally occurring MHD-induced thermal quench is expected to be about 20 ms, which sets the required reaction time scale for the disruption mitigation system. Note, however, that any perturbations of the plasma caused by the mitigation systems can accelerate the growth of MHD instabilities and/or aggravate the runaway electron issue, and the external interventions must therefore be implemented with care.

During the following current quench, the decay of the plasma current and motion of the plasma induces currents in the surrounding structures. The interaction between these currents and the toroidal and poloidal magnetic field gives rise to potentially harmful forces on the structures. As the position control of the plasma is lost and the plasma moves towards the wall, part of the plasma current might flow through the surrounding structures. This part of the plasma current forms a so-called *halo current*, which can also contribute to the vessel loads. The induced currents increase with shorter current quench times, while the risk of substantial halo currents increase with longer current quench times, giving both an upper and lower limit on the acceptable current quench time. In ITER, the current quench time should preferably be longer than 50 ms, with a hard limit at 35 ms, and shorter than 150 ms.

Finally, if a runaway current is formed, a major part of the runaway current

can impact the wall when the plasma control is fully lost. This would cause a substantial localised melting, and possibly also damage deeper into the underlying structures. In ITER, the runaway current remaining in the plasma upon wall impact should therefore not exceed 150 kA Lehnen & the ITER DMS task force (2021). This threshold is expressed in terms of the runaway current rather than the kinetic energy of the runaways, as the magnetic energy associated with the current is typically much larger than the kinetic energy of the runaways. The energy associated with the current may then be converted to kinetic energy by the electric field induced as the runaway beam impacts the wall and the current rapidly decays Putvinski *et al.* (1997*a*); Loarte *et al.* (2011); Riemann, Smith & Helander (2012).

3.4 Disruption mitigation by massive material injection

We now move on to the main methods considered in order to achieve the disruption mitigation requirements mentioned in chapter 3.3. This is a very active field of research, to which this work aims to contribute. The strategies studied most extensively to date are based on various forms of material injection, and so-called shattered pellet injection has been chosen as the basis for the disruption mitigation system in ITER Lehnen *et al.* (2020); ITER organization. This chapter gives an overview of material injection in the context of disruption mitigation, leading up to the most advanced injection scheme suggested, the two-stage shattered pellet injection scheme, which is studied in papers **B**, **D**, **G** and **H**.

Massive material injection acts to mitigate disruptions in three main ways, corresponding to the requirements on the radiated fraction of the thermal energy, current quench time and runaway avoidance. Suitable materials for radiative dissipation of the thermal energy are noble gases such as neon or argon Hollmann *et al.* (2015). Also note that as long as some amount of the impurity is present, the radiation can be further enhanced by increasing the electron density by injecting e.g. hydrogen species, since the collisional excitation rate is proportional to the electron density. The quantity and composition of injected material can also be used to regulate the post-disruption temperature, which is roughly given by an equilibrium between the impurity radiation and the Ohmic heating. Since the current quench time is proportional to the conductivity, which in turn scales as $T^{3/2}$, the temperature essentially determines the current quench time.

Finally, the injected material might reduce the runaway generation due to the resulting electron density increase, leading to an increase in the critical electric field according to equation (2.21). It should however be noted that the usefulness of this method to reduce the runaway generation might be limited by the fact that if the injected quantity becomes too high, the cooling might be intense enough to cause a substantial recombination, which can severely increase the runaway avalanche, as mentioned in section 2.2.2 and discussed more thoroughly in paper **A**.

With the above general background about the purpose of massive material injection in mind, we now turn to the different injection schemes and methods proposed to deliver the injected material in the following sections.

3.4.1 Injection schemes

A particular difficulty for the disruption mitigation system is that the various requirements of the disruption mitigation are to some extent contradictory Hollmann *et al.* (2015). For the mitigation of the thermal loads, it would be beneficial to have an early large injection of strongly radiating material, such as argon or neon. Such injections could also substantially increase the free electron density, which would contribute to the collisional drag which limits the runaway generation. Large amounts of argon or neon might however result in a post-thermal quench temperature too low to give an acceptable current quench time. Moreover, they might also increase the runaway seed generation from the hot-tail mechanism, as well as enhance the subsequent runaway avalanche due to the presence of bound electrons.

The currently envisaged compromise is to inject large amounts of deuterium combined with a trace amount of argon or neon Breizman *et al.* (2019); Lehnen *et al.* (2020). The role of the deuterium would be to provide a source of electrons in order to limit the runaway generation and to enhance the radiation efficiency of the neon. The role of the neon would be to radiatively dissipate the thermal energy and to set a post-thermal quench equilibrium temperature within an acceptable range.

A recently suggested improvement to the above scheme is to divide the injection into two stages following rapidly after each other Nardon *et al.* (2020*b*). The first stage would then deliver the deuterium, and the second deliver the neon or argon. The aim of such a scheme would be to first cool the plasma by dilution down to the 100-1000 eV range by the pure deuterium injection, without perturbing the plasma pressure or current density enough to significantly accelerate the growth of MHD instabilities (introduced in section 1.2). The plasma would then be left at this temperature for a few milliseconds to let the full distribution equilibrate to a Maxwellian at this temperature. A final radiative thermal quench would then be triggered by injecting the argon or neon. The intermediate equilibration of the distribution is expected to produce a significant reduction of the hot-tail runaway generation. The radiated fraction of the thermal energy could also be significantly increased, as the magnetic perturbations would not become significant until the comparatively low temperature makes conducted losses subdominant to radiation losses. It was indicated in Nardon *et al.* (2020*b*) that it is possible to cool an ITER-like plasma by dilution down to ~ 100 eV without immediately triggering a major MHD instability. The runaway dynamics and radiation characteristics of such a two-stage SPI scheme is the subject of paper **B**.

For such a mitigation scheme to be successful, it is important to assimilate a large amount of deuterium over as much of the plasma volume as possible before the onset of the MHD instability. This poses strict requirements on the injection system, the design of which is discussed in the next section.

3.4.2 Injection techniques

The most straightforward injection method is *massive gas injection*, where the injected material is simply released into the tokamak in gaseous form, via a connector to a pressurized vault Hollmann *et al.* (2015). As the simplest proposed method to implement, it is the one most studied experimentally, and therefore also the-

oretically. The greatest advantage with this method is its simplicity, while the assimilation efficiency of the released gas is found to be rather poor in practice on larger machines, despite promising results on smaller machines Papp *et al.* (2016); Reux *et al.* (2015). Much of the material has been observed in both experiments and simulations to be stopped at the plasma edge and only slowly mix with the rest of the plasma. This can be understood as a result of the fact that as soon as the gas particles ionize, they become confined by the magnetic field, which, together with the pressure of the pre-existing plasma, restricts the gas penetration. The resulting strong cooling at the edge may induce substantial MHD activity, which may help to speed up the inward transport of injected ions but also lead to an unwanted increase in the conducted heat losses.

Another method that gives a faster, more efficient delivery of material to the plasma core, is to inject the material in the form of solid cryogenic pellets Hollmann *et al.* (2015). In this way, the material travels through the plasma in a neutral, solid form, while being continuously ablated by the hot background plasma, depositing material along the trajectory. The pellets are typically accelerated by a propellant gas and reach speeds of around 300-600 m/s. This is similar to many typical gas sound speeds, and therefore the arrival time of the pellets at the plasma is not significantly different compared to a gas injection from the same location. Note that injection of pellets (though typically slightly smaller and of hydrogen isotopes) is regularly performed on existing machines, including for purposes other than disruption mitigation, such as to fuel the plasma, regulate instabilities and for diagnostic purposes Pégourié & Picchiottino (1996); Milora *et al.* (1995).

There are, however, a number of disadvantages associated with disruption mitigation by pellet injection. Depending on the speed at which the pellet travels and the state of the plasma, the pellet may pass through the plasma without depositing all of its material. Besides making the injection less effective, the remaining pellet might damage the wall upon impact (Hollmann *et al.*, 2015). This problem is particularly relevant when a pellet is injected after the plasma has already been cooled in the course of the thermal quench.

One way to address this issue is to use an SPI (Baylor *et al.*, 2009; Breizman *et al.*, 2019). In an SPI, the pellet is shattered against a tilted plate before entering the plasma. The number of shards into which the pellet is shattered may be controlled (to some extent) by varying the pellet speed and the geometry of the shattering plate. Increasing the number of shards (for a fixed total amount of pellet material) increases the ablation rate, hence reducing the amount of material passing through the plasma without ablating. The increased ablation may be understood by the fact that shattering the pellet increases the total contact area with the plasma. Any leftover material striking the wall will also be spread over a larger area, reducing the risk of damaging the wall. The initial spread of the deposited material is also increased, lowering the risk of local peaking in the radiative heat loads before the material has homogenized through the plasma.

Since the SPI technique was first demonstrated at the DIII-D tokamak (Commaux *et al.*, 2010*a*), it has undergone a rapid experimental development (Commaux *et al.*, 2016; Baylor *et al.*, 2019; Combs & Baylor, 2018), and state of the art SPI systems are now installed at several tokamaks, including DIII-D (Meitner *et al.*,

2017), ASDEX Upgrade (Dibon *et al.*, 2023; Heinrich *et al.*, 2024), KSTAR (Park *et al.*, 2020) and JET (Baylor *et al.*, 2021). During the last years, these systems have been used for extensive experimental studies in support of the ITER disruption mitigation system (Herfindal *et al.*, 2019; Jachmich *et al.*, 2022; Schwarz *et al.*, 2023; Heinrich *et al.*, 2025), largely confirming the benefit of the SPI technique over other methods.

Due to these advantages, SPI has been chosen as the basis of the ITER disruption mitigation system Lehnen *et al.* (2020); ITER organization. However, the design and operation parameters of the ITER disruption mitigation system, such as the pellet composition, the number of pellets and their particle contents, the degree of shattering, timing aspects etc. remain open questions. In order to address these questions, it is important to be able to model the behavior of the pellet and its interaction with the background plasma. The theory basis for pellet modeling is the subject of chapter 4, and a full disruption modeling framework is summarized in chapter 5.

3.5 Other mitigation strategies

As discussed in chapter 6, it remains unclear whether the above material injection techniques are sufficient to avoid the formation of a large runaway electron current in reactor scale devices, while at the same time fulfilling the other requirements discussed in section 3.3. For this reason, alternative complementary mitigation strategies have recently been investigated (although not studied in this thesis). Two of the main such strategies which are currently under investigation are briefly described below.

3.5.1 Benign termination of runaway beam

A novel runaway mitigation strategy, which has recently gained much attention, is the possibility to safely terminate an existing runaway beam by distributing its impact over a large part of the vessel wall rather than a small spot, referred to as *benign termination*. This has been found to be possible at several tokamaks, including DIII-D (Paz-Soldan *et al.*, 2019), JET (Reux *et al.*, 2021), ASDEX Upgrade and TCV (Sheikh *et al.*, 2024), by the use of a massive hydrogenic SPI during the runaway plateau.

The mechanism behind benign terminations is still under investigation, but is believed to work as follows (Bandaru *et al.*, 2021; Paz-Soldan *et al.*, 2021): the pellet shards are effectively ablated by the runaway electrons, and the cooling due to the resulting density increase causes a major plasma recombination. As a result, the Alfvén speed c_A, determining the speed at which magnetic field perturbations propagate, is strongly increased. This enables a rapid growth of any MHD modes when excited. An instability may then either be triggered naturally or through deliberate action, for example by the current profile being hollow or the edge safety factor passing a low order rational number (typically $q = 2$). The latter can be achieved by driving a loop voltage to increase the runaway current, which is facilitated by the low collisionality in the recombined plasma, or by plasma compression following

a natural or induced vertical motion. Finally, the rapidly growing MHD instability gives rise to a violent magnetic reconnection event in a similar way as during the thermal quench (see section 3.1), leading to a fast transport of the runaway electrons to the wall along the stochastic field lines.

In addition to spreading the runaways over a large wall area, the loss of the runaway current induces an electric field inside the plasma, replacing the runaway current by an ohmic current. Thus, this technique helps avoid the conversion of the magnetic energy associated with the current to kinetic energy of the runaways; the former may then instead be ohmically dissipated over a longer time scale (Paz-Soldan *et al.*, 2021).

Open questions however remain regarding the scalability of this technique to reactor scale devices, and the compatibility of this mitigation strategy with injections before the thermal quench. For instance, ITER simulations by McDevitt & Tang (2023) have shown that the ohmic current replacing the runaway current upon its termination may be partly re-converted to a runaway current, in a similar way as the original runaway current was generated. The existence of trapped runaway electrons, which are not lost during the magnetic reconnection event, may provide a significant seed for this re-conversion. The amount of trapped runaways depends on the density of high-Z impurities, which provide an efficient angular scattering of the runaway electrons into the trapped region of momentum space. It may therefore be important that the hydrogenic SPI effectively purges any impurities present in the plasma as it enters into the runaway plateau. It has also been found that there is an upper limit on the plasma density providing access to benign termination (Paz-Soldan *et al.*, 2021; Sheikh *et al.*, 2024). This upper limit has been linked to the increased rate of ionization by runaway impact at high densities, eventually causing a net increase in the free electron density Hoppe *et al.* (2025). This may limit the amount of material which may be injected before the thermal quench while still allowing access to benign termination.

3.5.2 Runaway electron mitigation coil

An alternative suggested runaway mitigation method is to trigger a magnetic reconnection to de-confine the runaways by installing a helical coil inside the tokamak (Boozer, 2011; Smith, Boozer & Helander, 2013). Once the current quench starts, the inductive coupling between the plasma and the coil will then drive a current through the coil. The magnetic field thus created may, for an appropriately designed coil, directly give rise to island-like magnetic field structures similar to those which may be caused by MHD instabilities, as described in section 3.1. As with islands created by MHD instabilities, if they become large enough, they may overlap and lead to a magnetic reconnection.

This method extends previous attempts at deconfining runaway electrons using resonant magnetic perturbation coils actively driven by a power supply. Such perturbations have shown promising results on smaller devices such as JT-60 (Yoshino & Tokuda, 2000), TEXTOR (Lehnen *et al.*, 2008) and COMPASS (Mlynar *et al.*, 2018), but have been found to be insufficient to significantly reduce the runaway current in JET (Riccardo *et al.*, 2010). This may be attributed to the limited pen-

etration depth of the field generated by the coils, in combination with technical limitations on the maximum currents which can be provided by the power supply (Papp *et al.*, 2011*a*). These issues may be even more limiting in future reactor scale devices such as ITER (Papp *et al.*, 2011*b*). The current induced in the passive coil by the decaying plasma current may however be larger than is practically possible to produce using an active power source. Using a passive coil also has the benefit that the activation of the coil does not rely on disruption prediction.

Such runaway electron mitigation coils have been designed for several tokamaks, including DIII-D (Weisberg *et al.*, 2021), SPARC (paper **N**) and TCV (Battey *et al.*, 2025). Promising modeling results have been found using this approach for the DIII-D and SPARC tokamaks (Tinguely *et al.*, 2021; Izzo *et al.*, 2022; Tinguely *et al.*, 2023), and experiments are planned for the DIII-D and TCV tokamaks in the near future (Battey *et al.*, 2025). However, as with the benign runaway beam termination discussed in section 3.5.1, it remains uncertain how well this method scales to larger tokamaks. Studies have shown that it may be difficult to make the perturbations penetrate deep into the core even with a passive coil (Smith, Boozer & Helander, 2013), which may still limit their prospect of preventing runaway formation (paper **O**). Difficulties also remain regarding how to support the large magnetic forces on the coil (paper **N**), as it may carry currents of several hundred kiloamperes, and how to keep the coil circuit open in order to avoid unwanted perturbations during normal operation (Tinguely *et al.*, 2025).

Chapter 4

Pellet theory

When modeling pellet injections, for disruption mitigation as well as for other purposes, it is crucial to have an accurate theoretical understanding of the interactions of the pellet (or pellet shards) with the background plasma. When models for this interaction are included in a larger integrated framework, such as that presented in chapter 5, analytical models are preferred, due to their low computational cost. This chapter establishes the theoretical framework for deriving such models, leading up to the SPI model used in papers **B**, **D**, **G** and **H**, and preparing for the theory development in papers **C** and **E**.

A summary of the main dynamics of a pellet injected into a hot plasma is illustrated in figure 4.1. When the pellet enters the plasma, it is exposed to the plasma heat flux, carried mainly by electrons flowing along the magnetic field lines. This heat flux ablates the pellet, quickly leading to the formation of a nearly spherically symmetric neutral gas cloud around the pellet, which shields it from the heat flux of the background plasma and slows further ablation in a self-regulating manner. The flow of ablated material accelerates quickly within the sonic radius r_* where the flow speed reaches the speed of sound, beyond which the flow speed remains rather constant. The sonic radius also sets a characteristic length scale for the variation of the other quantities describing the gas cloud, as well as the incoming electrons from the background plasma inside the gas cloud. Further away from the pellet, at the ionization radius r_i, the ablated material is ionized, after which it takes the form of a plasmoid expanding mainly along the field lines, at a speed close to the speed of sound. This plasmoid also contributes to the shielding of the pellet to some extent.

The local excess pressure in the plasmoid reintroduces the issue of charge separation by the ∇B drift, and a subsequent $E \times B$ drift along the major radius direction, similar to the drift that would affect the whole plasma in the absence of the poloidal twist of the magnetic field lines, as discussed in section 1.1. This results in a displacement of the deposition of the ablated material from the position of the pellet. In addition, the $E \times B$ drift bends the plasmoid boundary in relation to the magnetic field lines, giving rise to a finite plasmoid shielding length with an asymmetry component (s_0 and δs in figure 4.1a), respectively). This asymmetry, together with gradients in the plasma, adds an asymmetric component to the pellet heating and, consequently, the ablation dynamics (as illustrated by dotted lines and arrows in

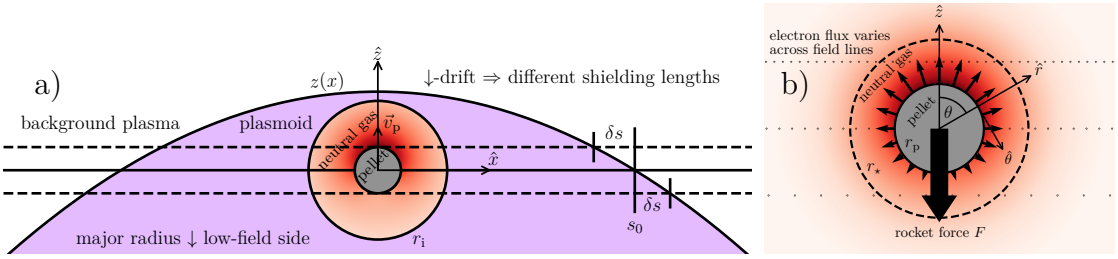

Figure 4.1: Illustration of the dynamics of a pellet exposed to a hot background plasma, also defining the coordinate system used throughout this chapter. a) The pellet (gray), neutral gas (red) and plasmoid consisting of recently ionized material (purple), drifting towards the low magnetic field side (downwards in the figure), in a coordinate system where the magnetic field lines are stretched out horizontally. b) A closer view of the pellet, including an illustration of the asymmetric heating, ablation, neutral cloud pressure and the resulting pellet rocket force. The proportions in the figure have been modified for visibility; in reality, $r_p \sim r_* \ll r_i \ll s_0$. Adapted from paper **F**.

figure 4.1b). As a result, the pellet is propelled by a rocket-like force, referred to as the *pellet rocket force*, towards the less heated side, which may significantly affect the pellet trajectory (as discussed in papers **E** and **F**).

In reality, some further complications arise in addition to the picture described above. One such complication is the partial separation of the cloud of drifting material into discrete plasmoids. The drifting of the ablated material is therefore commonly referred to as *plasmoid drift*. Several mechanisms have been proposed to play a role in forming this partial separation, such as the limited energy reservoir available on low-order rational magnetic flux surfaces Kaufmann *et al.* (1986); Pégourié & Dubois (1989) and the periodic passing of the ablation cloud front by the pellet Durst *et al.* (1990); Müller *et al.* (2002). It has also been suggested by Parks (1996) that the separation is related to the rotation of the plasmoid, caused by the $E \times B$ drift associated with the electrostatic potential gradient along the plasmoid radius. This rotation enables the growth of repeated Rayleigh-Taylor instabilities due to the centrifugal force in the frame of reference rotating with the plasmoid, displacing the ablation cloud from the pellet. In many theoretical models, however, these subtleties are not accounted for.

The rest of this chapter is divided into four parts. Section 4.1 provides a statistical model for pellet shattering, and section 4.2 describes the theoretical basis for pellet ablation calculations. Section 4.3 covers the theory of the cross-field drift underlying the model derived in paper **C**, and section 4.4 introduces the framework used for the calculation of the pellet rocket force in paper **E** and **F**.

4.1 Pellet shattering

An SPI starts with a pellet being accelerated and then shattered against a tilted plate, resulting in a plume of pellet shards of different sizes and velocities entering the plasma. While in reality the distribution of pellet shard sizes has a complicated dependence on the injection parameters such as the pellet size, velocity and shattering angle (Baylor *et al.*, 2019; Gebhart, Baylor & Meitner, 2020; Peherstorfer,

2022), one may estimate the shard size distribution by considering the fact that the pellet is initially mostly broken by shear stresses into a saucer-like structure (Parks, 2016). If the further break-up of the thin layers thus formed is approximated as a division by a large number of randomly and independently distributed perpendicular straight lines, the probability density $P(r_\mathrm{p})$ of the shard radius (or, rather, shard length scale) r_p takes the form (Mott & Linfoot (1943), a transcription is available in Mott & Linfoot (2006))

$$P(r_{p,k}) = k_p^2 r_{p,k} K_0(k_p r_{p,k}), \quad k_\mathrm{p} = \left(\frac{N_\mathrm{inj}}{6\pi^2 n_\mathrm{p} N_\mathrm{s}}\right)^{-1/3}, \tag{4.1}$$

where K_0 is the zeroth modified Bessel function of the second kind, the pellet is assumed to be shattered into N_s shards, n_p is the number density of the solid pellet material and N_inj is the total number of injected atoms. The parameter k_p can be interpreted as the inverse of the characteristic shard size. This distribution has a rather long tail towards large r_p, so that even if the pellet is shattered into many shards, a few larger shards, which may propagate deeper into the plasma before they are completely ablated, are typically present. Such a distribution of shard sizes has recently been used in several SPI modeling activities (Hu *et al.*, 2018; Matsuyama *et al.*, 2020; Nardon, Matsuyama & Lehnen, 2020), with N_inj and N_s being considered adjustable parameters.

4.2 Pellet ablation

Once the shards enter the plasma, they are continuously ablated, depositing their content along their trajectories. In essence, the number of particles ablated from a pellet or pellet shard during a given time interval is determined by the ratio of the heat flux reaching the pellet surface during this time interval and the sublimation energy per particle. However, on a very short timescale after the pellet is exposed to the plasma (of only a few μs), the finite flow of ablated material away from the pellet produces a dense cloud around the pellet that shields it from the heat flux from the plasma Pégourié (2007). The pellet ablation can therefore be regarded as a self-regulating process, balancing the heat flux coming from the plasma and the resulting build-up of the shielding cloud. The resulting quasi-stationary cloud size and ablation rate are such that only the ablation energy necessary for maintaining the cloud size reaches the pellet surface.

Directly above the pellet surface, the cloud is neutral and close to spherically symmetric. This neutral cloud typically has a thickness of the order of 1 cm, and a particle density of $10^{25} - 10^{26}$ m^{-3}. The pellet (or pellet shard) itself typically has a thickness of the order of a millimeter. At the edge of the neutral cloud, the material density falls and the temperature increases enough to begin to ionize the ablated material. The material takes the form of a confined cold plasma, whose subsequent expansion is therefore mostly aligned with the field lines.

There are three main mechanisms involved in the shielding of the pellet by the neutral cloud, although usually of quite different importance Pégourié (2007). With decreasing importance, these mechanisms are referred to as *gas dynamic shielding*,

electrostatic shielding and *diamagnetic shielding*. The gas dynamic shielding refers to the deposition of incident plasma energy by the collisional interaction with the neutral gas in closest proximity to the pellet (Parks & Turnbull, 1978; Parks, Leffler & Fisher, 1988; MacAulay, 1994; Fontanilla & Breizman, 2019; Parks, 2017). Collisions between the hot incident electrons and the new cold ablated plasma beyond the neutral cloud also contribute to some extent, typically referred to as *plasma shielding* (Pegourie *et al.*, 2002; Bosviel, Parks & Samulyak, 2021; Samulyak *et al.*, 2021). This effect is increased by the fact that once the ablated material ionizes, it forms a plasmoid expanding along the magnetic field lines, concentrating the shielding along the path taken by the incoming electrons. Due to its low density compared to the neutral cloud, its impact on the ablation rate is typically moderate (Parks & Turnbull, 1978; Pegourie *et al.*, 2002), although it may reduce the ablation rate by a substantial order unity factor at high magnetic fields (Bosviel, Parks & Samulyak, 2021; Samulyak *et al.*, 2021).

The energy deposition in the cloud occurs due to scattering, heat transfer to the cloud particles, and ionization and excitation of ions and atoms in the cloud, which then dissipate the energy by radiation (Pégourié, 2007; Lengyel *et al.*, 1999). It has however been estimated that, due to its relatively high density, the cloud might be substantially opaque to the resonant lines. A significant fraction of the radiation might therefore be trapped within the cloud, and the corresponding energy also contribute to the cloud heating (Morozov *et al.*, 2004; MacAulay, 1994).

Electrostatic shielding results from the different mobility of ions and electrons (Lengyel, Rozhanskij & Veselova, 1996; Pégourié *et al.*, 2004; Parks, 1996). Electrons in the background plasma initially flow into the ablation cloud much faster than the ions, due to their lower mass. This gives rise to a difference in charge between the ablation cloud and the surrounding plasma, and the corresponding electrostatic potential difference limits the heat flux into the ablation cloud.

Diamagnetic shielding occurs as there is a finite timescale for the magnetic field to diffuse into the cloud (Parks, 1980). The gyration of the ionized particles in the ablation cloud creates a magnetic field that opposes the background magnetic field, hence the name diamagnetic shielding. The heat flux from the background plasma is guided by the magnetic field lines, so deflection of the magnetic field leads to a deflection of the heat flux around the ablation cloud. The importance of this effect can be characterized by the ratio of the flow speed of material away from the pellet and the speed of the diffusion of the magnetic field into the neutral cloud, which is not expected to be very large due to the comparatively low conductivity of the neutral cloud (Parks & Turnbull, 1978).

As the gas dynamic shielding is typically the dominating shielding mechanism, most models of pellet ablation are centered around a treatment of this mechanism, possibly including corrections for other shielding mechanisms. This allows for several simplifications of the problem, leading to the so-called *Neutral Gas Shielding (NGS) model* described in the next subsection.

4.2.1 The Neutral Gas Shielding model

We consider here a pellet surrounded by neutral ablated gas, which is heated primarily by energy deposited in the cloud by the light electrons of the bulk plasma, streaming rapidly along the field lines to intersect the pellet. As the time scale for the build-up of the shielding cloud is in the μs-range, which is about 2-3 orders of magnitude faster than most other processes of interest, the problem may be treated as quasi-stationary. In the original treatment of this problem by Parks & Turnbull (1978), the energy distribution of the incident electrons from the bulk plasma was approximated by a single mono-energetic beam, with effective energy per particle $\mathcal{E}_{\text{in}} = 2T$, equal to the ratio of the unidirectional heat and particle flux. Despite its simplicity, this model gives ablation rates which agree reasonably well with experiments (Pégourié, 2007). For this reason, the calculation of the pellet rocket force in paper **E** was built on this solution to the spherically symmetric problem, making it instructive to study here. Apart from differences in the calculation of the heat flux attenuation, the outline of the solution is also similar for more advanced models (Parks, Leffler & Fisher, 1988; MacAulay, 1994; Fontanilla & Breizman, 2019).

With the above considerations, the dynamics of the ablated gas is then governed by the steady-state conservation equations of mass, momentum and energy, as well as the equation of state for an ideal gas:

$$\nabla \cdot (\rho \vec{v}) = 0 \tag{4.2}$$

$$\rho \vec{v} \cdot \nabla \vec{v} = -\nabla p \tag{4.3}$$

$$\nabla \cdot \left[\left(\frac{\rho v^2}{2} + \frac{\gamma_{\text{a}} p}{\gamma_{\text{a}} - 1} \right) \vec{v} \right] = -f_{\text{heat}} \nabla \cdot \vec{\mathcal{Q}} = -f_{\text{heat}} \frac{d\mathcal{Q}}{dx} \tag{4.4}$$

$$p = \frac{\rho T}{m}, \tag{4.5}$$

where ρ is the mass density, $\vec{v}$ is the flow velocity, p is the pressure, m is the mass per ablated particle, $\mathcal{Q}$ is the heat flux of electrons from the background plasma flowing along the magnetic field lines in the x-direction, f_{heat} is the fraction of the absorbed heat flux that goes into heating the cloud ($f_{\text{heat}} \approx 0.65$ according to Parks & Turnbull (1978)), γ_{a} is the adiabatic index, and r is the radial coordinate (all coordinates are defined in figure 4.1).

For a mono-energetic beam of incoming electrons, the equations governing the attenuation of the heat flux and effective energy per particle take the form

$$\frac{d\mathcal{Q}}{dx} = -\frac{\rho}{m} \mathcal{Q} \Lambda(\mathcal{E}) \tag{4.6}$$

$$\frac{d\mathcal{E}}{dx} = -2 \frac{\rho}{m} L(\mathcal{E}). \tag{4.7}$$

In the treatment by Parks & Turnbull (1978), the effective heat flux cross section Λ and electron energy loss function L were approximated by semi-empirical expressions

according to

$$\Lambda(\mathcal{E}) = \hat{\sigma}_T(\mathcal{E}) + \frac{2L(\mathcal{E})}{\mathcal{E}} \tag{4.8}$$

$$L(\mathcal{E}) = 8.62 \cdot 10^{-15} \cdot \left[\left(\frac{\mathcal{E}}{100}\right)^{0.823} + \left(\frac{\mathcal{E}}{60}\right)^{-0.125} + \left(\frac{\mathcal{E}}{48}\right)^{-1.94} \right]^{-1} \text{eV} \cdot \text{cm}^2 \tag{4.9}$$

$$\hat{\sigma}_T(\mathcal{E} > 100\,\text{eV}) = \frac{8.8 \cdot 10^{-13}}{\mathcal{E}^{1.71}} - \frac{1.62 \cdot 10^{-12}}{\mathcal{E}^{1.932}}\,\text{cm}^2 \tag{4.10}$$

$$\hat{\sigma}_T(\mathcal{E} < 100\,\text{eV}) = \frac{1.1 \cdot 10^{-14}}{\mathcal{E}}\,\text{cm}^2, \tag{4.11}$$

where $\hat{\sigma}_T$ is the total elastic scattering cross section.

As the gas dynamic shielding mostly takes place close to the pellet surface, where the shielding cloud is essentially spherically symmetric, it is a reasonable approximation to reduce the problem to one, radial, dimension. This approximation is essential for the analytical tractability of the problem. One way to impose this reduced dimensionality on the incoming heat flux is to approximate all paths taken by the electrons through the cloud by the purely radial path that leads to the same point, corresponding to replacing $d\mathcal{Q}/dx$ with $-d\mathcal{Q}/dr$. Note that the attenuation of the heat flux, and thus the corresponding heat source, only depends on the length of the path taken through the cloud, i.e. it does not depend on the direction of the heat flux directly, so that this approximation only affects the results through an order unity modification to the heat source via a modification to the path length.

An alternative way to arrive at this approximation is to write $\nabla\mathcal{Q} = \partial\mathcal{Q}/\partial r + 2\mathcal{Q}/r$ for a spherically symmetric heat flux. The second term, corresponding to the convergence of the heat flux, is then dropped, as such a convergence does not occur in reality for electrons streaming along the non-converging field lines.

Inserting the above approximations reduces the equation system to

$$\frac{d}{dr}\left(r^2 v_0 \frac{p_0}{T_0}\right) = 0 \Rightarrow r^2 v_0 \frac{p_0}{T_0} = \text{const} = \frac{G}{4\pi} \tag{4.12}$$

$$m\frac{p_0}{T_0} v \frac{dv_0}{dr} + \frac{dp_0}{dr} = 0 \tag{4.13}$$

$$\frac{G}{4\pi r^2}\frac{d}{dr}\left(\frac{\gamma_\text{a} T_0}{\gamma_\text{a} - 1} + m\frac{v_0^2}{2}\right) = f_\text{heat}\frac{d\mathcal{Q}_0}{dr} \tag{4.14}$$

$$\frac{d\mathcal{Q}_0}{dr} = \frac{p_0}{T_0}\mathcal{Q}_0\Lambda(\mathcal{E}_0) \tag{4.15}$$

$$\frac{d\mathcal{E}_0}{dr} = 2\frac{p_0}{T_0}L(\mathcal{E}_0), \tag{4.16}$$

where G is the particle ablation rate [s^{-1}] and index 0 is used to distinguish the spherically symmetric component.

The pellets considered for the ITER disruption mitigation system, consisting of neon and hydrogen isotopes, have a sublimation energy per particle of only a fraction of an electron volt. For such pellets, the boundary condition at the pellet surface can be expressed by requiring the heat flux and cloud temperature to completely

vanish at the pellet surface. At large radii, the pressure can be considered negligible, and the heat flux and effective incoming electron energy must approach those of the background plasma. In summary, the boundary conditions are

$$p(r \to \infty) = 0, \quad \mathcal{Q}(r \to \infty) = \mathcal{Q}_{\text{in}}, \quad \mathcal{E}(r \to \infty) = \mathcal{E}_{\text{in}}, \tag{4.17}$$

$$\mathcal{Q}(r_p) = 0, \quad T(r_p) = 0, \tag{4.18}$$

where $\mathcal{Q}_{\text{in}}$ and $\mathcal{E}_{\text{in}}$ are the initial incoming heat flux and electron energy, and r_p is the pellet radius. The solution to the equation system thus obtained yields the NGS model (Parks & Turnbull, 1978).

A semi-analytical solution to this equation system can be obtained by normalizing the involved quantities to their values at the sonic radius (i.e. the radius where the flow becomes supersonic, marked by a subscript '*', see figure 4.1),

$$\begin{aligned} &\bar{p}_0 = p_0/p_*, \quad \bar{T}_0 = T_0/T_*, \quad \bar{v}_0 = v_0/v_*, \quad \bar{\mathcal{Q}}_0 = \mathcal{Q}_0/\mathcal{Q}_*, \quad \bar{\mathcal{E}}_0 = \mathcal{E}_0/\mathcal{E}_* \\ &\bar{r} = r/r_*, \quad \bar{\Lambda}(\bar{\mathcal{E}}_0) = \Lambda(\bar{\mathcal{E}}_0\mathcal{E}_*)/\Lambda(\mathcal{E}_*) \quad \bar{L}(\bar{\mathcal{E}}_0) = L(\bar{\mathcal{E}}_0\mathcal{E}_*)/[\mathcal{E}_*\Lambda(\mathcal{E}_*)], \end{aligned} \tag{4.19}$$

where we introduced the new variable $\bar{w}_0 = \bar{v}_0^2$. After some algebra, the equation system may be rearranged to (dropping the bar for brevity)

$$\frac{dw_0}{dr} = \frac{4w_0T_0}{(T_0 - w_0)r}\left(\frac{\mathcal{Q}_0\Lambda(\mathcal{E}_0)r}{T_0\sqrt{w_0}} - 1\right) \tag{4.20}$$

$$\frac{dT_0}{dr} = \frac{2\Lambda\mathcal{Q}_0}{\sqrt{w_0}} - \frac{1}{2}(\gamma_{\text{a}} - 1)\frac{dw_0}{dr} \tag{4.21}$$

$$\frac{d\mathcal{E}_0}{dr} = 2\lambda_*\frac{L(\mathcal{E}_0)}{r^2\sqrt{w_0}} \tag{4.22}$$

$$\frac{d\mathcal{Q}_0}{dr} = \lambda_*\frac{\mathcal{Q}_0\Lambda(\mathcal{E}_0)}{\sqrt{w_0}r^2}, \tag{4.23}$$

where

$$\lambda_* = r_*\Lambda_*p_*/T_* \tag{4.24}$$

is a dimensionless eigenvalue that uniquely determines the solution to the normalized equation system. This derivation uses the relation

$$v_* = \sqrt{\frac{\gamma_{\text{a}}T_*}{m}} \tag{4.25}$$

for the speed of sound at the sonic radius, and the condition that all quantities must be continuous across the sonic radius, which imposes a condition on the dimensional quantities there:

$$\frac{4\pi r_*}{G}\frac{(\gamma_{\text{a}} - 1)}{\gamma_{\text{a}}}\frac{\lambda_* f_{\text{heat}}\mathcal{Q}_*}{T_*} = 2. \tag{4.26}$$

The equation for dw/dr has an apparent singularity at the sonic radius, but dw/dr can still be determined by L'Hopital's rule, yielding

$$\left.\frac{dw}{dr}\right|_{r=1} = \frac{\frac{1}{2}(3 - \gamma_{\text{a}}) + \{[\frac{1}{2}(3 - \gamma_{\text{a}})]^2 - \frac{1}{2}(\gamma_{\text{a}} + 1)(\lambda_* + \psi_* - 1)\}^{1/2}}{(\gamma_{\text{a}} + 1)/4}, \tag{4.27}$$

where

$$\psi_* = \left.\frac{d\Lambda}{dr}\right|_{r=1} = \frac{2\lambda_* L}{\Lambda^2}\left.\frac{d\Lambda}{d\mathcal{E}_0}\right|_{\mathcal{E}_0=\mathcal{E}_*}. \tag{4.28}$$

It is then possible to start integrating the normalized equation system numerically from the sonic radius (where, with the present normalisation, all quantities of interest are equal to 1) towards smaller radii, for some assumed value of λ_*. The value of λ_* can then be varied until a value is found such that the boundary conditions for $\mathcal{Q}$ and T are simultaneously satisfied. The radius at which this happens is then interpreted as the normalized pellet radius (which is not known a-priori). When the appropriate value of λ_* is found, one can integrate from the sonic radius towards larger radii, and find what values of the normalized heat flux $\bar{\mathcal{Q}}_{\rm in}$ and effective beam energy $\bar{\mathcal{E}}_{\rm in}$ the solution corresponds to (these values are also not known a-priori). Finally, combining equations (4.12), (4.24), (4.25) and (4.26), the ablation rate can be expressed in terms of $\lambda_*(\mathcal{E}_*)$, $\bar{\mathcal{Q}}_{\rm in}(\mathcal{E}_*)$ and $\bar{\mathcal{E}}_{\rm in}(\mathcal{E}_*)$, which are found from the calculation outlined above to be essentially constant except for a very weak dependence on $\mathcal{E}_*$ (Parks & Turnbull, 1978), according to

$$G = 4\pi\lambda_* \left(\frac{\gamma_{\rm a}-1}{2\bar{r}_{\rm p}^4\bar{\mathcal{Q}}_{\rm in}}\right)^{1/3}\left[\frac{f_{\rm heat}\mathcal{Q}_{\rm in}r_{\rm p}^4}{\Lambda_*^2 m}\right]^{1/3}. \tag{4.29}$$

Following a similar methodology, this model has later been improved upon, and adapted to various situations. This includes e.g. using a more sophisticated model for the heat flux attenuation and treating the full Maxwellian energy distribution of the incident particles (MacAulay, 1994; Fontanilla & Breizman, 2019), treating pellets consisting of higher atomic number material (Parks, Leffler & Fisher, 1988; Fontanilla & Breizman, 2019), or including the shielding due to the still cold plasma expanding along the field lines outside the neutral cloud (Pegourie *et al.*, 2002). However, the mass ablation rate can typically be expressed as a scaling law according to

$$G = \lambda\zeta(B)\left(\frac{\mathcal{Q}_{\rm in}}{\mathcal{Q}_{\rm ch}}\right)^{1/3}\left(\frac{\mathcal{E}_{\rm in}}{\mathcal{E}_{\rm ch}}\right)^{7/6}\left(\frac{r_{p,k}}{r_{\rm ch}}\right)^{4/3}. \tag{4.30}$$

Here, $\mathcal{Q}_{\rm ch}$, $\mathcal{E}_{\rm ch}$ and $r_{\rm ch}$ are characteristic values of the incoming heat flux, effective energy and pellet radius, respectively, and the details of the energy attenuation model enter via the pre-factor λ *. The additional pre-factor $\zeta(B)$ may be used to account for the variation of the ablation rate with the magnetic field. This variation occurs partly due to the diamagnetic shielding, and partly due to the impact of the magnetic field on the geometry of the plasmoid of recently ionized material, affecting its contribution to the shielding (Bosviel, Parks & Samulyak, 2021; Samulyak *et al.*, 2021). The details of the version of the NGS model used in this thesis are given in section 5.1.

4.3 Deposition of the ablated material

Once the pellet material is ablated and ionized, it begins to homogenize over the flux surfaces, and the pressure and temperature start to equilibrate with the background

*The exponents are also slightly dependent on the energy attenuation model, but usually to a negligible extent (Fontanilla & Breizman, 2019; Parks, 2017; Parks & Turnbull, 1978).

plasma. In present day machines, the homogenization process takes place over a time scale of 0.1-1 ms Pégourié & Picchiottino (1996). There are two main processes responsible for the homogenization. The first is the excess pressure of the cold plasmoid of ablated material driving its expansion along the magnetic field, at a speed similar to the sound speed inside the plasmoid. As a field line covers a whole flux surface[†], the expansion along the field lines eventually leads to the material being homogenized over the entire flux surface. This mechanism alone has however been shown to give about an order of magnitude slower equilibration than the 0.1-1 ms time scale observed in experiments Pégourié & Picchiottino (1996).

An additional mechanism to consider in describing the homogenization is caused by the potential difference between the channel of ablated material and the background plasma, again arising due to the much larger mobility of electrons compared to ions. As the channel of ablated material is heated while still having a much larger density than the background plasma, the net flow of negative charge will go from the channel of ablated material into the background plasma. The gradient along the tokamak minor radius of this potential gives rise to an electric field along the minor radius, which in turn causes an $E \times B$-drift in the poloidal direction. Conservation of momentum on the flux surface where the channel of ablated material resides then gives rise to a poloidal rotation of the plasma in the direction opposite to the poloidal $E \times B$-drift of the ablated material. The gradient of this rotation along the minor radius, together with the variation of the background magnetic field direction, gives rise to a poloidal stretching of the ablated material. As the ablated material is thinned out, the collisional interaction with the background plasma and the small scale turbulence becomes more effective, and eventually the ablated material equilibrates with the background plasma. The above mechanisms together have been shown to give rather accurate reproductions of the time evolution of the background plasma following fueling pellet injections in experiments Pégourié & Picchiottino (1996).

Finally, yet another $E \times B$-related drift might be present that transports the ablated material across the flux surfaces Parks & Baylor (2005). The limited length along the toroidal field line of the initial expanding channel of ionised, ablated material, re-introduces the issue of vertical charge separation in the channel by the ∇B drift. Remember this issue was described in chapter 1, occurring in the whole tokamak in the absence of a poloidal magnetic field. This gives rise to a vertical electric field in the vicinity of the ablated material, causing an $E \times B$ drift of the ablated material along the major radius towards the low magnetic field side. This cross-field drift results in a shift of the final deposition profile compared to the deposition profile immediately following the ablation. There is a wealth of experimental observations of this effect in present-day tokamaks (Baylor *et al.*, 2007; Lang *et al.*, 1997), and numerical simulations indicate that it might have a substantial impact in ITER (Matsuyama, 2022). This phenomenon is also the subject of paper **C**, and is described further in the next subsection.

[†]This is technically not true for the countable number of rational flux surfaces where the number of poloidal to toroidal turns of the field line is a ratio of integers. However, due to the finite gyroradius and the cross-field drift described below in section 4.3.1, the particles are not strictly confined to a single flux surface, which effectively reduces the effect of the rational flux surfaces.

4.3.1 Cross-field drift

The size of the outward shift of ablated pellet material resulting from the cross-field drift is regulated by three main mechanisms, related to the decay of the excess pressure inside the plasmoid, the twisting of the magnetic field lines, and additional currents counter-acting the charge separation (Pégourié *et al.*, 2006; Rozhansky *et al.*, 2004; Parks, Sessions & Baylor, 2000; Samulyak *et al.*, 2021). The excess current due to the ∇B drift inside the plasmoid compared to the background plasma is proportional to the excess pressure inside the plasmoid. Thus, as the plasmoid expands and the excess pressure decreases, so does the driving force behind the drift motion. Moreover, as the plasmoid expands around the torus along the twisted magnetic field lines, the vertical position of the field lines is inverted for the inboard portion of the plasmoid compared to the outboard portion, and when this happens the magnetic drift currents in the outboard and inboard portions of the plasmoid cancel out (analogously to a tokamak equilibrium). This mechanism effectively stops the drift motion over a characteristic time scale given by the time it takes for the cloud to expand one connection length along the field lines, $t_{\mathrm{drift}} \sim \pi R_{\mathrm{m}} q / c_{\mathrm{s}}$, where R_{m} is the major radius, c_{s} is the sound speed inside the plasmoid and q is the safety factor. Finally, the electric field resulting from the charge separation gives rise to additional currents counter-acting the charge separation, which limit the build-up of the electric field and hence the $E \times B$ drift.

The $E \times B$ drift velocity, given by (Chen, 1974),

$$\mathbf{v}_{\mathrm{d}} = \frac{\mathbf{E} \times \mathbf{B}}{B^2} \approx \frac{E_y}{B} \hat{R}, \tag{4.31}$$

is proportional to the binormal (nearly vertical) electric field $\mathbf{E} \approx E_y \hat{y}$ inside the plasmoid (considering $t \ll t_{\mathrm{drift}}$, i.e. disregarding the twisting of the field lines, for simplicity, referring to paper **C** for a more detailed picture). Moreover, the vertical electric field, as well as the density and temperature, may be approximated as constant along the field lines inside the plasmoid Pégourié *et al.* (2006). The equation of motion of the cloud can thus be formulated as a condition for the current density $\mathbf{j}$ to be divergence free in the quasi-neutral plasma. Such a formulation is useful when deriving a model of reduced dimensionality; the divergence of the current can be integrated over some volume to obtain an equation describing the balance of the total currents going into and out of the volume of integration, as illustrated in figure 4.2. This procedure effectively averages the equation of motion over the integration volume.

The equation of motion of the ablated material is governed by the quasi-static MHD force balance equation,

$$\rho \frac{d\mathbf{v}_{\mathrm{d}}}{dt} = \mathbf{j} \times \mathbf{B} + \nabla p, \tag{4.32}$$

from which the divergence of the current density can be obtained as

$$\nabla \cdot \mathbf{j} = \nabla \cdot \left(\frac{\mathbf{B} \times \nabla p}{B^2} + \frac{\rho}{B} \hat{x} \times \frac{d\mathbf{v}_{\mathrm{d}}}{dt} + j_{||} \hat{x} \right) = 0. \tag{4.33}$$

Here, ρ is the mass density and p is the plasmoid pressure. The first term can be simplified for large aspect ratios, utilizing that the curvature vector $\boldsymbol{\kappa} = \nabla B/B \approx \hat{R}/R_{\mathrm{m}}$, according to

$$\nabla \cdot \left(\frac{B \times \nabla p}{B^2} \right) = \nabla \cdot \left[p \nabla \times \left(\frac{\mathbf{B}}{B^2} \right) \right] \approx \nabla \cdot \left(2p \frac{\mathbf{b} \times \nabla B}{B^2} \right) \approx \nabla \cdot \left(-\frac{2p}{BR_{\mathrm{m}}} \hat{y} \right). \quad (4.34)$$

Inserting this into equation (4.33), along with equation (4.31) for the drift velocity, we obtain

$$\nabla \cdot \mathbf{j} = \nabla \cdot \left(-\frac{2p}{BR_{\mathrm{m}}} \hat{y} + \frac{\rho}{B^2} \frac{dE_y}{dt} \hat{y} + j_{||} \hat{x} \right) = 0. \quad (4.35)$$

We now reduce the dimensionality of the problem by integrating equation (4.35) over a suitable volume V. This volume is taken to be a flux tube along the field lines covering the upper half of the cloud, corresponding to the blue area in figure 4.2 (which is essentially symmetric to the lower half) with a small thickness δR along the major radius (into the plane of the paper). Applying the divergence theorem, this gives a current balance equation according to

$$\int_{\partial V} \left(-\frac{2p}{BR_{\mathrm{m}}} \hat{y} + \frac{\rho}{B^2} \frac{dE_y}{dt} \hat{y} + j_{||} \hat{x} \right) \cdot \hat{n} dS = I_{\nabla B} + I_{\dot{E}} + I_{||} = 0, \quad (4.36)$$

where $\hat{n}$ is the surface normal at the surface element dS running over the volume boundary ∂V.

The integral of the first term corresponds to the ∇B-current $I_{\nabla B}$. For $t \ll t_{\mathrm{drift}}$, the total ∇B current, per unit length in the radial direction, is approximately given by (Rozhansky *et al.*, 2004)

$$J_{\nabla B} = \frac{I_{\nabla B}}{\delta R} =\approx -\frac{2 \Delta p L_{\mathrm{cld}}}{BR_{\mathrm{m}}}, \quad (4.37)$$

where Δp is the excess pressure and L_{cld} is the length of the plasmoid. The second term is related to the time variation of the electric field; the time variation of the electric field causes an acceleration of the $E \times B$ drift, which the drifting particles experience as a force. In a similar way as the force from the electric field gives rise to the $E \times B$ drift, the force corresponding to this acceleration of the $E \times B$ drift gives rise to an additional drift, called the *polarisation drift*. This drift is perpendicular to both the magnetic field and the $E \times B$ drift, and is therefore directed in the vertical direction in this case, as shown in figure 4.2. The corresponding current, per unit length in the radial direction, is given by Pégourié *et al.* (2006)

$$J_{\dot{E}} = \frac{I_{\dot{E}}}{\delta R} = \frac{\bar{\rho}}{B^2} \frac{dE_y}{dt}, \quad (4.38)$$

where $\bar{\rho}$ is the field line-integrated mass density inside the plasmoid.

The remaining contribution comes from currents exiting the plasmoid parallel to the field lines. There are two components of these currents, one of which is carried by the Alfvén waves traveling along the field lines, excited by the gradient in the electrostatic potential imposed by the charge separation inside the plasmoid.

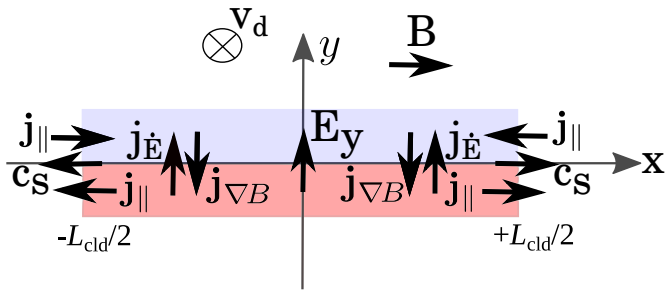

Figure 4.2: Toroidal cross section of a plasmoid of ablated pellet material, showing the contributions to the current balance determining the vertical electric field E_y and the corresponding drift velocity (in the radial direction). The positively (lower) and negatively (upper) charged parts of the plasmoid are marked with red and blue, respectively. The plasmoid expands in the x-direction, parallel to the magnetic field, at the speed of sound c_s, and the drift motion is directed into the paper.

Initially, before any of the Alfvén waves emitted from the opposite sides of the cloud have started to interfere with each other, this current contribution can be described by the Alfvén resistivity $R_\mathrm{A} = \mu_0 c_\mathrm{A}$, where μ_0 is the vacuum permeability and $c_\mathrm{A} = B/\sqrt{\mu_0 \rho} \gg c_\mathrm{s}$ is the Alfvén speed (Rozhansky *et al.*, 2004). The resulting parallel current, per unit length in the radial direction, becomes

$$J_\mathrm{A} = 2\frac{E_y}{R_\mathrm{A}}. \tag{4.39}$$

The factor 2 comes from the fact that the current flows from both sides of the plasmoid.

When the Alfvén waves traveling along a set of field lines meet the Alfvén waves traveling from the opposite side of the plasmoid, these waves interfere so that the electrostatic potential starts to converge towards a quasi-steady, nearly linear, variation along these field lines. At this point, these field lines effectively form a coil along which the current can be described by Ohm's law. Every time the Alfvén waves travel one toroidal turn around the torus, a portion of the field lines (statistically) will "connect" in this way to the opposite side of the plasmoid, so that an increasing fraction of the field lines start to carry an ohmic current instead of an Alfvénic current. The total parallel current contribution thus takes the form (Pégourié *et al.*, 2006)

$$J_{||} = \frac{I_{||}}{\delta R} = J_\mathrm{Ohm} + J_\mathrm{A} = \frac{E_y}{R_\mathrm{eff}} + 2P_\mathrm{A}\frac{E_y}{R_\mathrm{A}}, \tag{4.40}$$

where P_A is the fraction of the field lines still carrying an Alfvénic current, and R_eff is the effective resistance of the Ohmic current, determined by the background plasma conductivity and the length of every set of field lines connecting to the opposite side of the plasmoid.

The total current balance equation thus takes the form of a first-order ODE for E_y, and hence the drift velocity via equation (4.31), according to

$$J_{\nabla B} + J_{\dot{E}} + J_\mathrm{A} + J_\mathrm{Ohm} = -\frac{2\Delta p L_\mathrm{cld}}{B R_\mathrm{m}} + \frac{\bar{\rho}}{B^2}\frac{dE_y}{dt} + \frac{E_y}{R_\mathrm{eff}} + 2P_\mathrm{A}\frac{E_y}{R_\mathrm{A}} = 0. \tag{4.41}$$

This model was originally studied by Pégourié *et al.* (2006) and Commaux *et al.* (2010*b*) to examine the parameter dependence of the plasmoid drift and validate the model by comparing the resulting density build-up against experiments. They used a numerical model for the plasmoid density, temperature and size, as well as the effective resistance for the Ohmic current, and accounting for the poloidal twist of the field lines by limiting the integration time to t_{drift}. A more detailed derivation of the equation of motion for the plasmoid drift, along with an analytical solution, is presented in paper **C**, including an improved treatment of the poloidal twist of the magnetic field lines and an analytical model for R_{eff}.

4.4 Pellet acceleration due to asymmetric heating

As mentioned in the beginning of the chapter, the pellet ablation may be asymmetric, giving rise to a rocket-like acceleration of the pellet (Jones, 1978; Andersen, 1985; Müller *et al.*, 2002). Of particular interest for disruption mitigation is the radial rocket effect related to the heating asymmetries caused by plasma gradients and non-uniform plasma shielding due to the plasmoid drift[‡] (Senichenkov, Rozhansky & Gusakov, 2007), illustrated in figure 4.1. This effect has been found to be substantial in disruption mitigation SPI experiments at JET (Jachmich *et al.*, 2022; Kong *et al.*, 2024), indicating that it may have a significant effect on the core penetration of pellets injected into reactor-scale devices.

Depending on the pellet composition, the rocket acceleration can be explained either by the asymmetry in the ablation flow (Senichenkov, Rozhansky & Gusakov, 2007) or in the pressure inside the ablation cloud (Szepesi *et al.*, 2009). In the case of cryogenic pellets, it is found in papers **E** and **F** that the latter dominates. A first self-consistent analytical derivation of the rocket force on a cryogenic pellet due to plasma gradients is presented in paper **E**, based on the heat flux attenuation model described in section 4.2.1 and the considerations detailed below. Further details about the model and its predictions are given in paper **F**, where it is also extended to account for the asymmetry related to the plasmoid drift.

Consider a pellet heated by an asymmetric heat source, giving rise to an asymmetry also in the other pellet cloud parameters, which may be expressed in the form

$$X = X_0(r) + \delta X(r, \theta, \phi), \tag{4.42}$$

where $X = \{p, \mathbf{v}, T, \mathcal{Q}, \mathcal{E}\}$ and $\mathbf{v} = v_r\hat{r} + v_\theta\hat{\theta} + v_\phi\hat{\phi}$. Here, θ and ϕ are the polar and azimuthal angle, respectively, of a spherical coordinate system with the z-axis aligned with the axis of asymmetry (recall from figure 4.1). As will be clear shortly, it is convenient to expand the angularly dependent parts according to

$$\delta X = \sum_{m=0}^{\infty}\sum_{l=1}^{\infty} X_l^m(r) Y_l^m(\theta, \phi) \tag{4.43}$$

[‡]Note that even in cases where the plasma shielding has a negligible effect on the ablation rate, the non-uniformity of the plasma shielding may still contribute significantly to the ablation cloud asymmetry.

for all quantities except for δv_θ, which we expand as

$$\delta v_\theta = \sum_{m=0}^{\infty} \sum_{l=1}^{\infty} v_{\theta,l}^m(r) \frac{dY_l^m(\theta,\phi)}{d\theta}, \tag{4.44}$$

where

$$Y_l^m(\theta,\varphi) = \sqrt{\frac{(l-m)!}{(l+m)!}} \mathcal{P}_l^m(\cos\theta) e^{im\varphi}\,, \tag{4.45}$$

are the spherical harmonics, with $\mathcal{P}_l^m$ being the associated Legendre polynomials.

The net force on the pellet may be found by integrating the stress tensor across the pellet surface S:

$$\vec{F} = -\iint_S (\rho \mathbf{vv}\cdot\hat{r} + p\hat{r})\, dS. \tag{4.46}$$

Inserting the spherical coordinates, utilizing that they are defined such that the force points in the negative z-axis, yields

$$F = -\hat{z}\cdot\mathbf{F} = r_\mathrm{p}^2 \iint_S [\rho v_r(v_r\cos\theta + v_\theta \sin\theta) + p\cos\theta]\, d\Omega, \tag{4.47}$$

with the differential solid angle $d\Omega = \sin\theta d\theta d\phi$. Considering a small asymmetry, such that (4.47) may be linearised around the spherically symmetric cloud parameters, the expression for the force can be rewritten further as

$$\begin{aligned} F &= r_\mathrm{p}^2 \iint_S \left[\left(\delta\rho\, v_0^2 + 2\rho_0 v_0\, \delta v_r + \delta p\right)\cos\theta + \rho_0 v_0\, \delta v_\theta \sin\theta\right]\, d\Omega \\ &= r_\mathrm{p}^2 \iint_S \left[\delta\rho\, v_0^2 + 2\rho_0 v_0 \left(\delta v_r - \int_0^\theta \delta v_\theta\,(\theta')\,\mathrm{d}\theta'\right) + \delta p\right] Y_1^0 d\Omega, \end{aligned} \tag{4.48}$$

where in the last step a partial integration was used on the second term and we recognized that $\cos\theta = Y_1^0$. Utilizing that the spherical harmonics are orthogonal in the sense

$$\iint_S Y_l^m (Y_{l'}^{m'})^* d\Omega = \frac{4\pi}{2l+1}\delta_{ll'}\delta_{mm'}, \tag{4.49}$$

it is clear that only the $l = 1$, $m = 0$ component contributes to the force, which therefore simplifies to (dropping the m-index as $m = 0$ for all relevant terms)

$$F = \frac{4\pi r_\mathrm{p}^2}{3}\left(\rho_1 v_0^2 + 2\rho_0 v_0 (v_{1,r} - v_{1,\theta}) + p_1\right)_{r=r_\mathrm{p}}. \tag{4.50}$$

The problem of finding the rocket force is thus reduced to relating the asymmetries in the cloud parameters to the asymmetry in the incoming heat flux, projected onto the $l = 1$, $m = 0$ harmonic. Linearising the gas dynamic equations (4.2)-(4.7) around the spherically symmetric solution, and again utilizing the orthogonality of the spherical harmonics, yields an independent ordinary differential equation system with respect to r for each l and m. A semi-analytical solution may be found by normalizing the spherically symmetric solution to its values at the sonic radius (as in section 4.2.1) and normalizing the first order asymmetry correction according to

$$\begin{aligned} &\bar{p_1} = p_1/(p_*\mathcal{Q}_\mathrm{rel}), \quad \bar{T_1} = T_1/(T_*\mathcal{Q}_\mathrm{rel}), \quad \bar{v_{1,r}} = v_{1,r}/(v_*\mathcal{Q}_\mathrm{rel}), \\ &\bar{v_{1,\theta}} = v_{1,\theta}/(v_*\mathcal{Q}_\mathrm{rel}), \quad \bar{\mathcal{Q}_1} = \mathcal{Q}_1/(\mathcal{Q}_*\mathcal{Q}_\mathrm{rel}), \quad \bar{\mathcal{E}_1} = \mathcal{E}_1/(\mathcal{E}_*\mathcal{Q}_\mathrm{rel}), \end{aligned} \tag{4.51}$$

where

$$\mathcal{Q}_{\mathrm{rel}} = \frac{1}{\mathcal{Q}_{\mathrm{in}}} \frac{\int_0^{2\pi}\int_0^{\pi} \delta\mathcal{Q}(r=\infty) Y_1^0 \sin\theta d\theta d\phi}{\int_0^{2\pi}\int_0^{\pi} (Y_1^0)^2 \sin\theta d\theta d\phi} \tag{4.52}$$

is the relative heat flux asymmetry far away from the pellet, projected onto the $l = 1$, $m = 0$ spherical harmonic. Note that there is no (linear) contribution from v_ϕ as this harmonic is symmetric in ϕ. The equation system thus obtained for the $l = 1$, $m = 0$ harmonic can be written as (dropping the bar for brevity)

$$\frac{\partial}{\partial r}\left(\frac{p_0}{T_0}\right) v_{1,r} + \frac{p_0}{T_0}\frac{1}{r^2}\frac{\partial}{\partial r}\left(r^2 v_{1,r}\right) + v_0 \frac{\partial}{\partial r}\left(\frac{p_1}{T_0} - \frac{p_0}{T_0^2}T_1\right) + \frac{1}{r^2}\frac{\partial}{\partial r}\left(r^2 v_0\right)\left(\frac{p_1}{T_0} - \frac{p_0}{T_0^2}T_1\right) - 2\frac{p_0}{rT_0}v_{1,\theta} = 0 \tag{4.53}$$

$$\frac{p_0}{T_0}v_{1,r}v_0' + \frac{p_0}{T_0}v_0 v_{1,r}' + \left(\frac{p_1}{T_0} - \frac{p_0}{T_0^2}T_1\right)v_0 v_0' + \frac{p_1'}{\gamma_{\mathrm{a}}} = 0 \tag{4.54}$$

$$\frac{p_0}{T_0}\frac{v_0}{r}v_{1,\theta} + \frac{p_0}{T_0}v_0 v_{1,\theta}' + \frac{p_1}{\gamma_{\mathrm{a}} r} = 0 \tag{4.55}$$

$$\left(\frac{p_0 v_0^2}{2T_0} + \frac{p_0}{\gamma_{\mathrm{a}}-1}\right)\left[\frac{1}{r^2}\frac{\partial}{\partial r}\left(r^2 v_{1,r}\right) - 2\frac{v_{1,\theta}}{r}\right] + v_{1,r}\frac{\partial}{\partial r}\left(\frac{p_0 v_0^2}{2T_0} + \frac{p_0}{\gamma_{\mathrm{a}}-1}\right) + \left[\left(\frac{p_1}{T_0} - \frac{p_0}{T_0^2}T_1\right)\frac{v_0^2}{2} + \frac{p_0}{T_0}v_0 v_{1,r} + \frac{p_1}{\gamma_{\mathrm{a}}-1}\right]\frac{1}{r^2}\frac{\partial}{\partial r}\left(r^2 v_0\right) + v_0\frac{\partial}{\partial r}\left[\left(\frac{p_1}{T_0} - \frac{p_0}{T_0^2}T_1\right)\frac{v_0^2}{2} + \frac{p_0}{T_0}v_0 v_{1,r} + \frac{p_1}{\gamma_{\mathrm{a}}-1}\right] = \frac{2}{(\gamma_{\mathrm{a}}-1)\lambda_*}\frac{\partial \mathcal{Q}_1}{\partial r} \tag{4.56}$$

$$\frac{\partial \mathcal{Q}_1}{\partial r} = \lambda_*\left[\left(\frac{p_1}{T_0} - \frac{p_0}{T_0^2}T_1\right)\mathcal{Q}_0\Lambda(\mathcal{E}_0) + \frac{p_0}{T_0}\mathcal{Q}_0\frac{d\Lambda}{d\mathcal{E}}\Big|_{\mathcal{E}=\mathcal{E}_0}\mathcal{E}_1 + \frac{p_0}{T_0}\Lambda(\mathcal{E}_0)\mathcal{Q}_1\right] \tag{4.57}$$

$$\frac{\partial \mathcal{E}_1}{\partial r} = 2\lambda_*\left[\left(\frac{p_1}{T_0} - \frac{p_0}{T_0^2}T_1\right)L(\mathcal{E}_0) + 2\frac{p_0}{T_0}\frac{dL}{d\mathcal{E}}\Big|_{\mathcal{E}=\mathcal{E}_0}\mathcal{E}_1\right], \tag{4.58}$$

with a prime denoting derivative with respect to r, and the boundary conditions become

$$\begin{aligned} &T_1(r_p) = 0, \quad \mathcal{Q}_1(r_p) = 0, \\ &p_1(\infty) = 0, \quad \mathcal{Q}_1(\infty) = \mathcal{Q}_0(\infty), \quad \mathcal{E}_1(\infty) = \mathcal{E}_0(\infty)\mathcal{E}_{\mathrm{rel}}/\mathcal{Q}_{\mathrm{rel}}. \end{aligned} \tag{4.59}$$

Importantly, this equation system depends only on $\mathcal{E}_*$, which determines the spherically symmetric component as detailed in section 4.2.1, and $\mathcal{E}_{\mathrm{rel}}/\mathcal{Q}_{\mathrm{rel}}$ entering into the boundary condition for the first order asymmetry correction.

Finally, using equation (4.25) and (4.5), the rocket force on the pellet (4.50) may be expressed in terms of the normalized cloud parameters as

$$\begin{aligned} F &= \frac{4\pi r_p^2}{3} p_* \mathcal{Q}_{\mathrm{rel}}\left[\gamma_{\mathrm{a}} v_0^2\left(\frac{p_1}{T_0} - \frac{p_0}{T_0^2}T_1\right) + P_1(r_p) + \frac{2\gamma_{\mathrm{a}}}{r^2}(v_{1,r} - v_{1,\theta})\right]\Big|_{r\to r_p} \\ &= \frac{4\pi r_p^2}{3} p_* \mathcal{Q}_{\mathrm{rel}} f(\mathcal{E}_*, \mathcal{E}_{\mathrm{rel}}/\mathcal{Q}_{\mathrm{rel}}), \end{aligned} \tag{4.60}$$

where $f(\mathcal{E}_*, \mathcal{E}_{\rm rel}/\mathcal{Q}_{\rm rel})$ is a dimensionless factor which only depends on E_* and $E_{\rm rel}/\mathcal{Q}_{\rm rel}$. The pressure p_* at the sonic radius is determined by equations (4.12), (4.24), (4.25) and (4.26) in a similar way as the ablation rate (equation (4.29)):

$$p_* = \frac{\lambda_*}{\gamma_{\rm a}} \left(\frac{\bar{r}(\gamma_{\rm a}-1)^2}{4\bar{\mathcal{Q}}_{\rm in}} \right)^{1/3} \left[\frac{m(f_{\rm heat}\mathcal{Q}_{\rm in})^2}{\Lambda_* r_{\rm p}} \right]^{1/3}. \tag{4.61}$$

A solution of equations (4.53)-(4.58) and an analytical fit for $f(\mathcal{E}_*, \mathcal{E}_{\rm rel}/\mathcal{Q}_{\rm rel})$ is presented in paper **E**, with additional details provided in paper **F**.

Chapter 5

Disruption model

Having acquired a basic knowledge of the characteristic features of disruptions, and the proposed injection schemes to mitigate their impact, we are now in a position to describe the models used in this work to simulate such scenarios in papers **A**, **B**, **D**, **G** and **H**. A number of components are required to build a model for the injected material deposition through the final current decay, and they are described in the sections of this chapter. The model for the evolution of the electron and ion density, possibly including a source due to an ablating pellet, is described in section 5.1, and the model describing the subsequent plasma cooling is described in section 5.2. The cooling of the plasma is accompanied by a drop in the conductivity, leading to the induction of a strong electric field, after which the plasma current starts to decay. The strong electric field might however lead to the generation of a substantial runaway current, as was also described in section 1.2, resulting in an incomplete current decay. The evolution of the electric field, as well as the models governing the runaway generation resulting from the induced electric field, are described in section 5.3. Finally, the numerical tools GO (Fehér *et al.* (2011), Paper **A**), and DREAM (Hoppe, Embreus & Fülöp, 2021) are described in section 5.5. These codes solve the set of equations listed in this chapter starting from a set of given injection parameters and pre-disruption plasma parameters.

5.1 Material injection and density evolution

The density evolution is determined by summing the contributions from the ionization/recombination processes, the material injection and transport. As mentioned in section 4.3, the drift and homogenization of the ablated material over the flux surfaces, as well as the temperature and pressure equilibration with the background plasma, occurs over a time scale $\lesssim 1$ ms. This time scale is comparable to the thermal quench time scale, while being relatively fast compared to the current quench time scale. The homogenization and equilibration of the ablated material is therefore approximated here to take place instantaneously, an assumption also made in other recent disruption mitigation studies (Nardon *et al.*, 2020*b*; Matsuyama *et al.*, 2020; Nardon, Matsuyama & Lehnen, 2020; Shiraki *et al.*, 2020).

We utilise the near homogeneity of the plasma quantities over the flux surfaces to make the problem 1-dimensional, representing spatially varying quantities by their

flux surface averages. The flux surface geometry is described by the spatial Jacobian,

$$\mathcal{J} = \frac{1}{|\nabla\phi \cdot (\nabla\theta \times \nabla r)|}, \tag{5.1}$$

where ϕ is the toroidal angle, θ is the poloidal angle and r is a flux surface label, taken here to be the distance between the magnetic axis and the flux surface along the outboard mid-plane. The flux surface average of a quantity Y is then defined as

$$\langle Y \rangle = \frac{1}{V'} \int_0^{2\pi} \int_{-\pi}^{\pi} Y \mathcal{J} d\theta d\phi, \tag{5.2}$$

where

$$V' = \int_0^{2\pi} \int_{-\pi}^{\pi} \mathcal{J} d\theta d\phi. \tag{5.3}$$

In reality, the shape and size of the flux surfaces vary in time, consistently with the evolution of the plasma current and the corresponding poloidal magnetic flux. Here we however assume that the geometry of the flux surfaces used for the averaging described above is constant in time. Note, however, that only the flux surface geometry is held fix, and that we still calculate a value of the poloidal flux ψ_p which evolves with the plasma current as described in section 5.3. Losses of runaway electrons due to flux surfaces being scraped off against the wall are also accounted for, by introducing a loss term outside an estimated value of the actual minor radius of the last closed flux surface, as detailed in section 5.4.

With n_{ij} denoting the density of charge state i of ion species j, the change in the local charge state distribution of all ions may be modeled as

$$\frac{\partial n_{ij}}{\partial t} = \left(\frac{\partial n_{ij}}{\partial t}\right)_\mathrm{ioniz} + \left(\frac{\partial n_{ij}}{\partial t}\right)_\mathrm{injection} + \frac{1}{V'}\frac{\partial}{\partial r}\left[V'\left(-A_{ij}n_{ij} + D_{ij}\frac{\partial n_{ij}}{\partial r}\right)\right], \tag{5.4}$$

where the first term accounts for ionization and recombination processes, the second term accounts for the injection source and the last term describes an advective-diffusive transport. The corresponding evolution of the total free electron density n_free (including both the Maxwellian and non-Maxwellian populations) is determined by the condition that the plasma must remain quasi-neutral. In this work, the ion transport coefficients are prescribed by the user, typically in a way which resembles the transport found in 3D MHD simulations or experiments (Linder *et al.*, 2020; Hu *et al.*, 2021). Reasonable values vary from $A_{ij} \sim 100 - 1000\,\mathrm{m/s}$ and $D_{ij} \sim 100 - 1000\,\mathrm{m^2/s}$, depending on the scenario and tokamak device (see papers **D** and **H**).

The contribution from ionization and recombination is calculated by the time dependent rate equations

$$\left(\frac{\partial n_{ij}}{\partial t}\right)_\mathrm{ioniz} = I_{i-1,j}n_{i-1,j}n_\mathrm{M} - I_{ij}n_{ij}n_\mathrm{M} + R_{i+1,j}n_{i+1,j}n_\mathrm{M} - R_{ij}n_{ij}n_\mathrm{M}, \tag{5.5}$$

where $I_{ij}(T_\mathrm{M}, n_\mathrm{M})$ and $R_{ij}(T_\mathrm{M}, n_\mathrm{M})$ are the ionization and recombination rates, with n_M and T_M denoting the density and temperature of the thermal, Maxwellian, electron bulk, respectively (recall the division of the electron distribution function discussed in section 2.2.1). In this work, these ionization/recombination rates are

interpolated from tabulated values of numerical calculations of the excitation/deexcitation processes involved, available in the ADAS (Summers, 2004) and AMJUEL* databases.

The injection can be modeled in a number of different ways depending on the injection technique, with varying degree of sophistication. The simplest way to model an arbitrary type of injection is to assume the injected material to be instantly deposited in the neutral charge state at $t = 0$, with a prescribed spatial profile. This profile may be chosen to be rather homogeneous, motivated by the rapid flattening of the density profile due to the enhanced transport occurring when the magnetic field becomes stochastic. As the injection time scale is similar to the thermal quench time scale, and 1-2 orders of magnitude shorter than the current quench time scale, this model may be sufficient to capture the main characteristics of the disruption, especially the current evolution, and has therefore been used in several studies available in the literature (Izzo *et al.* (2011); Martín-Solís, Loarte & Lehnen (2017); Pusztai *et al.* (2023), Paper **A**, Paper **T**).

This model is however not sufficient to capture the detailed evolution of all quantities of interest, and does not treat the question of how the injected material is assimilated. In case of a pellet injection or SPI, this would instead require resolving the ablation and propagation of the pellet or pellet shards. The homogenized ion density increase on the flux surface with radius r due to the ablation of the pellet material is then given by

$$\left(\frac{\partial n_{ij}}{\partial t}\right)_{\text{injection}} = -f_{ij} \sum_{k=1}^{N_\text{s}} \frac{4\pi r_{p,k}^2 \dot{r}_{p,k} \rho_\text{dens} N_\text{A}}{\mathcal{M}} H(r, \rho_{p,k}), \tag{5.6}$$

where the time derivative $\dot{r}_{p,k}$ of the k^{th} shard is related to the mass ablation rate G_k of the same shard according to $\dot{r}_{p,k} = G_k/(4\pi r_{p,k}^2 \rho_\text{dens})$, where ρ_dens denotes the mass density of the solid pellet material. The factor f_{ij} denotes the particle fraction of the ablated material that is deposited to n_{ij}. The pellet molar mass is denoted by $\mathcal{M}$, and N_A is the Avogadro number. The radial distribution of the homogenized density increase is described by the factor $H(r, \rho_{p,k}) = h(r, \rho_{p,k})/V'$, where $h(r, \rho_{p,k})\mathrm{d}r$ describes the fraction of the material deposited at a radius between r and $r + \mathrm{d}r$ ablated from a pellet at radius $\rho_{p,k}$.

The initial shard sizes are drawn from the distribution given by equation (4.1). As a first approximation, the pellet shards may be assumed to travel along straight lines starting from a point close to the tokamak wall, following specified angular and speed distributions. Note however, that in reality, the pellet will be accelerated due to asymmetries in the ablation cloud caused by the asymmetric heating, as discussed in chapter 4.4. In the future, this effect may be accounted for using e.g. the model derived in paper **E**.

The ITER disruption mitigation system will use pellets consisting of a mixture of neon and hydrogen isotopes, thus requiring an NGS model adapted to such pellets. The most up to date version of the NGS model adapted to this situation, accounting for the full Maxwellian electron momentum distribution was presented by Parks (2017) (some additional details are also given by Samulyak *et al.* (2021)). According

*http://www.eirene.de

to this model, the ablation rate G_k takes the form of equation (4.30), with the prefactor λ given by

$$\lambda(X) = 2.99 \cdot 10^{23} \cdot [27.0837 + \tan(1.48709X)] \text{ s}^{-1}, \tag{5.7}$$

where $X = N_{\text{D}_2}/(N_{\text{D}_2} + N_{\text{Ne}})$ is the deuterium fraction, N_{D_2} is the number of deuterium molecules and N_{Ne} is the number of neon atoms in the pellet. The normalising radius, heat flux and effective energy in equation (4.30) are here given by $r_{\text{ch}} = 2$ mm, $\mathcal{Q}_{\text{ch}} = n_{\text{ch}}\sqrt{2T_{\text{ch}}^3/(\pi m_e)}$ and $\mathcal{E}_{\text{ch}} = 2T_{\text{ch}}$, with the representative temperature and density $T_{\text{ch}} = 2000$ eV and $n_{\text{ch}} = 10^{20}$ m^{-3}, respectively. This model has been used in many recent studies of disruption mitigation by SPI in ITER (Nardon *et al.*, 2020*b*; Hu *et al.*, 2018; Matsuyama *et al.*, 2020), including papers **B**, **D**, **G** and **H**.

The ablation rate also has a dependence on the magnetic field, due to the diamagnetic shielding and the impact of the magnetic field on the geometry of the plasmoid, as discussed in chapter 4.2.1. This dependence is accounted for by the factor ζ in equation (4.30). In paper **B** we use $\zeta = 1$, for simplicity, while in papers **D**, **G** and **H** we use an expression fitted to simulations with the FronTier code (Zhang & Parks, 2020; Bosviel, Parks & Samulyak, 2021)[†]:

$$\zeta(B) = \left(\frac{2}{B}\right)^{0.843}. \tag{5.8}$$

The most realistic model for the charge state distribution of the newly ablated material is to add it to the neutral charge state of the relevant species. Alternatively, if the ablated material is assumed to have undergone a drift motion before deposition (as discussed in chapter 4.3.1), most ablated material will be in the singly charged state, as the drift only starts once the ablated material becomes charged. However, at the relatively high plasma temperatures into which the pellets are injected, the fast ionization process of the lower charge states might introduce a problematic bottleneck in the need for time resolution. To circumvent this issue, one may deposit the ablated material directly to the equilibrium distribution of charge states associated with the local density and temperature, which can be found by solving equation (5.5) with the time derivative set to zero. This approach was used in paper **B**, while in the other papers including SPI simulations (paper **D**, **G** and **H**), the ablated material is deposited in the neutral or singly charged state as appropriate.

The width of the volume within which the ablated material is deposited may be approximated by the width of the shielding cloud around the pellet, with a radius $r_{\text{cld}} \sim 1$ cm. However, in some cases, one might be required by computational feasibility to have a radial cell size that is significantly larger than such a width of the pellet cloud, and the radial resolution then becomes the limiting length scale for the spread of the ablated material. In such cases, it is more reasonable to use a delta function deposition kernel, $h = \delta(r - \rho_{p,k})$ which, when discretized in time, translates

[†]It should however be noted that these simulations did not account for the cross-field drift of the recently ionized plasmoid, which affects the length of the plasmoid contributing the shielding (see section 4.3.1 and 4.4). It was therefore found by Samulyak *et al.* (2021) that this fit may underestimate the ablation rate by up to $\approx 30\,\%$ at high magnetic fields in certain cases.

to a uniform distribution over the distance traveled during the current time step. The impact of the radial grid step size and the use of a Gaussian deposition kernel with a finite width is investigated in Appendix C in Vallhagen (2021). These calculations verify that the width of the deposition kernel has only a formal impact on the final density profile, even when the radial grid step size is smaller than the pellet cloud width.

The deposition kernel can also be shifted compared to the pellet position, to account for the cross-field drift of the ablated material described in section 4.3.1, e.g. using the model derived in paper **C**. Although the pellet was assumed to be injected along the midplane in paper **C**, the derivation holds for an arbitrary injection geometry assuming the ablation cloud remains up-down symmetric in the poloidal plane where the pellet resides[‡]. This assumption is justified since the pellet speed is typically small compared to both the expansion and drift of the ablated material. Equation 2.32 in paper **C** then gives the drift displacement ΔR in the major radius direction, for the part of the plasmoid residing in the same poloidal plane as the pellet.

The direction of the drift will vary along the field lines, as the twisting of the field lines rotates the electrostatic potential inside the plasmoid, and hence the direction of $E \times B$. However, assuming that the electrostatic potential is constant along the field lines as in paper **C**, all ablated material will be deposited at the same flux surface; with this assumption, the electric field inside the plasmoid rotates along the field lines in such a way that the angle between the drift and the flux surface normal remains constant.

In many cases, the Alfvén current (see section 4.3.1) is negligible compared to the ohmic current. In this case, assuming constant plasma parameters and perpendicular width of the plasmoid during the drift motion, an analytical solution for ΔR is given by equation A.3 in paper **C** (this expression is however very lengthy, and is therefore not repeated here for brevity). The temperature T_{pl}, average charge Z_{pl} and perpendicular half-width Δy of the plasmoid during the drift, as well as the temperature $T_{0,\mathrm{pl}}$ in the vicinity of the pellet, are not self-consistently determined by the model, and must therefore be prescribed by the user.

The value of T_{pl} may differ significantly between different species, depending on their radiation characteristics. Pure hydrogenic pellets have been shown to have representative temperatures of a few tens of eV, while neon-doped pellets only reach $\sim 5\,\mathrm{eV}$ Müller *et al.* (2002); Matsuyama (2022). At this temperature, the neon radiation losses increase rapidly, preventing further heating. This is in line with the radiation characteristics shown in figure 6 of paper **A**, although the density and optical thickness of the plasmoid is too high for the model used in **A** to be quantitatively acurate. Typical corresponding values of the average charges are $Z_{\mathrm{avg,D}} = 1$ and $Z_{\mathrm{avg,Ne}} \approx 2$ Martín-Solís, Loarte & Lehnen (2017). Moreover, $T_{0,\mathrm{pl}} \approx 2\,\mathrm{eV}$, as this is the temperature at which the ionized fraction becomes significant. Finally, experimental measurement and simulations show that $\Delta y \sim r_{\mathrm{cld}} \sim 1\,\mathrm{cm}$

[‡]If the slab of the ablation cloud under consideration intersects the poloidal plane of the pellet at a poloidal angle θ_{cld}, the angle θ in equation 2.6 in paper **C** should be replaced by $\theta' = \theta - \theta_{\mathrm{cld}} \approx z/(qR_{\mathrm{m}})$. This ensures that $\hat{y}$ and $\hat{Y} = \mathbf{B}/B \times \hat{R}$ (see figure 1 in paper **C**) still coincide in the poloidal plane of the pellet.

Müller *et al.* (2002); Matsuyama (2022); Samulyak *et al.* (2021).

When accounting for the drift, the delta function deposition kernel should be modified as $h = \delta(r - \rho_{p,k} + \Delta r_{p,k})$, where Δr is the change in the flux surface label corresponding to the displacement ΔR. If the pellet is situated at a major radius of $R_{p,k}$ and at a height $Z_{p,k}$ relative to the horizontal midplane, we have

$$\Delta r_{p,k} = r(R_{p,k}, Z_{p,k}) - \rho_{p,k}. \tag{5.9}$$

For a general flux surface geometry, the coordinate transformation $r(R_{p,k}, Z_{p,k})$ has to be done numerically.

A more detailed description of the SPI model available in the DREAM code is given in paper **B**, with the addition of the plasmoid drift in paper **H**.

5.2 Plasma cooling

When the cold pellet material is deposited, the hot plasma is initially cooled simply by dilution of the thermal energy on the local flux surface over the new particles. Thereafter, the partially ionized particles in the deposited material dissipate the thermal energy as radiation, either directly through line radiation or indirectly by ionization, resulting in a final radiative loss during recombination. Moreover, the introduction of radiating impurities is expected to trigger or accelerate the growth of MHD instabilities resulting in a stochastisation of the magnetic field. This stochastisation increases the transport of thermal energy out of the plasma during the early parts of the disruption, as discussed in section 1.2, before the flux surfaces re-heal when the thermal quench approaches its end. The thermal energy is also affected by local ohmic heating from the thermal part of the plasma current and, at high temperatures, bremsstrahlung losses.

We now turn to the model used for the evolution of the temperature and energy density of the Maxwellian bulk of electrons, $W_\mathrm{M} = 3n_\mathrm{M}T_\mathrm{M}/2$. The part of the electron distribution function deviating from a Maxwellian is treated separately, in section 5.3. The transport of thermal energy along the stochastic magnetic field lines is expected to result in an exponential-like decay of the temperature. Thus, as a simple first approximation, one may prescribe an exponential temperature evolution from temperature $T_0(r)$ to $T_\mathrm{final}(r)$,

$$T_\mathrm{M} = T_\mathrm{final} - (T_\mathrm{final} - T_0)e^{-t/t_\mathrm{TQ}}, \tag{5.10}$$

with the characteristic thermal quench time $t_\mathrm{TQ} \sim 1$ ms.

The exponential decay model may be useful for making a first, computationally efficient, exploration of a new scenario. However, many important aspects of the interaction between the injected material and the background plasma occur via its effect on the temperature, which is not resolved by this model. Resolving these effects require a self-consistent treatment of the energy balance in the plasma, which

can be expressed as

$$\frac{\partial W_{\mathrm{M}}}{\partial t} = \frac{3}{2V'}\frac{\partial}{\partial r}\left[n_{\mathrm{M}}V'D_W\frac{\partial T_{\mathrm{M}}}{\partial r}\right] - \left(\frac{\partial W_{\mathrm{M}}}{\partial t}\right)_{\mathrm{line}} - \left(\frac{\partial W_{\mathrm{M}}}{\partial t}\right)_{\mathrm{ioniz}} + \left(\frac{\partial W_{\mathrm{M}}}{\partial t}\right)_{\mathrm{ohm}} + \left(\frac{\partial W_{\mathrm{M}}}{\partial t}\right)_{\mathrm{col}}^{\mathrm{M}} + \left(\frac{\partial W_{\mathrm{M}}}{\partial t}\right)_{\mathrm{col}}^{\mathrm{st}} + \left(\frac{\partial W_{\mathrm{M}}}{\partial t}\right)_{\mathrm{brems}} + \left(\frac{\partial W_{\mathrm{M}}}{\partial t}\right)_{\mathrm{ioniz}}^{\mathrm{abl}} + \left(\frac{\partial W_{\mathrm{M}}}{\partial t}\right)_{\mathrm{abs}}, \tag{5.11}$$

where the first four terms on the right of (5.11) typically dominate the evolution of the energy density. The dilution effect is captured by the fact that an increase in the thermal electron density n_{M} must be compensated by a drop in the temperature T_{M} to maintain a given energy density W_{M}.

The first term on the right of equation (5.11) describes a diffusive energy transport due to magnetic perturbations. When electrons follow stochastically perturbed magnetic field lines, their radial dynamics may be approximated as a diffusion process. In a tokamak geometry, a heuristic argument gives the Rechester-Rosenbluth form for the radial diffusion coefficient (Rechester & Rosenbluth, 1978)

$$D = \pi q \left|v_{||}\right| R_{\mathrm{m}} \left(\delta B/B\right)^2, \tag{5.12}$$

for a particle traveling with a speed $v_{||}$ along the field lines. The factor $\pi q R_{\mathrm{m}}$ represents the parallel correlation length scale of the stochastic magnetic field perturbation, and $\delta B/B$ is the relative amplitude of the magnetic perturbation. The local electron heat diffusion coefficient D_W is calculated by integrating the diffusion coefficient D over a Maxwellian with the local temperature T_{M}:

$$D_W = \frac{1}{\pi^{3/2} v_T^3 T_{\mathrm{M}}} \int \frac{m_e v^2}{2}\left(\frac{v^2}{v_T^2} - \frac{3}{2}\right) D(\boldsymbol{v}) \exp\left(-\frac{v^2}{v_T^2}\right) \mathrm{d}\boldsymbol{v}, \tag{5.13}$$

where $v_T = \sqrt{2T_{\mathrm{M}}/m_e}$ is the electron thermal velocity.

The transport term often dominates at the high initial temperature during a disruption. As the self-consistent calculation of the magnetic perturbations would require a three-dimensional treatment, the evolution of $\delta B/B$ is prescribed in our one-dimensional simulations. The MHD instability initiating the disruption is typically triggered by the formation of sharp gradients in the pressure or current density, in particular at flux surfaces with low order rational values of q. Such gradients may be formed by a substantial local cooling of the plasma. A plausible onset criterion may therefore be when the local temperature drops below a critical value $T_{\mathrm{crit}} \sim 10\,\mathrm{eV}$. However, as we only model the flux surface averaged temperature in this work, the model does not capture cases of strongly localized cooling in the closest vicinity of impurity doped pellet shards. An alternative onset criterion may therefore be when the doped pellet shards enter the plasma, or when a majority of the pellet shards have passed the $q = 2$ flux surface. The thermal quench onset criterion is further discussed in paper **D**.

As with the ion transport coefficients in section 5.1, the magnitude of $\delta B/B$ may be set in a way which resembles the transport found in 3D MHD simulations (see e.g. Hu *et al.* (2021)). Typical values lie in the 0.1-1% range, resulting in a

temperature drop down to $\sim 100\,\mathrm{eV}$ in a couple of milliseconds, which is of the same order of magnitude as the expected thermal quench time in ITER (Breizman *et al.*, 2019). At this point, the temperature scaling of the various cooling mechanisms typically makes transport subdominant, and the transport itself is reduced by the healing of the flux surfaces.

At temperatures of $\lesssim 100\,\mathrm{eV}$, the cooling is typically dominated by radiation and ionization losses, described by the second and third term on the right of equation (5.11), respectively. These terms can be expressed as

$$\left(\frac{\partial W_\mathrm{M}}{\partial t}\right)_\mathrm{line} = n_\mathrm{M} \sum_{ij} n_{ij} L_{ij}(T_\mathrm{M},\, n_\mathrm{M}) \tag{5.14}$$

and

$$\left(\frac{\partial W_\mathrm{M}}{\partial t}\right)_\mathrm{ioniz} = n_\mathrm{M} \sum_{ij} n_{ij} E_{ij}^\mathrm{ioniz} I_{ij}(T_\mathrm{M},\, n_\mathrm{M}), \tag{5.15}$$

where the line radiation rates L_{ij} are taken from the ADAS-database similarly to the ionization and recombination rates, and the ionization energies E_{ij}^ioniz are taken from the NIST database[§]. Note that ionization losses are still present when the net electron density does not increase, as in that case the ionization and recombination processes are still active although they balance each other. At temperatures in the few eV range, the line radiation and ionization losses are balanced by the ohmic heating, preventing the temperature from dropping further. The ohmic heating is given by

$$\left(\frac{\partial W_\mathrm{M}}{\partial t}\right)_\mathrm{ohm} = \sigma_{||} \frac{\langle \mathbf{E}\cdot\mathbf{B}\rangle}{\langle B^2\rangle} = \sigma_{||} \tilde{E}_{||}^2, \tag{5.16}$$

where $\sigma_{||}$ is the plasma conductivity and $\tilde{E}_{||}$ is a representative value of the electric field parallel to the magnetic field lines over the flux surfaces.

The cooling mechanisms considered here mainly affect the electrons directly, but the electrons can also exchange energy with the ions, which can in turn exchange energy among themselves, according to

$$\left(\frac{\partial W_i}{\partial t}\right)_\mathrm{col}^\mathrm{M} = \sum_j Q_{ij} \tag{5.17}$$

$$Q_{ij} = \left(\sum_{k=0}^{Z_i} n_i^k Z_{0,k}^2\right)\left(\sum_{l=0}^{Z_j} n_j^k Z_{0,l}^2\right) \frac{e^4 \ln\Lambda_{ij}}{2\pi^{3/2}\epsilon_0^2 m_i m_j} \frac{T_j - T_i}{\left(\frac{T_i}{m_i} + \frac{T_j}{m_j}\right)^{3/2}}. \tag{5.18}$$

Here, $W_i = 3n_i T_i/2$, and the indices i and j run over all Maxwellian populations, both ions and electrons. In this work we assume that different charge states of the same ion species have the same temperature, so i and j only run over the different ion species and not each charge state individually. Including this energy exchange can sometimes increase the need for time resolution in the simulations, and this effect was therefore omitted in papers **A**, **B**, and **D**. This essentially lowers the plasma heat capacity by a factor $\lesssim 2$, depending on the plasma composition, which

[§]`https://physics.nist.gov/PhysRefData/ASD/ionEnergy.html`

may have a significant impact on the hot-tail runaway generation, but otherwise typically has only a moderate impact on the simulation result.

The last four terms in equation (5.11) correspond to: collisional energy exchange between the superthermal (i.e. non-Maxwellian) electron population and the bulk; bremsstrahlung losses; the ionization energy required for the initial ionization of the ablated material (in case the ablated material is deposited directly to an ionized charge state); and heat being absorbed in the pellet clouds, possibly re-deposited along with the ablated material. These contributions typically play a minor role in a disruption, but are included to obtain a more accurate energy conservation. A more detailed description of the terms in equation (5.11) is given by Hoppe, Embreus & Fülöp (2021), and a more detailed summary is also given in appendix A of paper **B**.

5.3 Electric field and currents

The rapid cooling of the plasma is accompanied by a rapid drop in the conductivity, resulting in the induction of an electric field, that later decays in a diffusive manner. The electric field is related to the poloidal magnetic flux ψ_p[¶], taken to be the flux between the inner part of a flux surface and the center of the torus, according to a mean field equation given by (Boozer (2018), paper **Q**)

$$\frac{\partial \psi_\mathrm{p}}{\partial t} = U + \mu_0 \frac{\partial}{\partial \psi_\mathrm{t}} \left(\psi_\mathrm{t} \Lambda \frac{\partial}{\partial \psi_\mathrm{t}} \frac{j_{||}}{B} \right), \tag{5.19}$$

where

$$\psi_\mathrm{t} = \frac{1}{2\pi} \int_0^r V' \langle \mathbf{B} \cdot \nabla \phi \rangle dr' \tag{5.20}$$

is the toroidal flux enclosed by the flux surface labeled r and

$$U = 2\pi \frac{\langle \mathbf{E} \cdot \mathbf{B} \rangle}{\langle \mathbf{B} \cdot \nabla \phi \rangle} \tag{5.21}$$

is the loop voltage. With $\Lambda = 0$, equation (5.19) reduces to the ordinary Faraday induction law, and the last term may be added to estimate the flattening of the current density profile due to the stochasticity of the magnetic field. The poloidal flux is related to the total field line-parallel current density $j_{||}$ according to Ampère's law (disregarding the displacement current which is not relevant on the time scales of interest here),

$$2\pi\mu_0 \langle \mathbf{B} \cdot \nabla \phi \rangle \frac{j_{||}}{B} = \frac{1}{V'} \frac{\partial}{\partial r} \left(V' \left\langle \frac{|\nabla r|^2}{R^2} \right\rangle \frac{\partial \psi_\mathrm{p}}{\partial r} \right). \tag{5.22}$$

Note that during equilibrium conditions in a tokamak with a finite aspect ratio R_m/a, $j_{||}$ is not constant on the flux surfaces, but instead the ratio $j_{||}/B$ is constant.

[¶]Note that we assume a constant flux surface geometry in this work, although we evolve a value of ψ_p separate from that defining the flux surface geometry consistently with the loop voltage and current density.

We therefore typically represent the current density on a flux surface by the minimum value $j_{||,\min}$ at the outboard mid-plane of the flux surfaces.

In the limit of an infinite aspect ratio and elliptical flux surface cross sections, equations (5.19)-(5.22) reduce to

$$\mu_0 \frac{\partial j_{||}}{\partial t} = \frac{1+\kappa^{-2}}{2} \frac{1}{r} \frac{\partial}{\partial r} \left(r \frac{\partial E}{\partial r} \right), \tag{5.23}$$

where κ is the elongation.

At the plasma edge, the poloidal flux is coupled to the poloidal flux ψ_{wall} at the first toroidally conducting wall by the mutual inductance M_{ew} according to

$$\psi_{\text{edge}} = \psi_{\text{wall}} - M_{\text{ew}} I_{\text{p}}, \tag{5.24}$$

where I_{p} is the total plasma current and

$$M_{\text{ew}} = (2\pi)^2 \mu_0 \int_a^b \frac{dr}{V' \left\langle \frac{|\nabla r|^2}{R^2} \right\rangle}. \tag{5.25}$$

Here, $b \geq a$ is the effective radius of the toroidally conducting structure closest to the plasma[‖], assumed to have the same shape as the last closed flux surface. The flux at the wall is in turn given by

$$\psi_{\text{wall}} = -L_{\text{ext}}(I_{\text{p}} + I_{\text{wall}}) \tag{5.26}$$

$$U_{\text{wall}} = \frac{\partial \psi_{\text{wall}}}{\partial t} = R_{\text{wall}} I_{\text{wall}}. \tag{5.27}$$

Here, $L_{\text{ext}} = \mu_0 R_0 \ln(R_0/b)$ is the external inductance and $R_{\text{wall}} = L_{\text{ext}}/t_{\text{wall}}$ is the wall resistance, defined by the resistive time scale t_{wall} of the wall. In the cylindrical limit, with a perfectly conducting wall ($t_{\text{wall}} \to \infty$), the boundary condition reduces to $E_{||}(a) = a \ln(a/b) \partial E_{||}/\partial r|_{r=a}$.

The current density is comprised of the sum of the contribution from the ohmic current carried by the thermal bulk of electrons, and the contribution from the more energetic, superthermal electrons, including the runaway electrons, which are treated separately in our model. As a relatively simple, and thus computationally efficient, approximation, we separate the electron population into a thermal (Maxwellian) population, which carries the ohmic current density

$$\frac{j_{\text{ohm}}}{B} = \sigma_{||} \frac{\langle \mathbf{E} \cdot \mathbf{B} \rangle}{\langle B^2 \rangle} = \sigma_{||} \frac{\tilde{E}_{||}}{\sqrt{\langle B^2 \rangle}}, \tag{5.28}$$

and a runaway population characterized by the number density n_{RE} that is assumed to travel at the speed of light parallel to the field lines. The runaway population thus carries the current density

$$\frac{j_{\text{RE}}}{B} = ec \frac{n_{\text{RE}}}{\langle B \rangle}. \tag{5.29}$$

The evolution of the population n_{RE} is treated in the next section.

[‖]Note that the first wall typically consists of tiles which do not form an electrically connected closed toroidal circuit, and therefore only has a minor effect on the poloidal flux (Boozer, 2021)

5.4 Runaway electrons

The time evolution of the runaway population is determined by calculating the total flux of electrons into the runaway region of momentum space due to the various mechanisms introduced in section 2.2.2, adding transport and scrape-off losses:

$$\frac{\partial n_{\mathrm{RE}}}{\partial t} = \left(\frac{\partial n_{\mathrm{RE}}}{\partial t}\right)^{\mathrm{hot-tail}} + \left(\frac{\partial n_{\mathrm{RE}}}{\partial t}\right)^{\mathrm{Dreicer}} + \left(\frac{\partial n_{\mathrm{RE}}}{\partial t}\right)^{\mathrm{tritium}} + \left(\frac{\partial n_{\mathrm{RE}}}{\partial t}\right)^{\gamma} + \left(\frac{\partial n_{\mathrm{RE}}}{\partial t}\right)^{\mathrm{avalanche}} + \left(\frac{\partial n_{\mathrm{RE}}}{\partial t}\right)^{\mathrm{transport}} + \left(\frac{\partial n_{\mathrm{RE}}}{\partial t}\right)^{\mathrm{scrape\text{-}off}}. \tag{5.30}$$

The relatively cold post-thermal quench plasma may contain a substantial fraction of partially ionized ions and atoms. Thus, these calculations must account for the presence of both free and bound electrons, as well as the partial screening of the nuclei surrounded by bound electrons (Hesslow *et al.*, 2018*a*), which was not included in section 2.2.1. In particular, partial screening affects the collision frequencies for Coulomb collisions, as detailed in section 5.4.1.

The contributions from the various runaway generation mechanisms can be calculated either by direct numerical solution of the kinetic equation or by using approximate analytical expressions for the flux of electrons into and out of the runaway region of momentum space. The latter approach yields fluid-like sources and sinks of the population n_{RE}, as described in section 5.4.2. In section 5.4.3 we present a generalized version of the kinetic equation introduced in section 2.2.1, which may be used to more accurately account for the hot-tail and Dreicer mechanisms.

5.4.1 Collision frequencies in partially ionized plasmas

The slowing down and deflection frequencies for an electron with momentum p colliding with the background Maxwellian electron and ion populations are written here as

$$\nu_{\mathrm{s}} = \nu_{\mathrm{c}} \bar{\nu}_{\mathrm{s}}\left(\bar{p}\right) \frac{\gamma^2}{\bar{p}^3} \tag{5.31}$$

$$\nu_{\mathrm{D}} = \nu_{\mathrm{c}} \bar{\nu}_{\mathrm{D}}\left(\bar{p}\right) \frac{\gamma}{\bar{p}^3} \tag{5.32}$$

$$\nu_c = \frac{n_e e^4 \ln \Lambda_c}{4\pi\epsilon_0^2 m_e^2 c^3}, \tag{5.33}$$

where $\gamma = 1/\sqrt{1 - v^2/c^2}$ is the Lorentz factor. The normalized collision frequencies $\bar{\nu}_{\mathrm{s}}$ and $\bar{\nu}_{\mathrm{D}}$ are weak dimensionless functions of $\bar{p} = p/(m_e c)$. Since the non-Maxwellian population typically has a very small number density, collisions between non-Maxwellian electrons may usually be omitted, in line with the linearization of the kinetic equation in section 2.2.1. Moreover, when studying superthermal electrons, collisional energy diffusion (corresponding to equation (2.17) for a non-relativistic, fully ionized plasma) is typically negligible. The prefactor ν_{c} denotes a representative collision frequency (analogous to the thermal collision frequency in

equation (2.18)) with

$$\ln\Lambda_{\rm c} = \ln\Lambda_0 + \frac{1}{2}\ln\left(\frac{m_e c^2}{T_{\rm M}}\right) \tag{5.34}$$

$$\ln\Lambda_0 = 14.9 - 0.5\ln\left(n_{\rm M}/10^{20}\right) + \ln\left(T_{\rm M}/10^3\right) \tag{5.35}$$

being defined as the Coulomb logarithm for electron-electron collisions for an electron with $\gamma = 2$; the energy dependent Coulomb logarithms $\ln\Lambda_{ee}$ and $\ln\Lambda_{ei}$, for electron-electron and electron-ion collisions, respectively, are given by

$$\ln\Lambda_{ee} = \ln\Lambda_0 + \frac{1}{k}\ln\left(1 + \left(\frac{2(\gamma-1)m_e c^2}{2T_{\rm M}}\right)^{k/2}\right) \tag{5.36}$$

$$\ln\Lambda_{ei} = \ln\Lambda_0 + \frac{1}{k}\ln\left(1 + \left(\frac{2\bar{p}\sqrt{m_e c^2}}{\sqrt{2T_{\rm M}}}\right)^{k}\right) \tag{5.37}$$

$$\tag{5.38}$$

where $k = 5$ is used as an interpolation parameter between the thermal and relativistic limit. Including relativistic effects, the electron-electron contributions to the normalized collision frequencies, denoted $\bar{\nu}_s^{ee}$ and $\bar{\nu}_D^{ee}$, respectively, are given by Beliaev & Budker (1956)

$$\bar{\nu}_s^{\rm ee} = \frac{\ln\Lambda_{ee}}{\ln\Lambda_{\rm c}}\frac{\gamma^2\Psi_1 - \Theta\Psi_0 + (\Theta\gamma - 1)\bar{p}e^{-(\gamma-1)/\Theta}}{e^{1/\Theta}K_2(1/\Theta)},$$

$$\bar{\nu}_D^{\rm ee} = \frac{\ln\Lambda_{ee}}{\ln\Lambda_{\rm c}}\frac{1}{\gamma^2\bar{p}^2 e^{1/\Theta}K_2(1/\Theta)}\Big[(\bar{p}^2\gamma^2 + \Theta^2)\Psi_0 + \Theta(2\bar{p}^4 - 1)\Psi_1 + \gamma\Theta[1 + \Theta(2\bar{p}^2 - 1)]\bar{p}e^{-(\gamma-1)\Theta}\Big],$$

$$\Psi_n = \int_0^{\bar{p}} (1+s^2)^{(n-1)/2} e^{-(\sqrt{1+s^2}-1)/\Theta}\,{\rm d}s,$$

$$\Theta = \frac{T_{\rm M}}{m_e c^2},$$

where K_2 is the second-order modified Bessel function of the second kind. The electron-ion contributions $\bar{\nu}_s^{ei}$ and $\bar{\nu}_D^{ei}$, assumed to be against infinitely massive ions, with partial screening effects taken into account, are given by Hesslow *et al.* (2018*a*)

$$\bar{\nu}_s^{ei} = \frac{1}{\ln\Lambda_{\rm c}}\sum_{ij}\frac{n_{ij}}{n_{\rm M}}N_{e,ij}\left[\frac{1}{k}\ln\left(1 + h_{ij}^k\right) - \frac{\bar{p}^2}{\gamma^2}\right],$$

$$\bar{\nu}_D^{ei} = \frac{1}{\ln\Lambda_{\rm c}}\sum_{ij}\frac{n_{ij}}{n_{\rm M}}\left(\ln\Lambda_{ei}Z_{ij}^2 + g_{ij}(\bar{p})\right),$$

$$g_{ij} = \frac{2}{3}(Z_{{\rm tot},j}^2 - Z_{ij}^2)\ln[1 + (\bar{a}_{ij}\bar{p})^{3/2}] - \frac{2}{3}N_{e,ij}^2\frac{(\bar{a}_{ij}\bar{p})^{3/2}}{1 + (\bar{a}_{ij}\bar{p})^{3/2}},$$

$$h_{ij} = \frac{m_e c^2}{\mathcal{I}_{ij}}\bar{p}\sqrt{\gamma - 1},$$

$$N_{e,ij} = Z_{{\rm tot},j} - Z_{ij},$$

Here, Z_{ij} and $N_{e,ij}$ are the charge number and number of bound electrons, respectively, of charge state i of ion species j, and $Z_{\mathrm{tot},j}$ is the total atomic charge number of ion species j. The effects of partial screening enter via the ionic mean stopping power $\mathcal{I}_{ij}$ and screening length scale $\bar{a}_{ij}$ (normalised to the Bohr radius), specific for every charge state i of ion species j, both of which are tabulated in Hesslow *et al.* (2018*a*).

The slowing down frequency ν_s also contains an additional term ν_s^br accounting for the effect of radiation losses due to bremsstrahlung, based on a mean-force model Koch & Motz (1959), according to

$$\begin{aligned}\bar{\nu}_s^\mathrm{br} &= \frac{\alpha\gamma}{4\pi \ln\Lambda_\mathrm{c} n_\mathrm{M}\bar{p}} \sum_{ij} n_{ij} Z_{\mathrm{tot},j}^2 \left[\frac{12\gamma^2+4}{3\gamma\bar{p}} \ln(\gamma+\bar{p}) \right. \\ &\quad \left. - \frac{8\gamma+6\bar{p}}{3\gamma p^2} \ln^2(\gamma+\bar{p}) - \frac{4}{3} + \frac{2F[2\bar{p}(\gamma+\bar{p})]}{\gamma\bar{p}} \right], \\ F(x) &= \int_0^x \frac{\ln(1+y)}{y} \mathrm{d}y, \end{aligned} \tag{5.39}$$

where $\alpha \approx 1/137$ is the fine-structure constant. The effects of screening of partially ionized impurities on the bremsstrahlung emission have been ignored, so that the ions are only included in this expression through their total charge and density.

5.4.2 Fluid runaway sources

The fluid runaway sources presented in this section are all calculated by integrating approximate analytical sources of energetic electrons over momenta higher than a critical momentum, similar to the one introduced in section 2.2.2, determined by the electric field and collision frequencies. This critical momentum may be determined by solving the *bounce averaged* kinetic equation (Hoppe, Embreus & Fülöp, 2021), i.e. the kinetic equation averaged over the gyro-motion and the poloidal motion (recall from section 1.1), including an arbitrary source.

In an arbitrary tokamak geometry, one finds that the probability for an electron to become a runaway may be approximated as a step function at the critical momentum (Hoppe, Embreus & Fülöp, 2021)

$$p_\mathrm{c} = m_e c \left(\frac{\{\bar{\nu}_\mathrm{s}(\bar{p}_\star)\bar{\nu}_\mathrm{D}(\bar{p}_\star) + 4\bar{\nu}_\mathrm{s}(\bar{p}_\star)^2\}\, E_\mathrm{c}^2}{f_\mathrm{p}(\tilde{E}_{||} - E_\mathrm{c}^\mathrm{eff})^2} \right)^{1/4}, \tag{5.40}$$

with the corresponding critical energy $W_\mathrm{c} = m_e c^2 \sqrt{1+\bar{p}_\mathrm{c}^2}$. The factor f_p denotes the fraction of the particles having passing orbits. This expression was obtained by matching the solution to the runaway probability problem in various limits of the collision and electric field acceleration terms in the bounce averaged kinetic equation. Thus, we calculate the flux surface averaged runaway density by integrating the analytical sources over momenta larger than this value. The critical momentum $p_\star$

in the limit where $\bar{\nu}_\mathrm{D} \gg \tilde{E}_{||}/E_\mathrm{c} \gg 1$ is given implicitly by

$$p_\star = m_e c \sqrt{\frac{\sqrt{\bar{\nu}_\mathrm{s}(\bar{p}_\star)\bar{\nu}_\mathrm{D}(\bar{p}_\star)}}{\tilde{E}_{||}/E_\mathrm{c}}}. \tag{5.41}$$

The effective critical electric field $E_\mathrm{c}^\mathrm{eff}$ is defined here as the lowest electric field which allows runaway acceleration when taking into account the energy dependence of the Coulomb logarithm and screening effects, as well as bremsstrahlung and synchrotron radiation losses due to the gyro-motion of the electrons. These effects were not accounted for in the expression for E_c introduced in section 2.2.2. An expression for $E_\mathrm{c}^\mathrm{eff}$ was derived by Hesslow *et al.* (2018*b*), and a method for calculating $E_\mathrm{c}^\mathrm{eff}$ in an arbitrary tokamak geometry is described in appendix C2 of Hoppe, Embreus & Fülöp (2021).

For the tritium decay and Compton scattering sources, the flux of electrons into the runaway region can be calculated by directly integrating the corresponding source terms over the runaway region of momentum space. The runaway seed produced by tritium decay then becomes (Martín-Solís, Loarte & Lehnen (2017), Paper **K**)

$$\left(\frac{\partial n_\mathrm{RE}}{\partial t}\right)^\mathrm{tritium} = \ln(2)\frac{n_\mathrm{T}}{\tau_\mathrm{T}} f(W_\mathrm{c}), \tag{5.42}$$

where n_T is the tritium density, $\tau_\mathrm{T} \approx 4500$ days is the half-life of tritium. The fraction of the electrons created by tritium β^- decay above the critical runaway energy is given by $f(W_\mathrm{c}) \approx 1-(35/8)w^{3/2}+(21/4)w^{5/2}-(15/8)w^{7/2}$, with $w = W_\mathrm{c}/Q$ and $Q = 18.6\,\mathrm{keV}$, corresponding to the maximum energy of the β^- electrons.

Runaway generation due to Compton scattering of gamma photons from the activated wall takes the form

$$\left(\frac{\partial n_\mathrm{RE}}{\partial t}\right)^\gamma = n_\mathrm{tot} \int_{W_\mathrm{c}}^\infty \Gamma_\gamma(E_\gamma)\sigma(E_\gamma)dE_\gamma, \tag{5.43}$$

where $\Gamma(E_\gamma)$ is the gamma photon energy spectrum and $\sigma(E_\gamma)$ is the total Compton scattering cross-section as a function of the gamma photon energy E_γ (Martín-Solís, Loarte & Lehnen, 2017). The gamma photon energy spectrum depends on the details of the geometry, irradiation and material of the tokamak wall, and therefore varies between different machines. An estimated spectrum for ITER, which is of most interest in this work, obtained using radiation transport calculations performed at several poloidal locations, is available in Martín-Solís, Loarte & Lehnen (2017). The dependence on the total electron density n_tot, rather than the free electron density, reflects the fact that the gamma photon energies are much larger than the ionization energies of the ions and atoms in the plasma. Thus, the bound electrons may be scattered into the runaway momentum region essentially to the same extent as the free electrons.

The calculation of the remaining runaway sources requires an approximate analytical or numerical solution to the kinetic equation introduced in section 2.2. For the Dreicer mechanism, this is done by using a neural network trained on output

from kinetic simulations (Paper **J**), evaluated at the representative parallel electric field $\tilde{E}_{||}$.

The growth rate for the avalanche process is calculated based on an asymptotic matching of solutions to the kinetic equation in various limits, similar to that made for p_c above**, and is given by (Paper **I**)

$$\left(\frac{\partial n_\mathrm{RE}}{\partial t}\right)^\mathrm{avalanche} = \frac{e^4 n_\mathrm{tot} n_\mathrm{RE}}{4\pi\epsilon_0^2 m_\mathrm{e}^2 c^3 \bar{p}_\mathrm{c}'^2} = \frac{e n_\mathrm{RE}}{m_\mathrm{e} c \ln\Lambda_\mathrm{c}} \frac{n_\mathrm{tot}}{n_\mathrm{M}} \frac{\tilde{E}_{||} - E_\mathrm{c}^\mathrm{eff}}{\sqrt{4 + \bar{\nu}_\mathrm{S}(\bar{p}_\star)\bar{\nu}_\mathrm{D}(\bar{p}_\star)}}. \tag{5.44}$$

Here we have disregarded the trapping factor f_p due to the expected fast detrapping by collisions expected in high-density post-injection plasmas (McDevitt & Tang, 2019). The factor $n_\mathrm{tot}/n_\mathrm{M}$ reflects the fact that the runaway electrons typically reach energies much higher than the ionization potential of the bound electrons, making them available as target electrons for the avalanche process, while they do not contribute to the frictional drag to the same extent as free electrons for $E_{||} \gg E_\mathrm{c}^\mathrm{eff}$. Thus, the avalanche growth rate typically increases with an increased ratio of bound electrons.

The hot-tail runaway generation may be estimated by calculating an approximate solution to the kinetic equation, assuming that the distribution function is isotropic to leading order, and that the shape of the distribution function is mostly unaffected by the electric field. The electric field then enters by determining the momentum p_0 above which electrons are counted as runaways. The problem may be simplified further by utilizing that the plasma is typically nearly fully ionized while the hot-tail mechanism is active, and the slowing down is dominated by collisions. For a distribution f_0 having initial density n_0 and temperature T_0, which slows down due to collisions with a cold population with density n_M, the solution to the kinetic equation under these approximations was found by Smith & Verwichte (2008) to be

$$f_0 = \frac{n_0}{\pi^{3/2} p_\mathrm{th0}^3} \exp\left\{\left(-\frac{(\bar{p}^3 + 3\tau)^{2/3}}{\bar{p}_\mathrm{th0}^2}\right)\right\} \tag{5.45}$$

$$\tau = \int_0^t \nu_c dt. \tag{5.46}$$

Here, $p_\mathrm{th0} = \sqrt{2T_0/m_e}$ is the initial thermal momentum and τ is the time integral of the relativistic electron-electron collision frequency (equation (5.33)). The corresponding hot-tail runaway generation is

$$\left(\frac{\partial n_\mathrm{re}}{\partial t}\right)^\mathrm{hot-tail} = -4\pi p_0^2 \frac{\partial p_0}{\partial t} f_0(t, p_0). \tag{5.47}$$

Rather than counting all electrons with momentum $p > p_\mathrm{c}$ as runaways here, it has been shown by Svenningsson *et al.* (2021) that the model accuracy at high plasma charge is improved by taking p_0 as the momentum where the net momentum

**The critical momentum p_c' differs from p_c in equation (5.40) by a factor $\bar{\nu}_\mathrm{s}^2$ in the second term in the numerator, due to a slightly different choice of expression for the asymptotic matching described above.

flux vanishes. In an arbitrary tokamak geometry, this condition can be written as (Hoppe, Embreus & Fülöp, 2021)

$$\left[\frac{\nu_\mathrm{c} m_e c\gamma^2}{\bar{p}^2} f_0 + f_\mathrm{p}\frac{e^2\tilde{E}_{||}^2\bar{p}^3}{3(1+Z_\mathrm{eff})\nu_\mathrm{c}\gamma}\frac{\partial f_0}{\partial p}\right]_{p=p_0} = 0. \tag{5.48}$$

The first term accounts for the collisional slowing down and the second term represents the electric field acceleration.

The magnetic perturbations initiating the disruption will also lead to a transport of runaways as they follow the stochastic field lines, eventually leaving the plasma. This transport may be described by a diffusion coefficient of a similar form as equation (5.12), for electrons of a given momentum. The simplest approach, used in paper **B**, is to directly use equation 5.12 with $v_{||} = c$ (runaway electrons tend to have relatively low pitch angles θ, defined as $\cos\theta \equiv \xi = p_{||}/p$). However, the transport is expected to decrease at high momenta, when the deviation from the original field line over one poloidal revolution becomes larger than the correlation length of the magnetic field perturbation (Hauff & Jenko, 2009). This decrease in the transport may approximately be accounted for by a diffusion coefficient of the form (paper **O**)

$$D = \pi q R_\mathrm{m} c\left(\frac{\delta B}{B}\right)^2 \frac{\bar{p}}{1+\bar{p}^2}. \tag{5.49}$$

It also has to be taken into account that the runaway electrons do not follow a Maxwellian distribution function. Paper **O** derives the diffusion coefficient assuming that the runaway electron distribution function is dominated by the avalanche mechanism, which is the case the majority of the time during ITER disruptions. In this case, the distribution function for the runaways may be approximated by

$$f_\mathrm{RE} = n_\mathrm{RE}\frac{n_\mathrm{tot}}{n_\mathrm{M}}\frac{1}{\ln\Lambda_\mathrm{c}\sqrt{4+\bar{\nu}_\mathrm{S}(\bar{p}_\star)\bar{\nu}_\mathrm{D}(\bar{p}_\star)}}\exp\left(\frac{n_\mathrm{tot}}{n_\mathrm{M}}\frac{\bar{p}-\bar{p}_*}{\ln\Lambda_\mathrm{c}\sqrt{4+\bar{\nu}_\mathrm{S}(\bar{p}_\star)\bar{\nu}_\mathrm{D}(\bar{p}_\star)}}\right)\frac{Ae^{A\xi}}{2\sinh A}, \tag{5.50}$$

with $A = 2\bar{E}_{||}/(E_\mathrm{c}\bar{p}\bar{\nu}_\mathrm{D})$. The transport term then takes the form

$$\left(\frac{\partial n_\mathrm{RE}}{\partial t}\right)^\mathrm{transport} = \frac{1}{V'}\frac{\partial}{\partial r}(V'\Gamma_\mathrm{RE}), \tag{5.51}$$

with

$$\Gamma_\mathrm{RE} = \int_{\bar{p}_*}^{\infty}\int_{-1}^{1} -D\frac{\partial f_\mathrm{RE}}{\partial r}d\xi d\bar{p}. \tag{5.52}$$

In addition to transport, runaway electrons may also be lost due to the vertical plasma motion, causing the plasma to be scraped off against the wall (as discussed in section 3.2). In paper **G**, we account for the scrape-off by a loss term of the form

$$\left(\frac{\partial n_\mathrm{RE}}{\partial t}\right)^\mathrm{scrape\text{-}off} = \frac{n_\mathrm{RE}}{\tau_\mathrm{loss}}\Theta(r - r_\mathrm{LCFS}), \tag{5.53}$$

where τ_{loss} is the loss time scale, Θ is the Heaviside step function and r_{LCFS} is the flux surface label of the last closed flux surface, which decreases with time as the plasma is scraping off against the first wall. The loss time scale is determined by the time it takes the runaway electrons to travel along the field lines to the wall on an open flux surface, $\tau_{\text{loss}} \sim R_{\text{m}} \sim 10^{-8}\,\text{s}$. This time scale is however several orders of magnitude shorter than the other time scales of interest, and one may therefore set $\tau_{\text{loss}} \sim 10\Delta t$, where Δt is the numerical time step, to avoid increasing the need for time resolution without loss of accuracy.

The location of the last closed flux surface may be estimated by utilizing the fact that the poloidal flux at the last closed flux surface is essentially constant on the resistive time scale of the conducting wall (which is typically long compared to the current quench duration in ITER) (paper **G**). This may be intuitively understood by considering that any changes in the poloidal flux at a highly conducting wall, which is closely linked to the flux at the last closed flux surface, would induce currents inside the wall which would cancel the change in the flux. Thus, r_{LCFS} may be estimated by (numerically) solving

$$\psi_{\text{p}}(r_{\text{LCFS}}) = \psi_{\text{p}}(a, t = 0). \tag{5.54}$$

It has been shown in 2D axisymmetric simulations by Wang *et al.* (2024) that the poloidal flux is constant to a good accuracy during the majority of the runaway generation phase in representative ITER cases. In paper **G** it was also confirmed that the above model was able to accurately reproduce the runaway avalanche gain in one of the ITER cases studied by Wang *et al.* (2024). It should however be pointed out that this model is usually not suited to study the termination of a long-lasting runaway plateau due to scrape-off, as the lifetime of such a runaway plateau may be comparable to or longer than the resistive time scale of the conducting wall, even for a highly conducting device such as ITER. This model is instead adapted to study runaway losses mostly overlapping with the generation phase, during which the assumption of a constant poloidal flux at the last closed flux surface remains valid.

5.4.3 Kinetic equation

For many purposes, the runaway current may be calculated with sufficient accuracy by the analytical generation rates given above, without needing to resolve any further details of the electron momentum distribution function. This enables simulating a full disruption scenario with a computational cost of $\lesssim 1$ CPU hour. However, in order to accurately capture the hot-tail mechanism, which is an intrinsically transient phenomenon sensitive to the details of the electron distribution function, it is necessary to solve the kinetic equation self-consistently with the temperature evolution, for at least a part of the momentum space.

In order to do this in a computationally efficient manner, we only resolve electrons with up to mildly relativistic momenta, $p < p_{\text{RE}} \sim m_{\text{e}}c$, on the kinetic grid. Electrons passing this upper boundary are added to a fluid-like runaway electron population, again characterized by a density n_{RE}, and are approximated to travel with the speed of light, as above. We also introduce a momentum $p_{\text{hot}} \sim 10p_{\text{th}}$, separating the

Maxwellian electrons and the hot (superthermal) electrons with $p_{\mathrm{hot}} < p < p_{\mathrm{RE}}$, in the sense that only electrons with $p < p_{\mathrm{hot}}$ are considered to be part of the density n_{M} involved in the calculations of the plasma density and temperature evolution described in sections 5.1 and 5.2.

Using the above division of the momentum space, we resolve the part of momentum space with $p < p_{\mathrm{RE}}$ by solving the bounce-averaged kinetic equation with a linearized relativistic test particle Coulomb Fokker-Planck collision operator, introduced in section 2.2.1. The reference Maxwellian around which this collision operator is linearised is defined by the density n_{M} and temperature T_{M}, as calculated by equations (5.11) and (5.5), and the quasi-neutrality condition. As the kinetic equation is invoked here to study the comparatively small non-Maxwellian population, while the Maxwellian population characteristics are evolved by equations (5.11) and (5.5), the field particle term in equation (2.13) is omitted. We also neglect the collisional energy-diffusion part of the test particle term, an assumption strictly valid in the superthermal limit. The slowing down and deflection frequencies in the test particle operator are now those accounting for the energy dependence of the Coulomb logarithm, as well as the effect of partial screening in collisions with partially ionized impurities, as summarized in section 5.4.1.

When explicitly resolving the momentum space dynamics in this work, in paper **B**, we consider the cylindrical limit, thus avoiding complications which may arise due to the presence of trapped particles when the aspect ratio is finite (Hoppe, Embreus & Fülöp, 2021). We also do not resolve the tritium decay and Compton scattering sources on the kinetic grid, but add the contribution from these sources directly to the fluid-like runaway population. Simulations where these sources are resolved kinetically are however available in paper **T** and Ekmark *et al.* (2025). Finally, we make the conservative simplification of disregarding the effect of transport along stochastic field lines on the distribution function. When resolving the full distribution function with $p < p_{\mathrm{RE}}$, this decreases the run-time of the simulation by about an order of magnitude, from ~ 100 CPU hours to ~ 10 CPU hours, thus enabling exploration of a more extensive parameter space[††].

Using the coordinates p and ξ, and inserting the cylindrical configuration space geometry, this kinetic equation reads

$$\frac{\partial f}{\partial t} + eE\left(\frac{1}{p^2}\frac{\partial}{\partial p}\left[p^2\xi f\right] + \frac{1}{p}\frac{\partial}{\partial \xi}\left[\left(1-\xi^2\right) f\right]\right) = \frac{1}{p^2}\frac{\partial}{\partial p}\left[p^3\nu_s f\right] + \frac{\nu_D}{2}\frac{\partial}{\partial \xi}\left[(1-\xi^2)\frac{\partial f}{\partial \xi}\right] + S\delta(\boldsymbol{p}). \tag{5.55}$$

The strength S of the delta function source term at $\boldsymbol{p} = \boldsymbol{0}$ is determined by the requirement that the total number of particles on the kinetic grid must satisfy quasi-neutrality, $\int f(\boldsymbol{p}) d\boldsymbol{p} = n_{\mathrm{free}} - n_{\mathrm{RE}}$.

[††]The computational cost is however significantly lower when only resolving the initial hot electron population on the kinetic grid, using a model similar to that in Aleynikov & Breizman (2017), as in the "superthermal" or "isotropic" mode in the DREAM code (Hoppe, Embreus & Fülöp, 2021). These models have been used for extensive parameter scans, with the effect of transport along stochastic field lines on the distribution function included (paper **T**, Svenningsson *et al.* (2021), Ekmark *et al.* (2025)).

The solution to equation (5.55) is then used to calculate the current density j_{hot} carried by the hot population and momentum space flux F_{p} across the upper boundary p_{RE}:

$$F_{\mathrm{p}} = 2\pi p^2 \int\limits_{p=p_{\mathrm{RE}}} (eE_{||}\xi - p\nu_s) f d\xi. \tag{5.56}$$

This momentum space flux then corresponds to the sum of the hot-tail and Dreicer runaway generation mechanisms. The thermal bulk of the distribution function also partly accounts for the ohmic current. However, neglecting the field particle term in the collision operator leads to an underestimation of the current carried by the thermal bulk. The remaining contribution to the ohmic current is therefore added manually, such that

$$j_{\mathrm{ohm}} = E_{||}(\sigma_{||} - \sigma_{||,\mathrm{tp}}) + \int\limits_{p<p_{\mathrm{hot}}} ev_{||} f d\boldsymbol{p}. \tag{5.57}$$

The contribution $\sigma_{||,\mathrm{tp}}$ to the conductivity from the test particle collision operator was found by running several DREAM simulations with fixed parameters until the current carried by the thermal bulk was equilibrated. An analytical expression was then fitted to the result according to (Hoppe, Embreus & Fülöp, 2021)

$$\sigma_{||,\mathrm{tp}} = \sigma_{||}\left(1 - \frac{1.406}{1.888 + Z_{\mathrm{eff}}}\right). \tag{5.58}$$

Finally, noting that B is constant over a given flux surface in the cylindrical limit considered here, the total current density can be expressed as

$$j_{||} = j_{\mathrm{ohm}} + j_{\mathrm{hot}} + ecn_{\mathrm{RE}}, \tag{5.59}$$

with the time evolution of the runaway population determined by

$$\begin{aligned}\frac{\partial n_{\mathrm{RE}}}{\partial t} = F_{\mathrm{p}} &+ \left(\frac{\partial n_{\mathrm{RE}}}{\partial t}\right)^{\text{tritium}} + \left(\frac{\partial n_{\mathrm{RE}}}{\partial t}\right)^{\gamma} \\ &+ \left(\frac{\partial n_{\mathrm{RE}}}{\partial t}\right)^{\text{avalanche}} + \left(\frac{\partial n_{\mathrm{RE}}}{\partial t}\right)^{\text{transport}} + \left(\frac{\partial n_{\mathrm{RE}}}{\partial t}\right)^{\text{scrape-off}}.\end{aligned} \tag{5.60}$$

5.5 Numerical tools

Having described our model from a physics point of view, we here give a brief overview of the numerical tools GO (Fehér *et al.* (2011), paper **A**) and DREAM (Disruption Runaway Electron Analysis Model) (Hoppe, Embreus & Fülöp, 2021) used for the numerical studies in papers **K**-**A** and paper **B**, respectively. Based on an input specifying the injection parameters and pre-disruption plasma conditions, both codes are capable of self-consistently calculating the time evolution of the background plasma properties, the runaway current and, for the DREAM code, the electron momentum distribution function, during a mitigated tokamak disruption.

The GO code is a purely fluid model, in the sense that it does not resolve any details of the electron momentum distribution function, but merely treats a

thermal population assumed to have a Maxwellian momentum distribution and a runaway population assumed to travel with the speed of light. Thus, we do not use the GO code to study the hot-tail mechanism in this work. The evolution of the total (i.e. sum of all charge states) ion density of the injected material is directly prescribed by the user. The radial discretization is made using the finite difference method, with the radial derivatives calculated using the central approximation. The time stepping is performed using the Crank-Nicolson scheme for the electric field diffusion equation (5.23) and the diffusion term in the runaway density equation (5.30), while for the other terms it is performed using the Euler forward scheme. With its relatively simple and modular design, the code is well suited to quickly implement and explore new components of the disruption model.

In addition to the modeling capabilities of the GO code, the DREAM code also offers the possibility to solve for the electron momentum distribution function, making it more suitable for studies of e.g. the hot-tail runaway generation mechanism where such information is needed. Moreover, in paper **B**, the DREAM code was extended with the capability of modeling an SPI with input parameters specifying the size, composition and shattering of the pellet and the velocity distribution of the shards, instead of simply prescribing the evolution of the total injected density.

The equation system in DREAM is discretized using a finite volume method (see e.g. Karney (1986)) for the momentum and configuration space, and a backward Euler scheme for the time evolution. Approximating the momentum and configuration space derivatives with central differences, the differential equations included in the model are translated into an algebraic equation system for the cell averages of the various quantities at the next time step. The evolved quantities are thus computed in the center of the cells, while the fluxes between adjacent cells are calculated on the cell surfaces, ensuring that the flux into a grid cell exactly equals the flux out of adjacent grid cells. This guarantees conservation of the integrals of the various quantities to within machine precision, in the absence of sources and edge losses. The interpolation from the center of the cells to the cell boundaries, needed for the calculation of the fluxes, is performed in such a way as to preserve positivity of the evolved quantities.

The implicit solution for the evolved quantities in the next time step is obtained via Newton iteration, using a Jacobian constructed based on analytical derivatives, although some are approximated, or even neglected, to limit the complexity of the construction and inversion of the Jacobian. The iteration starts at the vector containing all the evolved quantities in the previous time-step, and continues until a tolerance specified by the user is satisfied separately for every evolved quantity.

Chapter 6

Summary and outlook

Disruptions are a severe threat to the future of fusion energy based on the tokamak design. A reliable disruption mitigation system is of utmost importance for the success of future large, high-current devices such as ITER. The currently envisaged method of mitigation is to inject massive amounts of material into the plasma, aiming to rapidly cool the plasma in a controlled way. The injected material can be delivered in a variety of ways, such as in the form of a gas released from a pressurized vault or in the form of a Shattered Pellet Injection (SPI), with the latter being chosen as the basis for the ITER disruption mitigation system. The objectives of the disruption mitigation system concern three main issues: mitigation of the localized heat loads and electromagnetic forces on the vessel, and the reduction of the runaway current generation. The mitigation of the localized heat loads is achieved by isotropically dissipating the thermal energy content through radiation. To avoid excessive electromagnetic forces, the current quench time must be long enough to sufficiently reduce the eddy currents induced in the structures surrounding the plasma, but short enough to avoid excessive halo currents. Finally, the runaway current must be sufficiently low to avoid substantial damage upon wall impact.

A detailed understanding and modeling capability of tokamak disruptions mitigated by massive material injection is crucial in order to guide the design and operation of the disruption mitigation system. This is the topic to which this thesis aims to contribute. This chapter summarizes the main findings of the attached papers in section 6.1, along with a summary of the current status, most critical remaining questions and suggestions for future research in section 6.2.

6.1 Summary of papers

The papers included in this thesis follow two main trails of research, partly converging in paper **H**. In papers **A**,**B**, **D**, **G** and **H**, we perform numerical simulations of tokamak disruptions and their mitigation by massive material injection, considering increasingly advanced scenarios and physics fidelity. In papers **C**, **E** and **F**, we contribute to the development of the theory of pellet injections, in particular the displacement of the ablated material due to the plasmoid drift and the pellet (shard) acceleration due to the rocket effect. The aim is to develop analytical models suitable to account for these effects in integrated modeling frameworks such as DREAM

without significantly increasing the computational cost. The plasmoid drift model defined in paper **C** is finally implemented in DREAM in paper **H**, where it is used to study the effect of the drift on the density build-up and disruption dynamics of SPI mitigated disruptions in ASDEX Upgrade and ITER.

In paper **A**, we perform an initial set of GO simulations of disruptions in deuterium-tritium plasmas in ITER, mitigated by the injection of a mixture of deuterium and neon or argon, evaluating the current quench time and runaway current generated for a wide range of injected densities. The initial part of the temperature drop, where the transport due to the stochastization of the magnetic field is expected to play a major role, is modeled by an exponential decay down to ~ 100 eV. After this, the energy balance is calculated self-consistently, accounting for radiation losses and Ohmic heating. This calculation assumed that the plasma is completely transparent to all radiation. The injected material is assumed to be instantly deposited in the neutral state with a homogeneous density profile at $t = 0$. The flux surfaces are assumed to have an infinite aspect ratio with a circular or elliptical cross-section, and the conducting wall (where the boundary condition for the poloidal flux is set) is assumed to have a 15 cm larger radius than the plasma and be infinitely conductive.

One of the main objectives of **A** was to study how the runaway generation is affected by the partial screening of the partially ionized ions and atoms present in the cold post-disruption plasma. This was done by implementing the new models accounting for these effects on the Dreicer and avalanche mechanisms, which were first demonstrated in papers **J** and **I**, respectively. We also account for the runaway generation due to tritium decay and Compton scattering of gamma photons from the radioactive wall, using the models from Martín-Solís, Loarte & Lehnen (2017) and paper **K**. These generation mechanisms are also affected by effects of partial screening, entering via the critical momentum for runaway acceleration*. In this paper the hot-tail mechanism was neglected, as no efficient kinetic solver or adequate model for the transport losses during the thermal quench was available at the time. However, as discussed in papers **A** and **D**, when the runaway plateau current is within an order of magnitude of the initial plasma current, the plateau current is only logarithmically sensitive to the seed current. This low sensitivity stems from the fact that when the runaway current becomes macroscopic and slows down the total current decay, it reduces the induced electric field, thus reducing any further runaway generation. As long as there are other sources present producing a significant seed, in this case the nuclear sources, neglecting the hot-tail generation is not expected to have a major qualitative influence on the results.

We find that the partial screening substantially increases the runaway generation, compared to the results obtained assuming a complete screening of the nuclei carrying bound electrons. This is explained by the shift in the balance between the frictional drag and contribution to the number of target electrons for the avalanche mechanism in the presence of bound electrons, as discussed in section 5.3. The increase can be counteracted to some extent by combining the neon or argon injection

*In this paper the critical momentum was calculated using the expression in equation (5.41), derived in the somewhat simplified limit of high electric fields and effective plasma charge, rather than equation (5.40) used in the later papers.

with a large amount of deuterium, which remains ionized at lower temperatures. However, when the injected quantities become large enough, the temperature starts to drop as low as $\sim 1\,\mathrm{eV}$ already when there is still a significant Ohmic current left in the plasma. When this happens, the deuterium also starts to recombine, which substantially increases the avalanche generation, converting a significant fraction of the remaining Ohmic current into a runaway current. At this point, the runaway current starts to increase with an increased amount of injected deuterium. Moreover, if the injected quantities are too low, the radiative cooling is found to be insufficient to cause a complete thermal quench, leaving the equilibrium temperature in the ~ 100 eV range. This results in a high post-thermal quench plasma conductivity and thus a too long current quench time. Within the range of injection parameters giving an acceptable current quench time, the lowest runaway current found was 3.7 MA.

Some of the simplifications in paper **A** are improved upon in paper **B**, where we use the recently developed DREAM code to study mitigated ITER disruptions, including a kinetic calculation of the hot-tail runaway generation. For this paper, an SPI model is implemented in DREAM, allowing for a self-consistent calculation of the assimilation of the injected material. Moreover, all parts of the temperature drop are now calculated self-consistently, with the transport due to the stochastization of the magnetic field accounted for by a diffusion term of the Rechester-Rosenbluth form, as described in section 5.2. The perturbation was assumed to be active while any neon-containing pellet shards remain in the plasma, with an amplitude chosen to give a transport loss time scale in the millisecond range. A major advantage of this model compared to prescribing an exponential temperature drop is that it makes it possible to estimate the fraction of the thermal energy lost by transport. This can be used as a measure of the performance concerning the mitigation of localized heat loads. However, to avoid the computational complexity of transporting particles between the radial grid points on the kinetic grid, the radial transport of the superthermal electrons is still neglected, and thus the calculated runaway currents should be interpreted as upper estimates. Finally, the line radiation and ionization/recombination model is updated to account for the opacity to the resonant Lyman lines of the hydrogen species expected at large deuterium densities. The main research objective of this paper is to evaluate the performance of the two-stage SPI mitigation scheme recently suggested for ITER, described in section 3.4.1.

The two-stage injection scheme was found to significantly impede the thermal energy transport due to magnetic perturbations, which can reduce localized heat loads. This is explained by the decrease in the thermal motion due to the dilution cooling in the first stage, before the stochastization of the magnetic field, which effectively reduces the cross-field transport possible along the stochastic magnetic field lines. Moreover, this injection scheme was found to effectively reduce the hot-tail runaway seed generation by several orders of magnitude. This reduction can be explained by the intermediate equilibration of the hot tail of the electron distribution between the injections, as discussed in section 3.4.1. Notably, this strong reduction was obtained despite the conservative assumption that the superthermal electrons were not affected by the magnetic field perturbations.

For the final runaway current, a non-monotonic dependence on the injected deuterium density similar to that observed in paper **A** was also found here. However,

the opacity to Lyman radiation was found to significantly reduce the cooling at temperatures $\lesssim 2$ eV, resulting in a shift of the deuterium recombination, and the related enhancement of the runaway avalanche, towards higher injected densities. For a non-nuclear plasma, i.e. in the absence of runaway generation due to tritium decay and Compton scattering, when accounting for opacity to Lyman radiation, the runaway current was found to be below the acceptable limit when injecting a deuterium pellet containing $\gtrsim 10^{24}$ atoms, with a rather weak dependence on the amount of injected neon in the range of $10^{22} - 10^{25}$ atoms. For activated operation, on the other hand, no such scenarios were found, and the lowest runaway currents found (again, within the range of injection parameters also giving an acceptable current quench time) were in the 3-4 MA range, similar to the results of paper **A**.

The physics fidelity and the complexity of the studied scenarios are increased further in paper **D**. The increase in the physics fidelity includes the addition of ion advection and diffusion, runaway losses calculated using the model in paper **O** and the use of a realistic toroidal geometry of the flux surfaces and the conducting wall, which now has a realistic conductivity. Notably, the wall radius is now almost 1 m larger than the plasma minor radius, corresponding to the first toroidally conducting wall. This change was implemented as it was realized that the wall closest to the plasma consists of electrically insulated tiles which only have a minor effect on the poloidal flux. To lower the computational cost, the hot-tail runaway generation was calculated using the fluid model equation (5.47).

In this paper, a set of new reference disruption modeling scenarios were also established. Four different initial plasma configurations were investigated, with varying plasma current and core temperatures as the main difference. The initial plasma profiles and the flux surface geometry were taken from simulations with the CORSICA code Kim, Casper & Snipes (2018), and the injected impurity concentrations were tailored to span current quench times ranging from 50 ms to 100 ms in certain test cases. Instead of assuming a pre-determined thermal quench onset, two different onset criteria are considered: one assuming that the thermal quench starts when any neon-containing shards pass the flux surface with $q = 2$, resulting in a relatively early onset; and one assuming that the thermal quench starts when the temperature falls below 10 eV anywhere inside the $q = 2$ flux surface, resulting in a relatively late onset. The thermal quench is then assumed to last for either 1 ms or 3 ms, with the perturbation level scaled such that the core temperature drops to 200 eV in preparatory simulations with transport as the only loss mechanism, after which the cooling is expected to be dominated by radiation.

The conclusions of this paper largely corroborate the findings of papers **A** and **B**. In some cases, particularly cases with a late thermal quench, it is found to be possible to separate the cooling into two phases even with a single stage injection. This is attributed to the fact that the cooling is naturally slowed down in the ~ 100 eV range due to a local minimum in radiated power (see e.g. figure 6 in paper **A**). Two-stage injections are however found to more robustly achieve the lowest possible runaway current. In cases without radioactive runaway sources, several cases are found where the seed runaway current calculated in the simulation corresponds to much less than a single relativistic electron, even for initial plasma currents of 15 MA. Due to the continuous statistical approach underlying the model, this current is still

amplified by the runaway avalanche, resulting in a $\sim 1\,\mathrm{MA}$ plateau current in the simulation. Nevertheless, accounting for the discreteness of charge, these cases may still be interpreted as having a successful runaway mitigation, unless a finite seed is generated by a mechanism not included in the model. However, in the presence of the radioactive runaway sources, no such cases are found, as in paper **B**.

One of the main differences between papers **B** and **D** is that the lowest runaway currents found in activated scenarios is around 6 MA in paper **D**, and increase by $\sim 2\,\mathrm{MA}$ compared to paper **B**. This difference is attributed to the increased radius and finite conductivity of the conducting wall, increasing the amount of magnetic energy inside the vessel available to contribute to the runaway avalanche. Assuming a perfectly conducting wall immediately at the plasma edge reduces the plateau current in the best performing cases to $\approx 1.5\,\mathrm{MA}$, highlighting the importance of the boundary condition of the poloidal flux.

The large impact of varying the boundary condition for the poloidal flux suggests that the runaway generation may be significantly affected by the vertical plasma motion, which is the subject of paper **G**. Here a model is proposed for the scrape-off losses of runaway electrons overlapping with the generation phase, which is compatible with a model with otherwise fixed flux surface geometry. The model is based on the fact that the poloidal flux at the plasma edge is similar to the flux at the conducting wall, which cannot change significantly on time scales shorter than the resistive time scale of the conducting wall. Thus, if this time scale is long compared to the current quench time, the radius of the last closed flux surface may be estimated by the radius at which the flux is equal to the initial flux at the plasma edge during this phase of the disruption. A loss term may then be applied which quickly removes all runaways outside this flux surface (see section 5.4.2 around equation (5.53)). In ITER, where the resistive time scale of the conducting wall is about an order of magnitude longer than the desired current quench time, the small variation of the poloidal flux at the plasma edge during the current quench is confirmed by 2D toroidally symmetric simulations with the JOREK code by Wang *et al.* (2024).

The above model is then applied to two of the scenarios studied in paper **D**. In addition to the magnetic perturbation and ion transport coefficients applied during the thermal quench we also explore here the effect of adding a hyperresistivity (see equation 5.19). This parameter is used to mimic the rapid current profile flattening and corresponding transport of poloidal flux during the magnetic reconnection event, and may therefore have a significant effect on the scrape-off runaway losses in some cases. The value of the hyperresistivity was chosen to recover a current spike with similar relative size as observed in experiments (see e.g. Gerasimov *et al.* (2020)).

The impact of the scrape-off losses is found to differ significantly between different cases. If the runaway current grows too large before a sizeable part of the flux surfaces are scraped off, the poloidal flux associated with the runaway current prevents the decay of the poloidal flux, thus preventing further scrape-off losses. In such cases, a long-lasting runaway plateau is formed, which is only scraped off after a relatively long time, when the assumption of a constant poloidal flux at the plasma edge is no longer valid. However, even a moderate decrease in the runaway generation allows for additional flux surfaces to be scraped off, further reducing the runaway generation and forming a positive feedback loop. As a result, in the best

performing case found in paper **D**, all flux surfaces are scraped off before a large runaway current is formed (although the runaway current is slightly larger than the desired upper limit of 150 kA mentioned in section 3.3). This result is however sensitive to the inclusion of hyperresistivity; if hyperresistivity is not included, the decay of the poloidal flux during the thermal quench is much slower, delaying the scrape-off process and allowing a macroscopic runaway plateau to form.

Despite the relatively high physics fidelity of papers **D** and **G**, a number of effects remain to be addressed. One such effect is the cross-field drift of the ablated pellet material, introduced in section 4.3.1. Accounting for this effect in a study similar to that of paper **D** would require a computationally efficient, preferably analytical, model for the total shift of the ablated material, as a function of the pellet and background plasma parameters. The development of such a model is the subject of paper **C**. Here we present a detailed derivation of the current balance equation governing the motion of an ablation plasmoid, along with an analytical solution assuming an approximate model of the plasmoid expansion along the field lines. The vertical plasmoid size, temperature and average charge are left as free parameters, which may be estimated based on previous measurements and simulations (see e.g. Müller *et al.* (2002); Matsuyama (2022)). One of the main novelties included is a statistical model for the field lines connecting the toroidally opposite sides of the plasmoid, and the corresponding Ohmic current flowing along those field lines, thus avoiding the need to numerically calculate the detailed paths of the field lines.

This model is then used to explore the extent of the drift in an ITER-relevant scenario, for a variety of pellet compositions. The results indicate that material ablated from a pure deuterium pellet is likely to drift a distance similar to the plasma minor radius, i.e. a substantial part of the material is likely to be completely ejected from the plasma. The evaluated drift distance was however found to be significantly reduced when adding a small amount of neon to the pellet, whose radiation reduces the temperature, and thus the excess pressure, inside the drifting plasmoid. This suggests that one should add a small amount of neon also to the first stage of the two-stage SPI scheme studied in paper **B** and paper **D**. The impact of such an addition of neon on the assimilation rate of the first injection stage is studied in paper **H**, as discussed below, assuming that the addition of neon does not result in a thermal quench during the first injection stage. It should however be emphasized that the possibility of injecting a slightly neon doped pellet in ITER without triggering a too early thermal quench requires further studies with appropriate 3D MHD models.

The plasmoid drift model of paper **C** is implemented in the DREAM code in paper **H**, where it is used to study the impact of plasmoid drifts on SPI mitigated disruptions in ASDEX Upgrade and ITER. The model is validated against line integrated density measurements from two ASDEX Upgrade injections, one with a pure deuterium pellet and one with a neon doping of 1.25% molar concentration. The pure deuterium pellet case was also validated against a post-injection measurement of the density profile based on Thomson scattering. The measured core line integrated density in this case was about 10% of what would be obtained if all injected material was uniformly assimilated in the plasma. For the neon doped pellet, the corresponding measure of the assimilation rate was about three times higher, experimentally confirming the larger drift losses expected for pure deuterium pellets.

For the pure deuterium injection, the model is found to match the experiment fairly well, for values of the free parameters within the range expected from previous measurements and simulations found in the literature. The results are however very sensitive to the vertical plasmoid width, which limits the predictive power of the model. For the neon doped pellet, the model moderately underpredicts the line integrated density regardless of the values of the free parameters of the drift model, given that the drifting material is assumed to travel freely out of the plasma and is then completely lost. The agreement was however improved if the drifting material was assumed to be mixed back into the plasma when the magnetic field becomes stochastic, indicating that the material drifting to the plasma edge may not be completely lost, at least not for doped pellets triggering a thermal quench.

The model is then applied to the best performing activated ITER case found in paper **D**. It is indicated that most of the material injected in the first injection stage will be lost, leading to an assimilation rate potentially as low as a few percent. The error margin is however large, due to the high sensitivity of the model to the assumed value of the vertical plasmoid width. Adding a small amount of neon to the first injection stage is found to increase its assimilation rate by up to an order of magnitude, given that the small addition of neon does not trigger a thermal quench during this injection stage. However, a low assimilation of the first injection stage leaves the plasma hotter as the second pellet arrives, increasing its ablation and assimilation rate. As a result, the effect of the drift losses on the runaway generation is moderate, at least when assuming a late and slow thermal quench. It should however be emphasized that the variation of runaway current may be amplified when including scrape-off losses, which were not included in this paper.

In addition to the plasmoid drift, the penetration and assimilation of the ablated material may also be affected by the pellet rocket force, making it desirable to have a computationally cheap model also for this effect, which could be implemented in integrated frameworks such as DREAM. Such a model is developed in paper **E**, for the rocket force stemming from gradients in the background plasma, and the contribution related to the plasmoid drift is included in paper **F**. The model is derived by adding a perturbative angularly dependent component to the treatment of the dynamics of the neutral cloud surrounding the pellet, building on the original derivation of the neutral gas shielding model by Parks & Turnbull (1978), as introduced in section 4.4. It is found that only the first spherical harmonic contributes to the rocket force, and a linear ODE system governing this correction is derived. The equation system is expressed in a normalized form allowing for a semi-analytical solution, and a numerical solution is presented along with a fit of the rocket force as a function of the variables remaining after normalization.

In paper **E** the model is then used to make estimated predictions of the rocket acceleration due to gradients in the background plasma, in ASDEX Upgrade scenarios similar to those studied experimentally by Müller *et al.* (2002). The predicted values are of the same order of magnitude as those measured in the experiment, but somewhat lower, with the discrepancy attributed to the contribution to the rocket force from the plasmoid drift. These calculations are extended in paper **F**, including the plasmoid shielding asymmetry and calculating the full pellet trajectory, showing good agreement with measurements by Szepesi *et al.* (2009). The model is also ap-

plied to ITER cases similar to those introduced in paper **D**. In low-confinement cases with a relatively modest core temperature ($\sim 5\,\mathrm{keV}$), the effect of the rocket force was found to be rather weak. On the other hand, in high-confinement cases with a core temperature $\sim 20\,\mathrm{keV}$, the penetration depth may decrease by a substantial order unity factor. These calculations were however performed assuming a static background plasma, disregarding the collective effect of shards paving the way for each other. A full assessment of the effect of the rocket force on SPIs, accounting for the above effect, would require implementing the rocket force model into a larger integrated model such as DREAM.

6.2 Current status and outlook

Disruptions remain a serious threat to the future of large scale, high current tokamaks of a similar scale to ITER. The results of paper **G** indicate that an acceptable disruption mitigation based on shattered pellet injection may be possible, but uncertainties and technical challenges remain. Disruptions may be somewhat less severe, although still challenging, in more compact future devices such as SPARC (paper **K**, paper **N**, Ekmark *et al.* (2025)), but even more severe in e.g. STEP due to the higher plasma current of 21 MA (paper **R**, paper **V**). Due to the severity of disruptions in reactor scale devices, disruption experiments at full scale need to be reduced as much as possible, thus requiring accurate modeling capabilities. The models need to self-consistently account for a large variety of physical phenomena at play, some of which are more easily captured than others by the models existing today.

The general qualitative trends of disruption mitigation performance as a function of the injected hydrogenic and impurity densities, in a reactor-scale high current device, may be considered to be reasonably well understood. The shape of the landscape of disruption mitigation performance shown in figure 2 of paper **A** may be traced to the atomic physics of the injected species. The radiated power as a function of temperature has three peaks (as shown in figure 6 of paper **A** and figure 6 of paper **B**); one peak in the $\sim 1 - 10\,\mathrm{eV}$ range, corresponding to line radiation from hydrogenic atoms; and the two peaks in the ranges $\sim 10 - 100\,\mathrm{eV}$ and $\sim 100 - 1000\,\mathrm{eV}$ related to line radiation from the outer and inner shell of the neon atoms or ions, respectively. During the current quench, the plasma will essentially approach an equilibrium between the Ohmic heating and the radiation losses corresponding to one of these peaks, giving rise to three distinct areas in the parameter space of disrupting mitigation performance.

In the areas corresponding to the peaks in the $\sim 1 - 10\,\mathrm{eV}$ and $\sim 10 - 100\,\mathrm{eV}$ ranges, the avalanche growth rate is enhanced by the relatively large abundance of bound electrons, leading to large runaway currents. The area corresponding to the peak in the $\sim 100 - 1000\,\mathrm{eV}$ range is characterized by too slow current quench times and insufficient radiative dissipation. A fourth area is formed in-between these three areas, where the optimal compromise between the above issues is found.

The above picture is complicated somewhat by the plasma being significantly opaque to some of the emitted radiation, as discussed in paper **B**. This effect moves the optimum towards higher deuterium densities, and would require a radiation transport model for a fully accurate treatment. Other possible complications in-

clude the ionization due to runaway electron impact (Garland *et al.*, 2020, 2022), potentially shifting and broadening the radiation peak at the lowest temperatures, thus quantitatively reshaping the mitigation performance landscape. Nevertheless, the range of the parameter space containing the optimum may be estimated with an anticipated reasonable accuracy. Updated mitigation performance landscapes for ITER, showing all disruption mitigation requirements summarized into a common cost function, are shown in paper **S** and **T**, accounting for the fact that the plasma is essentially opaque to Lyman radiation. Here it is indicated that the optimum is found at a deuterium density of $\lesssim 10^{22}\,\mathrm{m}^{-3}$ and a neon density of $\sim 10^{17}\,\mathrm{m}^{-3}$.

These numbers are consistent with semi-analytical calculations by McDevitt *et al.* (2023), using the ratio of the electric field and the effective critical electric field for runaway generation as a proxy for the runaway current. This study also highlights the fundamental connection between the atomic physics of the injected species and the features of the mitigation performance landscape. The optimum density values are also consistent with the results of paper **B**, **D**, **G** and **H**, where it is indicated that it is possible to achieve densities in the vicinity of the optimum reported in paper **T** with the SPI system planned for ITER.

The dynamics of small non-shattered pellets are fairly well understood from theory and experiments with fueling pellets (Pégourié, 2007). Recent modeling studies using a similar SPI model as the one used in DREAM have also been able to rather successfully reproduce SPI experiments in cases where plasmoid drifts are not expected to play a major role (Shiraki *et al.* (2020); Lvovskiy *et al.* (2023); paper **W**). The impact of plasmoid drifts and the pellet rocket force on the SPI dynamics however requires further investigation. Advanced numerical tools exist for calculating the plasmoid drift (Pégourié *et al.*, 2006; Samulyak *et al.*, 2021), but have not yet been used for full-disruption SPI simulations. Ad-hoc (Lvovskiy *et al.*, 2023) and interpretative Kong *et al.* (2024) models have been suggested which are able to reproduce experimental measurements, but are not able to self-consistently capture the drift dynamics. Paper **H** attempts to contribute to resolving this issue, but several important parameters, in particular the plasmoid size and temperature, remain undetermined by the model. Developing a semi-analytical model which self-consistently determines these parameters may provide important insights and significantly improve the modeling capability of pure hydrogenic SPIs.

The potential effect of the rocket force in reactor scale devices has only recently gained attention and remains rather unexplored. The trajectory of individual shards in the JET tokamak have been modeled with the rocket force taken into account, with results in general agreement with experiments Kong *et al.* (2024). The cumulative effect of many SPI shards in reactor scale devices however remains to be studied. Such a study could be performed by implementing the model presented in paper **E** into an integrated framework such as DREAM. Based on the preliminary calculations in paper **E** and **F**, the rocket force could potentially have a significant limiting effect on the assimilation of injected material in ITER.

The runaway generation rates presented in section 5.4.2 and 5.4.3 are rigorously derived from first principles, and have been used successfully in several interpretative comparisons with experiments (paper **J**, Linder *et al.* (2020), paper **P**). These studies were able to simultaneously reproduce both the experimentally measured current

decay and runaway plateau currents, with reasonable values of the free model parameters. Quantitative corrections, which may be significant in some cases, might be introduced by e.g. accounting for 3D effects or resolving additional momentum space dynamics kinetically (Stahl *et al.*, 2016; Embréus, Stahl & Fülöp, 2018; McDevitt & Tang, 2019), but are not expected to qualitatively alter the conclusions presented in this thesis. A part of the reason for this is the self-regulating mechanism where, at large runaway currents, an increase in the runaway generation is partly compensated by a decrease in the induced electric field, and vice versa.

Several simplifications and uncertainties however remain regarding the losses of runaway electrons, which may significantly affect the runaway plateau current at optimal injected quantities. The scrape-off model used in this thesis contains several simplifications which can only be resolved by 2D or 3D simulations with a dynamic flux surface geometry. Thus, while the results presented in paper **G** are promising, they must be verified with higher-fidelity models. Additional uncertainties are introduced by the prescribed evolution of the magnetic perturbations. In particular, the simulations presented in this thesis assume that no magnetic perturbations are present after the thermal quench. Such perturbations could be particularly strong in cases with a slightly incomplete thermal collapse, leading to the formation of thin hot sheets (Putvinski *et al.*, 1997*b*; Fehér *et al.*, 2011). The related sharp pressure gradients could potentially trigger major MHD instabilities, which may complete the thermal collapse and provide a major loss of runaways at the same time. On the other hand, the magnetic field is assumed to be fully stochastic during the thermal quench, without any remaining intact flux surfaces or magnetic islands giving rise to transport barriers, which may overestimate the runaway losses during this phase. These questions must however be treated with 3D MHD models.

A major issue with such calculations is the typically significant amount of computational resource required. A full scale 3D simulation of a thermal quench with the JOREK code, run on a large scale computing cluster, takes of the order of months Nardon *et al.* (2020*a*). Continuing the simulations into the current quench is even more demanding, and the MHD activity during the current quench therefore remains relatively unexplored, although several studies are under way. In contrast, the run-times for pure fluid simulations with DREAM and GO, following through both the thermal and current quench, are typically less than an hour. This highlights the benefit of combining knowledge gained with models of different complexity, to obtain sufficiently accurate results over a sufficiently large parameter space. Ideally, knowledge gained from models with high complexity could be used to develop reduced models which may be implemented in the computationally cheaper models.

Finally, this thesis is restricted to the study of pre-thermal quench injections, attempting to completely avoid the formation of a large runaway current. It may however be beneficial to combine this mitigation strategy with other methods, such as runaway mitigation coils or benign termination of a runaway beam by a secondary SPI, as described in section 3.5. In the latter case care must be taken that the pre-thermal quench injection is not so large that benign termination becomes inaccessible. Through a combination of novel mitigation strategies and the potential of runaway loss mechanisms yet to be explored, disruptions remain a formidable, but potentially solvable, problem for the future of fusion energy produced by tokamaks.

References

Aleynikov, P. & Breizman, B. N. 2015 "Theory of two threshold fields for relativistic runaway electrons". *Phys. Rev. Lett.* **114**, 155 001, DOI: 10.1103/PhysRevLett.114.155001, URL https://link.aps.org/doi/10.1103/PhysRevLett.114.155001

Aleynikov, P. & Breizman, B. N. 2017 "Generation of runaway electrons during the thermal quench in tokamaks". *Nuclear Fusion* **57** (4), 046 009, DOI: 10.1088/1741-4326/aa5895

Andersen, V. 1985 "Injection of solid deuterium pellets as a diagnostic tool". In "Europhysics Conference Abstracts", vol. 9F, Part 2, (648), Budapest: European Physical Society, URL http://libero.ipp.mpg.de/libero/PDF/EPS_12_Vol2_1985.pdf#page=645

Bandaru, V., Hoelzl, M., Reux, C., Ficker, O., Silburn, S., Lehnen, M., Eidietis, N., JOREK Team & JET Contributors 2021 "Magnetohydrodynamic simulations of runaway electron beam termination in JET". *Plasma Physics and Controlled Fusion* **63** (3), 035 024, DOI: 10.1088/1361-6587/abdbcf, URL https://dx.doi.org/10.1088/1361-6587/abdbcf

Bandaru, V., Hoelzl, M., Artola, F. & Lehnen, M. 2025 "Axisymmetric predictions for mitigated and vertically unstable disruptions in ITER with runaway electrons". *Journal of Plasma Physics* **91** (1), E27, DOI: 10.1017/S0022377824001661

Battey, A., Sheikh, U., Crisinel, F., Decker, J., Fasel, D. & Liu, Y. 2025 "Design of the TCV runaway electron mitigation coil". URL https://ft.nephy.chalmers.se/do/downloadconfpresentation.php?id=199. Presented at the Joint Runaway Electron Modelling (REM) and WPTE RT03 Analysis meeting

Baylor, L., Jernigan, T., Parks, P., Antar, G., Brooks, N., Combs, S., Fehling, D., Foust, C., Houlberg, W. & Schmidt, G. 2007 "Comparison of deuterium pellet injection from different locations on the DIII-D tokamak". *Nuclear Fusion* **47** (11), 1598–1606, DOI: 10.1088/0029-5515/47/11/023, URL https://doi.org/10.1088/0029-5515/47/11/023

Baylor, L., Combs, S., Foust, C., Jernigan, T., Meitner, S., Parks, P., Caughman, J., Fehling, D., Maruyama, S., Qualls, A., Rasmussen, D. & Thomas, C. 2009 "Pellet fuelling, ELM pacing and disruption mitigation technology development for ITER". *Nuclear Fusion* **49** (8), 085 013, DOI: 10.1088/0029-5515/49/8/085013, URL https://doi.org/10.1088/0029-5515/49/8/085013

Baylor, L., Meitner, S., Gebhart, T., Caughman, J., Herfindal, J., Shiraki, D. & Youchison, D. 2019 "Shattered pellet injection technology design and characterization for disruption mitigation experiments". *Nuclear Fusion* **59** (6), 066 008, DOI: 10.1088/1741-4326/ab136c, URL https://dx.doi.org/10.1088/1741-4326/ab136c

Baylor, L., Meitner, S., Gebhart, T., Caughman, J., Shiraki, D., Wilson, J., Craven, D., Fortune, M., Silburn, S., Muir, A., Peacock, A., Park, S., Kim, K., Kim, J., Lee, K., Ellwood, G., Jachmich, S., Kruezi, U., Lehnen, M. & JET Contributors 2021 "Design and performance of shattered pellet injection systems for JET and KSTAR disruption mitigation research in support of ITER". *Nuclear Fusion* **61** (10), 106 001, DOI: 10.1088/1741-4326/ac1bc3, URL https://dx.doi.org/10.1088/1741-4326/ac1bc3

Beliaev, S. & Budker, G. 1956 "The relativistic kinetic equation". In "Soviet physics doklady", vol. 1, (218)

Boozer, A. H. 2011 "Two beneficial non-axisymmetric perturbations to tokamaks". *Plasma Physics and Controlled Fusion* **53** (8), 084 002, DOI: 10.1088/0741-3335/53/8/084002, URL https://dx.doi.org/10.1088/0741-3335/53/8/084002

Boozer, A. H. 2018 "Pivotal issues on relativistic electrons in ITER". *Nuclear Fusion* **58** (3), 036 006, DOI: 10.1088/1741-4326/aaa1db, URL https://dx.doi.org/10.1088/1741-4326/aaa1db

Boozer, A. H. 2021 "The interaction of the iter first wall with magnetic perturbations". *Nuclear Fusion* **61** (4), 046 025, DOI: 10.1088/1741-4326/abe226, URL https://doi.org/10.1088/1741-4326/abe226

Bosviel, N., Parks, P. & Samulyak, R. 2021 "Near-field models and simulations of pellet ablation in tokamaks". *Physics of Plasmas* **28** (1), 012 506, ISSN 1070-664X, DOI: 10.1063/5.0029721, URL https://doi.org/10.1063/5.0029721. https://pubs.aip.org/aip/pop/article-pdf/doi/10.1063/5.0029721/15734147/012506_1_online.pdf

Breizman, B. N., Aleynikov, P., Hollmann, E. M. & Lehnen, M. 2019 "Physics of runaway electrons in tokamaks". *Nuclear Fusion* **59** (8), 083 001, DOI: 10.1088/1741-4326/ab1822

Cabal, H., Lechon, Y., Bustreo, C., Gracceva, F., Biberacher, M., Ward, D., Dongiovanni, D. & Grohnheit, P. E. 2017 "Fusion power in a future low carbon global electricity system". *Energy Strategy Reviews* **15**, DOI: 10.1016/j.esr.2016.11.002

Chen, F. 1974 Introduction to Plasma Physics and Controlled Fusion. 1st edn., New York, NY, USA: Springer International Publishing

Chen, F. 2011 An indispensable truth: how fusion power can save the planet. New York, NY, USA: Springer Science & Business Media

Combs, S. K. & Baylor, L. R. 2018 "Pellet-injector technology - brief history and key developments in the last 25 years". *Fusion Science and Technology* **73** (4), 493–518, DOI: 10.1080/15361055.2017.1421367, URL https://doi.org/10.1080/15361055.2017.1421367. https://doi.org/10.1080/15361055.2017.1421367

Commaux, N., Baylor, L., Jernigan, T., Hollmann, E., Parks, P., Humphreys, D., Wesley, J. & Yu, J. 2010*a* "Demonstration of rapid shutdown using large shattered deuterium pellet injection in DIII-D". *Nuclear Fusion* **50** (11), 112 001, DOI: 10.1088/0029-5515/50/11/112001, URL https://dx.doi.org/10.1088/0029-5515/50/11/112001

Commaux, N., Pégourié, B., Baylor, L., Köchl, F., Parks, P., Jernigan, T., Géraud, A. & Nehme, H. 2010*b* "Influence of the low order rational q surfaces on the pellet deposition profile". *Nuclear Fusion* **50** (2), 025 011, DOI: 10.1088/0029-5515/50/2/025011, URL https://doi.org/10.1088/0029-5515/50/2/025011

Commaux, N., Shiraki, D., Baylor, L., Hollmann, E., Eidietis, N., Lasnier, C., Moyer, R., Jernigan, T., Meitner, S., Combs, S. & Foust, C. 2016 "First demonstration of rapid shutdown using neon shattered pellet injection for thermal quench mitigation on DIII-D". *Nuclear Fusion* **56** (4), 046 007, DOI: 10.1088/0029-5515/56/4/046007, URL https://dx.doi.org/10.1088/0029-5515/56/4/046007

Connor, J. & Hastie, R. 1975 "Relativistic limitations on runaway electrons". *Nuclear Fusion* **15** (3), 415

Decker, J., Hirvijoki, E., Embréus, O., Peysson, Y., Stahl, A., Pusztai, I. & Fülöp, T. 2016 "Numerical characterization of bump formation in the runaway electron tail". *Plasma Physics and Controlled Fusion* **58** (2), 025 016, DOI: 10.1088/0741-3335/58/2/025016

Dibon, M., de Marne, P., Papp, G., Vinyar, I., Lukin, A., Jachmich, S., Kruezi, U., Muir, A., Rohde, V., Lehnen, M., Heinrich, P., Peherstorfer, T., Podymskii, D. & the ASDEX Upgrade Team 2023 "Design of the shattered pellet injection system for ASDEX Upgrade". *Review of Scientific Instruments* **94** (4), 043 504, ISSN 0034-6748, DOI: 10.1063/5.0141799, URL https://doi.org/10.1063/5.0141799. https://pubs.aip.org/aip/rsi/article-pdf/doi/10.1063/5.0141799/16833711/043504_1_5.0141799.pdf

Dreicer, H. 1959 "Electron and ion runaway in a fully ionized gas I". *Physical Review* **115** (2), 238, DOI: 10.1103/PhysRev.115.238

Durst, R., Rowan, W., Austin, M., Collins, R., Gandy, R., Phillips, P. & Richards, B. 1990 "Experimental observations of the dynamics of pellet ablation on the Texas Experimental Tokamak (TEXT)". *Nuclear Fusion* **30** (1), 3, DOI: 10.1088/0029-5515/30/1/001, URL https://dx.doi.org/10.1088/0029-5515/30/1/001

Ekmark, I., Hoppe, M., Tinguely, R., Sweeney, R., Fülöp, T. & Pusztai, I. 2025 "Runaway electron generation in disruptions mitigated by deuterium and noble gas injection in SPARC". *Journal of Plasma Physics* **91** (3), E82, doi: 10.1017/S0022377825000455

Embréus, O., Stahl, A. & Fülöp, T. 2016 "Effect of bremsstrahlung radiation emission on fast electrons in plasmas". *New Journal of Physics* **18** (9), 093 023

Embréus, O., Stahl, A. & Fülöp, T. 2018 "On the relativistic large-angle electron collision operator for runaway avalanches in plasmas". *Journal of Plasma Physics* **84** (1), 905840 102, doi: 10.1017/S002237781700099X

Fehér, T., Smith, H. M., Fülöp, T. & Gál, K. 2011 "Simulation of runaway electron generation during plasma shutdown by impurity injection in ITER". *Plasma Physics and Controlled Fusion* **53** (3), 035 014, doi: 10.1088/0741-3335/53/3/035014, URL https://dx.doi.org/10.1088/0741-3335/53/3/035014

Fontanilla, A. K. & Breizman, B. N. 2019 "Heating and ablation of high-Z cryogenic pellets in high temperature plasmas". *Nuclear Fusion* **59** (9), 096 033, doi: 10.1088/1741-4326/ab2bd6, URL https://dx.doi.org/10.1088/1741-4326/ab2bd6

Freidberg, J. P. 2008 Plasma physics and fusion energy. 1st edn., Cambridge, UK: Cambridge University Press

Garland, N. A., Chung, H.-K., Fontes, C. J., Zammit, M. C., Colgan, J., Elder, T., McDevitt, C. J., Wildey, T. M. & Tang, X.-Z. 2020 "Impact of a minority relativistic electron tail interacting with a thermal plasma containing high-atomic-number impurities". *Physics of Plasmas* **27** (4), 040 702, ISSN 1070-664X, doi: 10.1063/5.0003638, URL https://doi.org/10.1063/5.0003638. https://pubs.aip.org/aip/pop/article-pdf/doi/10.1063/5.0003638/15923353/040702_1_online.pdf

Garland, N. A., Chung, H.-K., Zammit, M. C., McDevitt, C. J., Colgan, J., Fontes, C. J. & Tang, X.-Z. 2022 "Understanding how minority relativistic electron populations may dominate charge state balance and radiative cooling of a post-thermal quench tokamak plasma". *Physics of Plasmas* **29** (1), 012 504, ISSN 1070-664X, doi: 10.1063/5.0071996, URL https://doi.org/10.1063/5.0071996. https://pubs.aip.org/aip/pop/article-pdf/doi/10.1063/5.0071996/16625462/012504_1_online.pdf

Gebhart, T. E., Baylor, L. R. & Meitner, S. J. 2020 "Experimental pellet shatter thresholds and analysis of shatter tube ejecta for disruption mitigation cryogenic pellets". *IEEE Transactions on Plasma Science* **48** (6), 1598–1605, doi: 10.1109/TPS.2019.2957968

Gerasimov, S., Abreu, P., Artaserse, G., Baruzzo, M., Buratti, P., Carvalho, I., Coffey, I., De La Luna, E., Hender, T., Henriques, R., Felton, R., Jachmich, S., Kruezi, U., Lomas, P., McCullen, P., Maslov, M., Matveeva, E., Moradi, S., Piron, L., Rimini, F., Schippers, W., Stuart, C., Szepesi, G., Tsalas, M., Valcarcel, D., Zakharov, L., & JET Contributors 2020 "Overview of disruptions with JET-ILW". *Nuclear Fusion* **60** (6), 066 028, doi: 10.1088/1741-4326/ab87b0, URL https://dx.doi.org/10.1088/1741-4326/ab87b0

Gruber, O., Lackner, K., Pautasso, G., Seidel, U. & Streibl, B. 1993 "Vertical displacement events and halo currents". *Plasma Physics and Controlled Fusion* **35** (SB), B191, doi: 10.1088/0741-3335/35/SB/015, URL https://dx.doi.org/10.1088/0741-3335/35/SB/015

Hauff, T. & Jenko, F. 2009 "Runaway electron transport via tokamak microturbulence". *Physics of Plasmas* **16** (10), 102 308, ISSN 1070-664X, doi: 10.1063/1.3243494, URL https://doi.org/10.1063/1.3243494. https://pubs.aip.org/aip/pop/article-pdf/doi/10.1063/1.3243494/14058921/102308_1_online.pdf

Heinrich, P., Papp, G., de Marné, P., Dibon, M., Jachmich, S., Lehnen, M., Peherstorfer, T. & Vinyar, I. 2024 "Recipes for pellet generation and launching in the ASDEX Upgrade SPI". *Fusion Engineering and Design* **206**, 114 576, ISSN 0920-3796, doi: https://doi.org/10.1016/j.fusengdes.2024.114576, URL https://www.sciencedirect.com/science/article/pii/S0920379624004289

Heinrich, P., Papp, G., Jachmich, S., Artola, J., Bernert, M., de Marné, P., Dibon,

M., Dux, R., Eberl, T., Hobirk, J., Lehnen, M., Peherstorfer, T., Schwarz, N., Sheikh, U., Sieglin, B., Svoboda, J., the ASDEX Upgrade Team & the EUROfusion Tokamak Exploitation Team 2025 "Radiated energy fraction of SPI-induced disruptions at ASDEX Upgrade". *Nuclear Fusion* **65** (5), 056 036, doi: 10.1088/1741-4326/adcbc0, URL https://dx.doi.org/10.1088/1741-4326/adcbc0

Helander, P. & Sigmar, D. 2005 Collisional Transport in Magnetized Plasmas. Cambridge, UK: Cambridge University Press

Helander, P., Smith, H., Fülöp, T. & Eriksson, L.-G. 2004 "Electron kinetics in a cooling plasma". *Physics of Plasmas* **11** (12), 5704, doi: 10.1063/1.1812759

Hender, T., Wesley, J., Bialek, J., Bondeson, A., Boozer, A., Buttery, R., Garofalo, A., Goodman, T., Granetz, R., Gribov, Y., Gruber, O., Gryaznevich, M., Giruzzi, G., Günter, S., Hayashi, N., Helander, P., Hegna, C., Howell, D., Humphreys, D., Huysmans, G., Hyatt, A., Isayama, A., Jardin, S., Kawano, Y., Kellman, A., Kessel, C., Koslowski, H., Haye, R. L., Lazzaro, E., Liu, Y., Lukash, V., Manickam, J., Medvedev, S., Mertens, V., Mirnov, S., Nakamura, Y., Navratil, G., Okabayashi, M., Ozeki, T., Paccagnella, R., Pautasso, G., Porcelli, F., Pustovitov, V., Riccardo, V., Sato, M., Sauter, O., Schaffer, M., Shimada, M., Sonato, P., Strait, E., Sugihara, M., Takechi, M., Turnbull, A., Westerhof, E., Whyte, D., Yoshino, R., Zohm, H. & the ITPA MHD, Disruption and Magnetic Control Topical Group 2007 "Chapter 3: MHD stability, operational limits and disruptions". *Nuclear Fusion* **47** (6), 128, doi: 10.1088/0029-5515/47/6/S03

Herfindal, J., Shiraki, D., Baylor, L., Eidietis, N., Hollmann, E., Lasnier, C. & Moyer, R. 2019 "Injection of multiple shattered pellets for disruption mitigation in DIII-D". *Nuclear Fusion* **59** (10), 106 034, doi: 10.1088/1741-4326/ab3693, URL https://dx.doi.org/10.1088/1741-4326/ab3693

Hesslow, L., Embréus, O., Hoppe, M., DuBois, T., Papp, G., Rahm, M. & Fülöp, T. 2018*a* "Generalized collision operator for fast electrons interacting with partially ionized impurities". *Journal of Plasma Physics* **84** (6), 905840 605, doi: 10.1017/S0022377818001113

Hesslow, L., Embréus, O., Wilkie, G. J., Papp, G. & Fülöp, T. 2018*b* "Effect of partially ionized impurities and radiation on the effective critical electric field for runaway generation". *Plasma Physics and Controlled Fusion* **60** (7), 074 010, doi: 10.1088/1361-6587/aac33e

Hirvijoki, E., Pusztai, I., Decker, J., Embréus, O., Stahl, A. & Fülöp, T. 2015 "Radiation reaction induced non-monotonic features in runaway electron distributions". *Journal of Plasma Physics* **81**, 475810 502, doi: 10.1017/S0022377815000513/

Hollmann, E. M., Aleynikov, P. B., Fülöp, T., Humphreys, D. A., Izzo, V. A., Lehnen, M., Lukash, V. E., Papp, G., Pautasso, G., Saint-Laurent, F. & Snipes, J. A. 2015 "Status of research toward the ITER disruption mitigation system". *Physics of Plasmas* **22** (2), 021 802, ISSN 1070-664X, doi: 10.1063/1.4901251, URL https://doi.org/10.1063/1.4901251. https://pubs.aip.org/aip/pop/article-pdf/doi/10.1063/1.4901251/16137172/021802_1_online.pdf

Hoppe, M., Embreus, O. & Fülöp, T. 2021 "DREAM: a fluid-kinetic framework for tokamak disruption runaway electron simulations". 2103.16457

Hoppe, M., Decker, J., Sheikh, U., Coda, S., Colandrea, C., Duval, B., Ficker, O., Halldestam, P., Jachmich, S., Lehnen, M., Reimerdes, H., Paz-Soldan, C., Pedrini, M., Reux, C., Simons, L., Vincent, B., Wijkamp, T., Zurita, M., the TCV Team & the EUROfusion Tokamak Exploitation Team 2025 "An upper pressure limit for low-Z benign termination of runaway electron beams in TCV". *Plasma Physics and Controlled Fusion* **67** (4), 045 015, doi: 10.1088/1361-6587/adbcd5, URL https://dx.doi.org/10.1088/1361-6587/adbcd5

Hu, D., Nardon, E., Lehnen, M., Huijsmans, G., van Vugt, D. C. & JET Contributors 2018 "3D non-linear MHD simulation of the MHD response and density increase as a result of shattered pellet injection". *Nuclear Fusion* **58** (12), 126 025, doi: 10.1088/1741-4326/aae614

Hu, D., Nardon, E., Hoelzl, M., Wieschollek, F., Lehnen, M., Huijsmans, G., van Vugt, D. C., Kim, S.-H., JET Contributors & the JOREK TEam 2021 "Radiation

asymmetry and MHD destabilization during the thermal quench after impurity shattered pellet injection". *Nuclear Fusion* **61** (2), 026 015, DOI: 10.1088/1741-4326/abcbcb, URL https://doi.org/10.1088/1741-4326/abcbcb

ITER ORGANIZATION http://www.iter.org

IZZO, V., HOLLMANN, E., JAMES, A., YU, J., HUMPHREYS, D., LAO, L., PARKS, P., SIECK, P., WESLEY, J., GRANETZ, R., OLYNYK, G. & WHYTE, D. 2011 "Runaway electron confinement modelling for rapid shutdown scenarios in DIII-D, Alcator C-Mod and ITER". *Nuclear Fusion* **51** (6), 063 032, DOI: 10.1088/0029-5515/51/6/063032, URL https://dx.doi.org/10.1088/0029-5515/51/6/063032

IZZO, V., PUSZTAI, I., SÄRKIMÄKI, K., SUNDSTRÖM, A., GARNIER, D., WEISBERG, D., TINGUELY, R., PAZ-SOLDAN, C., GRANETZ, R. & SWEENEY, R. 2022 "Runaway electron deconfinement in SPARC and DIII-D by a passive 3D coil". *Nuclear Fusion* **62** (9), 096 029, DOI: 10.1088/1741-4326/ac83d8, URL https://dx.doi.org/10.1088/1741-4326/ac83d8

JACHMICH, S., KRUEZI, U., LEHNEN, M., BARUZZO, M., BAYLOR, L., CARNEVALE, D., CRAVEN, D., EIDIETIS, N., FICKER, O., GEBHART, T., GERASIMOV, S., HERFINDAL, J., HOLLMANN, E., HUBER, A., LOMAS, P., LOVELL, J., MANZANARES, A., MASLOV, M., MLYNAR, J., PAUTASSO, G., PAZ-SOLDAN, C., PEACOCK, A., PIRON, L., PLYUSNIN, V., REINKE, M., REUX, C., RIMINI, F., SHEIKH, U., SHIRAKI, D., SILBURN, S., SWEENEY, R., WILSON, J., CARVALHO, P. & JET CONTRIBUTORS 2022 "Shattered pellet injection experiments at JET in support of the ITER disruption mitigation system design". *Nuclear Fusion* **62** (2), 026 012, ISSN 0029-5515, 1741-4326, DOI: 10.1088/1741-4326/ac3c86, URL https://iopscience.iop.org/article/10.1088/1741-4326/ac3c86

JONES, E. 1978 "Self-propelling pellets for fusion-reactor refueling". *Lettere al Nuovo Cimento (1971-1985)* **23** (5), 198–200, ISSN 1827-613X, DOI: 10.1007/BF02856274, URL https://doi.org/10.1007/BF02856274

KARNEY, C. F. 1986 "Fokker-Planck and quasilinear codes". *Computer Physics Reports* **4** (3), 183, ISSN 0167-7977, DOI: 10.1016/0167-7977(86)90029-8

KAUFMANN, M., LACKNER, K., LENGYEL, L. & SCHNEIDER, W. 1986 "Plasma shielding of hydrogen pellets". *Nuclear Fusion* **26** (2), 171, DOI: 10.1088/0029-5515/26/2/005, URL https://dx.doi.org/10.1088/0029-5515/26/2/005

KIM, S., CASPER, T. & SNIPES, J. 2018 "Investigation of key parameters for the development of reliable ITER baseline operation scenarios using CORSICA". *Nuclear Fusion* **58** (5), 056 013, DOI: 10.1088/1741-4326/aab034, URL https://dx.doi.org/10.1088/1741-4326/aab034

KIRAMOV, D. I. & BREIZMAN, B. N. 2017 "Model of vertical plasma motion during the current quench". *Physics of Plasmas* **24** (10), 100 702, ISSN 1070-664X, DOI: 10.1063/1.4993071, URL https://doi.org/10.1063/1.4993071. https://pubs.aip.org/aip/pop/article-pdf/doi/10.1063/1.4993071/14890403/100702_1_online.pdf

KOCH, H. W. & MOTZ, J. W. 1959 "Bremsstrahlung cross-section formulas and related data". *Rev. Mod. Phys.* **31**, 920, DOI: 10.1103/RevModPhys.31.920

KONG, M., NARDON, E., HOELZL, M., BONFIGLIO, D., HU, D., LEE, S.-J., SAMULYAK, R., SHEIKH, U., SILBURN, S., ARTOLA, F., BOBOC, A., BODNER, G., CARVALHO, P., DELABIE, E., FONTDECABA, J., GERASIMOV, S., HENDER, T., JACHMICH, S., KOS, D., LAWSON, K., PAMELA, S., SOMMARIVA, C., STANCAR, Z., STEIN-LUBRANO, B., SUN, H., SWEENEY, R., SZEPESI, G., THE JOREK TEAM & JET CONTRIBUTORS 2024 "Interpretative 3D MHD modelling of deuterium SPI into a JET H-mode plasma". *Nuclear Fusion* **64** (6), 066 004, ISSN 0029-5515, 1741-4326, DOI: 10.1088/1741-4326/ad3b1c, URL https://iopscience.iop.org/article/10.1088/1741-4326/ad3b1c

LANG, P. T., BÜCHL, K., KAUFMANN, M., LANG, R. S., MERTENS, V., MÜLLER, H. W. & NEUHAUSER, J. 1997 "High-efficiency plasma refuelling by pellet injection from the magnetic high-field side into ASDEX Upgrade". *Phys. Rev. Lett.* **79**, 1487–1490, DOI: 10.1103/PhysRevLett.79.1487, URL https://link.aps.org/doi/10.1103/PhysRevLett.79.1487

LEHNEN, M. & THE ITER DMS TASK FORCE 2021 "The ITER disruption mitigation system - design progress and design validation". URL https://tsdw.pppl.gov/Talks/2021/Lehnen.

pdf. Presented at Theory and Simulation of Disruptions Workshop, PPPL

Lehnen, M., Bozhenkov, S. A., Abdullaev, S. S. & Jakubowski, M. W. 2008 "Suppression of runaway electrons by resonant magnetic perturbations in TEXTOR disruptions". *Phys. Rev. Lett.* **100**, 255 003, DOI: 10.1103/PhysRevLett.100.255003, URL https://link.aps.org/doi/10.1103/PhysRevLett.100.255003

Lehnen, M., Arnoux, G., Hartmann, N., Brezinsek, S., Devaux, S., Huber, A., Jachmich, S., Kruezi, U., Matthews, G., Reux, C., Riccardo, V., Sieglin, B., Stamp, M. & de Vries, P. 2013 "Disruption heat loads and their mitigation in JET with the ITER-like wall". *Journal of Nuclear Materials* **438**, S102–S107, ISSN 0022-3115, DOI: https://doi.org/10.1016/j.jnucmat.2013.01.016, URL https://www.sciencedirect.com/science/article/pii/S002231151300024X. Proceedings of the 20th International Conference on Plasma-Surface Interactions in Controlled Fusion Devices

Lehnen, M., Jachmich, S., Kruezi, U. & the ITER DMS task force 2020 "The ITER disruption mitigation strategy". https://conferences.iaea.org/event/217/contributions/17867/. Presented by M. Lehnen at the IAEA Technical Meeting on Plasma Disruption and their Mitigation

Lengyel, L., Rozhanskij, V. & Veselova, L. 1996 "Electrostatic shielding of vaporizing surfaces exposed to hot plasmas". *Nuclear Fusion* **36** (12), 1679, DOI: 10.1088/0029-5515/36/12/I08, URL https://dx.doi.org/10.1088/0029-5515/36/12/I08

Lengyel, L., Büchl, K., Pautasso, G., Ledl, L., Ushakov, A., Kalvin, S. & Veres, G. 1999 "Modelling of impurity pellet ablation in ASDEX Upgrade (neon) and Wendelstein W7-AS (carbon) by means of a radiative (`killer') pellet code". *Nuclear Fusion* **39** (6), 791, DOI: 10.1088/0029-5515/39/6/307

Linder, O., Fable, E., Jenko, F., Papp, G. & Pautasso, G. 2020 "Self-consistent modeling of runaway electron generation in massive gas injection scenarios in ASDEX Upgrade". *Nuclear Fusion* **60** (9), 096 031, DOI: 10.1088/1741-4326/ab9dcf

Loarte, A., Riccardo, V., Martin-Solís, J., Paley, J., Huber, A., Lehnen, M. & JET EFDA Contributors 2011 "Magnetic energy flows during the current quench and termination of disruptions with runaway current plateau formation in JET and implications for ITER". *Nuclear Fusion* **51** (7), 073 004, DOI: 10.1088/0029-5515/51/7/073004, URL https://dx.doi.org/10.1088/0029-5515/51/7/073004

Lvovskiy, A., Matsuyama, A., OGorman, T., Shiraki, D., Herfindal, J., Hollmann, E., Marini, C., Boivin, R., Eidietis, N. & Lehnen, M. 2023 "Density and temperature profiles after low-Z and high-Z shattered pellet injections on DIII-D". *Nuclear Fusion* **64** (1), 016 002, DOI: 10.1088/1741-4326/ad0905, URL https://dx.doi.org/10.1088/1741-4326/ad0905

MacAulay, A. 1994 "Geometrical, kinetic and atomic physics effects in a two dimensional time dependent fluid simulation of ablating fuel pellets". *Nuclear Fusion* **34** (1), 43, DOI: 10.1088/0029-5515/34/1/i03

Martín-Solís, J., Loarte, A. & Lehnen, M. 2017 "Formation and termination of runaway beams in ITER disruptions". *Nuclear Fusion* **57** (6), 066 025, DOI: 10.1088/1741-4326/aa6939, URL https://dx.doi.org/10.1088/1741-4326/aa6939

Martín-Solís, J., Mier, J., Lehnen, M. & Loarte, A. 2022 "Formation and termination of runaway beams during vertical displacement events in tokamak disruptions". *Nuclear Fusion* **62** (7), 076 013, DOI: 10.1088/1741-4326/ac637b, URL https://dx.doi.org/10.1088/1741-4326/ac637b

Matsuyama, A. 2022 "Neutral gas and plasma shielding (NGPS) model and cross-field motion of ablated material for hydrogen-neon mixed pellet injection". *Physics of Plasmas* **29** (4), 042 501, DOI: 10.1063/5.0084586, URL https://doi.org/10.1063/5.0084586. https://doi.org/10.1063/5.0084586

Matsuyama, A., Nardon, E., Honda, M. & Lehnen, M. 2020 "ITER SPI modelling for runaway electron avoidance". https://ft.nephy.chalmers.se/?p=abstract&id=10. Presented at the 8th Runaway Electron Modelling (REM) meeting

McDevitt, C. J. & Tang, X.-Z. 2019 "Runaway electron generation in axisymmetric tokamak geometry". *Europhysics Letters* **127** (4), 45 001, DOI: 10.1209/0295-5075/127/45001, URL https://dx.doi.org/10.1209/0295-5075/127/45001

McDevitt, C. J. & Tang, X.-Z. 2023 "Runaway electron current reconstitution after a nonaxisymmetric magnetohydrodynamic flush". *Phys. Rev. E* **108**, L043 201, DOI: 10.1103/PhysRevE.108.L043201, URL https://link.aps.org/doi/10.1103/PhysRevE.108.L043201

McDevitt, C. J., Tang, X.-Z., Fontes, C. J., Sharma, P. & Chung, H.-K. 2023 "The constraint of plasma power balance on runaway avoidance". *Nuclear Fusion* **63** (2), 024 001, DOI: 10.1088/1741-4326/acae38, URL https://dx.doi.org/10.1088/1741-4326/acae38

Meitner, S., Baylor, L. R., Commaux, N., Shiraki, D., Combs, S., Bjorholm, T., Ha, T. & McGinnis, W. 2017 "Design and commissioning of a three-barrel shattered pellet injector for DIII-D disruption mitigation studies". *Fusion Science and Technology* **72** (3), 318–323, DOI: 10.1080/15361055.2017.1333854, URL https://doi.org/10.1080/15361055.2017.1333854. https://doi.org/10.1080/15361055.2017.1333854

Milora, S., Houlberg, W., Lengyel, L. & Mertens, V. 1995 "Pellet fuelling". *Nuclear Fusion* **35** (6), 657, DOI: 10.1088/0029-5515/35/6/i04

Mlynar, J., Ficker, O., Macusova, E., Markovic, T., Naydenkova, D., Papp, G., Urban, J., Vlainic, M., Vondracek, P., Weinzettl, V., Bogar, O., Bren, D., Carnevale, D., Casolari, A., Cerovsky, J., Farnik, M., Gobbin, M., Gospodarczyk, M., Hron, M., Kulhanek, P., Havlicek, J., Havranek, A., Imrisek, M., Jakubowski, M., Lamas, N., Linhart, V., Malinowski, K., Marcisovsky, M., Matveeva, E., Panek, R., Plyusnin, V. V., Rabinski, M., Svoboda, V., Svihra, P., Varju, J., Zebrowski, J., the COMPASS Team & the EUROfusion MST1 Team 2018 "Runaway electron experiments at compass in support of the EUROfusion ITER physics research". *Plasma Physics and Controlled Fusion* **61** (1), 014 010, DOI: 10.1088/1361-6587/aae04a, URL https://doi.org/10.1088/1361-6587/aae04a

Morozov, D., Gervids, V., Senichenkov, I., Veselova, I., Rozhansky, V. & Schneider, R. 2004 "Ionization–recombination processes and ablation cloud structure for a carbon pellet". *Nuclear Fusion* **44** (2), 252, DOI: 10.1088/0029-5515/44/2/005

Mott, N. & Linfoot, E. 1943 "A theory of fragmentation". Tech. Rep. AC3348, United Kingdom Ministry of Supply

Mott, N. & Linfoot, E. 2006 A Theory of Fragmentation, (207). Berlin, Heidelberg: Springer Berlin Heidelberg, ISBN 978-3-540-27145-1, DOI: 10.1007/978-3-540-27145-1_9

Müller, H., Dux, R., Kaufmann, M., Lang, P., Lorenz, A., Maraschek, M., Mertens, V., Neuhauser, J. & the ASDEX Upgrade Team 2002 "High beta plasmoid formation, drift and striations during pellet ablation in ASDEX Upgrade". *Nuclear Fusion* **42** (3), 301, DOI: 10.1088/0029-5515/42/3/311, URL https://dx.doi.org/10.1088/0029-5515/42/3/311

Nardon, E., Artola, J., Sommariva, C., Hoelzl, M., Hu, D. & Huijsmans, G. 2020*a* "JOREK simulations of MGI-triggered disruptions in JET". https://ft.nephy.chalmers.se/?p=abstract&id=11. Presented at the 8th Runaway Electron Modelling (REM) meeting

Nardon, E., Hu, D., Hoelzl, M., Bonfiglio, D. & the JOREK Team 2020*b* "Fast plasma dilution in ITER with pure deuterium shattered pellet injection". *Nuclear Fusion* **60** (12), 126 040, DOI: 10.1088/1741-4326/abb749

Nardon, E., Matsuyama, A. & Lehnen, M. 2020 "On the possible injection schemes with the ITER SPI system". https://conferences.iaea.org/event/217/contributions/16702/. Presented at the IAEA Technical Meeting on Plasma Disruption and their Mitigation

Papp, G., Drevlak, M., Fülöp, T. & Helander, P. 2011*a* "Runaway electron drift orbits in magnetostatic perturbed fields". *Nuclear Fusion* **51** (4), 043 004, DOI: 10.1088/0029-5515/51/4/043004, URL https://doi.org/10.1088/0029-5515/51/4/043004

Papp, G., Drevlak, M., Fülöp, T., Helander, P. & Pokol, G. I. 2011*b* "Runaway electron losses caused by resonant magnetic perturbations in ITER". *Plasma Physics and Controlled*

Fusion **53** (9), 095 004, DOI: 10.1088/0741-3335/53/9/095004, URL https://doi.org/10.1088/0741-3335/53/9/095004

Papp, G., Pautasso, G., Decker, J., Gobbin, M., Mccarthy, P., Blanchard, P., Carnevale, D., Choi, D., Coda, S., Duval, B., Dux, R., Erdös, B., Esposito, B., Ficker, O., Fischer, R., Fuchs, C., Galperti, C., Giannone, L., Gude, A., Labit, B., Lackner, K., Lunt, T., Marelli, L., Martin, P., Mlynek, A., Maraschek, M., Marmillod, P., Nocente, M., Peysson, Y., Piovesan, P., Plyusnin, V., Pokol, G., Poloskei, P., Potzel, S., Reux, C., Saint-Laurent, F., Sauter, O., Sieglin, B., Sheikh, U., Sommariva, C., Suttrop, W., Tardini, G., Testa, D., Treutterer, W., Valisa, M., the ASDEX Upgrade Team, the TCV Team & the Eurofusion MST1 Team 2016 "Runaway electron generation and mitigation on the european medium sized tokamaks ASDEX Upgrade and TCV". In "Proceedings of the 2016 IAEA Fusion Energy Conference", URL https://nucleus.iaea.org/sites/fusionportal/Shared%20Documents/FEC%202016/fec2016-preprints/preprint0502.pdf

Park, S., Lee, K., Baylor, L. R., Meitner, S. J., Lee, H., Song, J., Gebhart, T. E., Yun, S., Kim, J., Kim, K., Park, K. & Yoon, S. 2020 "Deployment of multiple shattered pellet injection systems in KSTAR". *Fusion Engineering and Design* **154**, 111 535, ISSN 0920-3796, DOI: https://doi.org/10.1016/j.fusengdes.2020.111535, URL https://www.sciencedirect.com/science/article/pii/S0920379620300831

Parks, P. 1980 "Magnetic-field distortion near an ablating hydrogen pellet". *Nuclear Fusion* **20** (3), 311, DOI: 10.1088/0029-5515/20/3/007, URL https://dx.doi.org/10.1088/0029-5515/20/3/007

Parks, P. B. 1996 "Theory of pellet cloud oscillation striations". *Plasma Physics and Controlled Fusion* **38** (4), 571, DOI: 10.1088/0741-3335/38/4/008, URL https://dx.doi.org/10.1088/0741-3335/38/4/008

Parks, P. 2016 "Modeling dynamic fracture of cryogenic pellets". Tech. Rep. GA-A28352, General Atomics, DOI: 10.2172/1344852

Parks, P. 2017 "A theoretical model for the penetration of a shattered-pellet debris plume". https://tsdw.pppl.gov/Talks/2017/Lexar/Wednesday%20Session%201/Parks.pdf. Presented at the Theory and Simulation of Disruptions Workshop

Parks, P. B. & Baylor, L. R. 2005 "Effect of parallel flows and toroidicity on cross-field transport of pellet ablation matter in tokamak plasmas". *Phys. Rev. Lett.* **94** (12), 125 002, DOI: 10.1103/PhysRevLett.94.125002

Parks, P. B. & Turnbull, R. J. 1978 "Effect of transonic flow in the ablation cloud on the lifetime of a solid hydrogen pellet in a plasma". *The Physics of Fluids* **21** (10), 1735, DOI: 10.1063/1.862088

Parks, P., Leffler, J. & Fisher, R. 1988 "Analysis of low Z impurity pellet ablation for fusion diagnostic studies". *Nuclear Fusion* **28** (3), 477, DOI: 10.1088/0029-5515/28/3/012

Parks, P. B., Sessions, W. D. & Baylor, L. R. 2000 "Radial displacement of pellet ablation material in tokamaks due to the grad-B effect". *Physics of Plasmas* **7** (5), 1968, DOI: 10.1063/1.874052

Paz-Soldan, C., Eidietis, N. W., Liu, Y. Q., Shiraki, D., Boozer, A. H., Hollmann, E. M., Kim, C. C. & Lvovskiy, A. 2019 "Kink instabilities of the post-disruption runaway electron beam at low safety factor". *Plasma Physics and Controlled Fusion* **61** (5), 054 001, DOI: 10.1088/1361-6587/aafd15, URL https://dx.doi.org/10.1088/1361-6587/aafd15

Paz-Soldan, C., Reux, C., Aleynikova, K., Aleynikov, P., Bandaru, V., Beidler, M., Eidietis, N., Liu, Y., Liu, C., Lvovskiy, A., Silburn, S., Bardoczi, L., Baylor, L., Bykov, I., Carnevale, D., Del-Castillo Negrete, D., Du, X., Ficker, O., Gerasimov, S., Hoelzl, M., Hollmann, E., Jachmich, S., Jardin, S., Joffrin, E., Lasnier, C., Lehnen, M., Macusova, E., Manzanares, A., Papp, G., Pautasso, G., Popovic, Z., Rimini, F., Shiraki, D., Sommariva, C., Spong, D., Sridhar, S., Szepesi, G., Zhao, C., the DIII-D Team & JET Contributors 2021 "A novel path to runaway electron mitigation via deuterium injection and current-driven MHD instability". *Nuclear Fusion* **61** (11), 116 058, DOI: 10.1088/1741-4326/ac2a69, URL https://dx.doi.

org/10.1088/1741-4326/ac2a69

Pégourié, B. 2007 "Review: Pellet injection experiments and modelling". *Plasma Physics and Controlled Fusion* **49** (8), 87, DOI: 10.1088/0741-3335/49/8/r01

Pegourie, B., Picchiottino, J.-M., Drawin, H.-W., Geraud, A. & Chatelier, M. 2002 "Pellet ablation studies on Tore Supra". *Nuclear Fusion* **33**, 591, DOI: 10.1088/0029-5515/33/4/I06

Pégourié, B., Waller, V., Nehme, H., Garzotti, L. & Géraud, A. 2006 "Homogenization of the pellet ablated material in tokamaks taking into account the ∇B-induced drift". *Nuclear Fusion* **47** (1), 44–56, DOI: 10.1088/0029-5515/47/1/006, URL https://doi.org/10.1088/0029-5515/47/1/006

Peherstorfer, T. 2022 "Fragmentation analysis of cryogenic pellets for disruption mitigation". *arXiv preprint* (arXiv:2209.01024), URL https://arxiv.org/abs/2209.01024

Pusztai, I., Ekmark, I., Bergström, H., Halldestam, P., Jansson, P., Hoppe, M., Vallhagen, O. & Fülöp, T. 2023 "Bayesian optimization of massive material injection for disruption mitigation in tokamaks". *Journal of Plasma Physics* **89**, 905890 204, DOI: 10.1017/S0022377823000193, URL https://doi.org/10.1017/S0022377823000193

Putvinski, S., Barabaschi, P., Fujisawa, N., Putvinskaya, N., Rosenbluth, M. N. & Wesley, J. 1997*a* "Halo current, runaway electrons and disruption mitigation in ITER". *Plasma Physics and Controlled Fusion* **39** (12B), B157, DOI: 10.1088/0741-3335/39/12B/013, URL https://dx.doi.org/10.1088/0741-3335/39/12B/013

Putvinski, S., Fujisawa, N., Post, D., Putvinskaya, N., Rosenbluth, M. & Wesley, J. 1997*b* "Impurity fueling to terminate tokamak discharges". *Journal of Nuclear Materials* **241-243**, 316–321, ISSN 0022-3115, DOI: https://doi.org/10.1016/S0022-3115(97)80056-6, URL https://www.sciencedirect.com/science/article/pii/S0022311597800566

Pégourié, B. & Dubois, M. 1989 "Magnetic surfaces and striations during pellet ablation". *Nuclear Fusion* **29** (5), 745, DOI: 10.1088/0029-5515/29/5/004, URL https://dx.doi.org/10.1088/0029-5515/29/5/004

Pégourié, B. & Picchiottino, J. 1996 "Plasma density buildup after pellet injection". *Physics of Plasmas* **3** (12), 4594, DOI: 10.1063/1.872030

Pégourié, B., Waller, V., Dumont, R. J., Eriksson, L.-G., Garzotti, L., Géraud, A. & Imbeaux, F. 2004 "Modelling of pellet ablation in additionally heated plasmas". *Plasma Physics and Controlled Fusion* **47** (1), 17, DOI: 10.1088/0741-3335/47/1/002, URL https://dx.doi.org/10.1088/0741-3335/47/1/002

Rechester, A. B. & Rosenbluth, M. N. 1978 "Electron heat transport in a tokamak with destroyed magnetic surfaces". *Phys. Rev. Lett.* **40**, 38, DOI: 10.1103/PhysRevLett.40.38

Reux, C., Plyusnin, V., Alper, B., Alves, D., Bazylev, B., Belonohy, E., Boboc, A., Brezinsek, S., Coffey, I., Decker, J., Drewelow, P., Devaux, S., de Vries, P., Fil, A., Gerasimov, S., Giacomelli, L., Jachmich, S., Khilkevitch, E., Kiptily, V., Koslowski, R., Kruezi, U., Lehnen, M., Lupelli, I., Lomas, P., Manzanares, A., Aguilera, A. M. D., Matthews, G., Mlynář, J., Nardon, E., Nilsson, E., von Thun, C. P., Riccardo, V., Saint-Laurent, F., Shevelev, A., Sips, G., Sozzi, C. & JET Contributors 2015 "Runaway electron beam generation and mitigation during disruptions at JET-ILW". *Nuclear Fusion* **55** (9), 093 013, DOI: 10.1088/0029-5515/55/9/093013

Reux, C., Paz-Soldan, C., Aleynikov, P., Bandaru, V., Ficker, O., Silburn, S., Hoelzl, M., Jachmich, S., Eidietis, N., Lehnen, M., Sridhar, S. & JET Contributors 2021 "Demonstration of safe termination of megaampere relativistic electron beams in tokamaks". *Phys. Rev. Lett.* **126**, 175 001, DOI: 10.1103/PhysRevLett.126.175001, URL https://link.aps.org/doi/10.1103/PhysRevLett.126.175001

Riccardo, V., Arnoux, G., Cahyna, P., Hender, T. C., Huber, A., Jachmich, S., Kiptily, V., Koslowski, R., Krlin, L., Lehnen, M., Loarte, A., Nardon, E., Paprok, R., Tskhakaya, D. & JET-EFDA contributors 2010 "JET disruption studies in support of ITER". *Plasma Physics and Controlled Fusion* **52** (12), 124 018, DOI: 10.1088/0741-3335/

52/12/124018, URL https://doi.org/10.1088/0741-3335/52/12/124018

Riemann, J., Smith, H. M. & Helander, P. 2012 "Energetics of runaway electrons during tokamak disruptions". *Physics of Plasmas* **19** (1), 012 507, ISSN 1070-664X, doi: 10.1063/1.3671974, URL https://doi.org/10.1063/1.3671974. https://pubs.aip.org/aip/pop/article-pdf/doi/10.1063/1.3671974/15882923/012507_1_online.pdf

Rosenbluth, M. & Putvinski, S. 1997 "Theory for avalanche of runaway electrons in tokamaks". *Nuclear Fusion* **37** (10), 1355, doi: 10.1088/0029-5515/37/10/i03

Rosenbluth, M. N., MacDonald, W. M. & Judd, D. L. 1957 "Fokker-Planck equation for an inverse-square force". *Phys. Rev.* **107**, 1–6, doi: 10.1103/PhysRev.107.1, URL https://link.aps.org/doi/10.1103/PhysRev.107.1

Rozhansky, V., Senichenkov, I., Veselova, I. & Schneider, R. 2004 "Mass deposition after pellet injection into a tokamak". *Plasma Physics and Controlled Fusion* **46** (4), 575–591, doi: 10.1088/0741-3335/46/4/001, URL https://doi.org/10.1088/0741-3335/46/4/001

Samulyak, R., Yuan, S., Naitlho, N. & Parks, P. 2021 "Lagrangian particle model for 3D simulation of pellets and SPI fragments in tokamaks". *Nuclear Fusion* **61** (4), 046 007, doi: 10.1088/1741-4326/abdcd2

Schuller, F. C. 1995 "Disruptions in tokamaks". *Plasma Physics and Controlled Fusion* **37** (11A), A135, doi: 10.1088/0741-3335/37/11A/009, URL https://dx.doi.org/10.1088/0741-3335/37/11A/009

Schwarz, N., Artola, F., Vannini, F., Hoelzl, M., Bernert, M., Bock, A., Driessen, T., Dunne, M., Giannone, L., Heinrich, P., de Marné, P., Papp, G., Pautasso, G., Gerasimov, S., the ASDEX Upgrade Team, JET Contributors & the JOREK Team 2023 "The mechanism of the global vertical force reduction in disruptions mitigated by massive material injection". *Nuclear Fusion* **63** (12), 126 016, doi: 10.1088/1741-4326/acf50a, URL https://dx.doi.org/10.1088/1741-4326/acf50a

Senichenkov, I., Rozhansky, V. & Gusakov, P. 2007 "The pellet rocket acceleration caused by ∇B-induced drift". In "Europhysics Conference Abstracts", vol. 31F, (P4.094), Warsaw: European Physical Society, URL https://info.fusion.ciemat.es/OCS/EPS2007/pdf/P4_094.pdf

Sheikh, U., Decker, J., Hoppe, M., Pedrini, M., Sieglin, B., Simons, L., Cazabonne, J., Caloud, J., Cerovsky, J., Coda, S., Colandrea, C., Dal Molin, A., Duval, B., Ficker, O., Griener, M., Papp, G., Pautasso, G., Paz-Soldan, C., Reux, C., Tomesova, E., Wijkamp, T., the ASDEX Upgrade Team, the TCV Team & the MST1 Team 2024 "Benign termination of runaway electron beams on ASDEX Upgrade and TCV". *Plasma Physics and Controlled Fusion* **66** (3), 035 003, doi: 10.1088/1361-6587/ad1e31, URL https://dx.doi.org/10.1088/1361-6587/ad1e31

Shiraki, D., Herfindal, J., Baylor, L. R., Hollmann, E. M., Lasnier, C., Bykov, I., Eidietis, N., Raman, R., Sweeney, R., Sheikh, U., Gerasimov, S., Jachmich, S., Lehnen, M., Kim, J., Jang, J. J., Meitner, S. & Gebhart, T. 2020 "Particle assimilation during shattered pellet injection". https://conferences.iaea.org/event/217/contributions/16713/. Presented at the IAEA Technical Meeting on Plasma Disruption and their Mitigation

Smith, H. M. & Verwichte, E. 2008 "Hot tail runaway electron generation in tokamak disruptions". *Physics of Plasmas* **15** (7), 072 502, doi: 10.1063/1.2949692

Smith, H., Helander, P., Eriksson, L.-G. & Fülöp, T. 2005 "Runaway electron generation in a cooling plasma". *Physics of Plasmas* **12** (12), 122 505, doi: 10.1063/1.2148966

Smith, H. M., Boozer, A. H. & Helander, P. 2013 "Passive runaway electron suppression in tokamak disruptions". *Physics of Plasmas* **20** (7), 072 505, ISSN 1070-664X, doi: 10.1063/1.4813255, URL https://doi.org/10.1063/1.4813255. https://pubs.aip.org/aip/pop/article-pdf/doi/10.1063/1.4813255/16030770/072505_1_online.pdf

Sokolov, Y. A. 1979 ""Multiplication" of accelerated electrons in a tokamak". *JETP Lett. (USSR) (Engl. Transl.); (United States)* **29** (4)

Stahl, A., Embréus, O., Papp, G., Landreman, M. & Fülöp, T. 2016 "Kinetic modelling of runaway electrons in dynamic scenarios". *Nuclear Fusion* **56** (11), 112 009, doi: 10.1088/0029-5515/56/11/112009, URL https://dx.doi.org/10.1088/0029-5515/56/11/112009

Summers, H. P. 2004 "The ADAS user manual, version 2.6". URL http://www.adas.ac.uk

Svenningsson, I., Embreus, O., Hoppe, M., Newton, S. L. & Fülöp, T. 2021 "Hot-tail runaway seed landscape during the thermal quench in tokamaks". *Physical Review Letters* **127**, 035 001, doi: 10.1103/PhysRevLett.127.035001, URL https://arxiv.org/abs/2104.03272

Svensson, P. 2020 "Effects of magnetic perturbations and radiation on the runaway avalanche". URL https://hdl.handle.net/20.500.12380/300784

Szepesi, T., Kálvin, S., Kocsis, G., Lang, P. T. & Senichenkov, I. 2009 "Comparison of pellet acceleration model results to experimentally observed penetration depths". *Journal of Nuclear Materials* **390** (1), 507, ISSN 0022-3115, doi: 10.1016/J.JNUCMAT.2009.01.063. Publisher: North-Holland

Taylor, P. L., Kellman, A. G., Evans, T. E., Gray, D. S., Humphreys, D. A., Hyatt, A. W., Jernigan, T. C., Lee, R. L., Leuer, J. A., Luckhardt, S. C., Parks, P. B., Schaffer, M. J., Whyte, D. G. & Zhang, J. 1999 "Disruption mitigation studies in DIII-D". *Physics of Plasmas* **6** (5), 1872–1879, ISSN 1070-664X, doi: 10.1063/1.873445, URL https://doi.org/10.1063/1.873445. https://pubs.aip.org/aip/pop/article-pdf/6/5/1872/19073137/1872_1_online.pdf

Tinguely, R., Izzo, V., Garnier, D., Sundström, A., Särkimäki, K., Embréus, O., Fülöp, T., Granetz, R., Hoppe, M., Pusztai, I. & Sweeney, R. 2021 "Modeling the complete prevention of disruption-generated runaway electron beam formation with a passive 3D coil in SPARC". *Nuclear Fusion* **61** (12), 124 003, doi: 10.1088/1741-4326/ac31d7, URL https://dx.doi.org/10.1088/1741-4326/ac31d7

Tinguely, R. A., Pusztai, I., Izzo, V. A., Särkimäki, K., Fülöp, T., Garnier, D. T., Granetz, R. S., Hoppe, M., Paz-Soldan, C., Sundström, A. & Sweeney, R. 2023 "On the minimum transport required to passively suppress runaway electrons in SPARC disruptions". *Plasma Physics and Controlled Fusion* **65** (3), 034 002, doi: 10.1088/1361-6587/acb083

Tinguely, R. A., Sweeney, R., Boguski, J., Riccardo, V., Rosenthal, A., Kilgus, D., Myers, C., Reinke, M., Clauser, C., Datta1, R., Feyrer, A., Panontin, E., Izzo, V., Ekmark, I., Fülöp, T., Pusztai, I., Logan, N., Hoppe, M., Ratynskaia, S., Paschalidis, M., Tolias, P. & Rizzi, T. 2025 "An update on runaway electron modeling and mitigation in SPARC". URL https://ft.nephy.chalmers.se/do/downloadconfpresentation.php?id=183. Presented at the Joint Runaway Electron Modelling (REM) and WPTE RT03 Analysis meeting

UK Atomic Energy Authority https://step.ukaea.uk/

Vallhagen, O. 2021 "Disruption mitigation in tokamaks with shattered pellet injection". URL https://hdl.handle.net/20.500.12380/302296

Wang, C., Nardon, E., Artola, F., Bandaru, V., Hoelzl, M. & the JOREK team 2024 "The effect of vertical displacements on the runaway electron avalanche in ITER mitigated disruptions". *Nuclear Fusion* **65** (1), 016 012, doi: 10.1088/1741-4326/ad8d66, URL https://dx.doi.org/10.1088/1741-4326/ad8d66

Ward, D. & Wesson, J. 1992 "Impurity influx model of fast tokamak disruptions". *Nuclear Fusion* **32** (7), 1117, doi: 10.1088/0029-5515/32/7/i03

Weisberg, D., Paz-Soldan, C., Liu, Y., Welander, A. & Dunn, C. 2021 "Passive deconfinement of runaway electrons using an in-vessel helical coil". *Nuclear Fusion* **61** (10), 106 033, doi: 10.1088/1741-4326/ac2279, URL https://dx.doi.org/10.1088/1741-4326/ac2279

Wesson, J. 2011 Tokamaks. 4th edn., Oxford, UK: Oxford University Press

Yoshino, R. & Tokuda, S. 2000 "Runaway electrons in magnetic turbulence and runaway current termination in tokamak discharges". *Nuclear Fusion* **40** (7), 1293, doi: 10.1088/0029-5515/40/7/302, URL https://doi.org/10.1088/0029-5515/40/7/302

Zhang, J. & Parks, P. 2020 "Analytical formula for pellet fuel source density in toroidal plasma configurations based on an areal deposition model". *Nuclear Fusion* **60** (6), 066 027, DOI: 10.1088/1741-4326/ab868e, URL https://dx.doi.org/10.1088/1741-4326/ab868e